Charge Transfer Dynamics in Quantum Dot & Quantum Dot Based Nanostructures

By

Sreejith Kaniyankandy
Enrolment Number: CHEM01200604009
Bhabha Atomic Research Centre

A
Thesis submitted to the
Board of Studies in Chemical Sciences

In partial fulfillment of requirements
For the Degree of

DOCTOR OF PHILOSOPHY

of

HOMI BHABHA NATIONAL INSTITUTE

APRIL 2012

Homi Bhabha National Institute

Recommendations of the Viva Voce Board

As members of the Viva Voce Board, we certify that we have read the dissertation prepared by **Sreejith Kaniyankandy** entitled "**Charge Transfer Dynamics in Quantum Dot & Quantum Dot Based Nanostructures**" and recommend that it may be accepted as fulfilling the dissertation requirement for the Degree of Doctor of Philosophy.

Tulsi Mukherjee Date: 17/9/12

Chairman: Prof. T. Mukherjee

Date: 17/9/12

Guide/Convener: Asst. Prof. H. N. Ghosh

Amitava Patra Date: 17.9.12

External Examiner: Prof. A. Patra

Date: 17/09/2012

Member 1: Senior Prof. S. K. Sarkar

Palit Date: 17-09-12

Member 2: Prof. D. K. Palit

Date: 17-09-2012

Member 3: Prof. A. K. Tyagi

Final approval and acceptance of this dissertation is contingent upon the candidate's submission of the final copies of the dissertation to HBNI. I hereby certify that I have read this dissertation prepared under my direction and recommend that it may be accepted as fulfilling the dissertation requirement.

Date: 17/9/12

Place: BARC, Mumbai

STATEMENT BY AUTHOR

This dissertation has been submitted in partial fulfillment of requirements for an advanced degree at Homi Bhabha National Institute (HBNI) and is deposited in the Library to be made available to borrowers under rules of the HBNI.

Brief quotations from this dissertation are allowable without special permission, provided that accurate acknowledgement of source is made. Requests for permission for extended quotation from or reproduction of this manuscript in whole or in part may be granted by the Competent Authority of HBNI when in his or her judgment the proposed use of the material is in the interests of scholarship. In all other instances, however, permission must be obtained from the author.

(Sreejith Kaniyankandy)

DECLARATION

I, hereby declare that the investigation presented in the thesis has been carried out byme. The work is original and has not been submitted earlier as a whole or in part for a degree / diploma at this or any other Institution / University.

(Sreejith Kaniyankandy)

DEDICATED TO MY FAMILY

ACKNOWLEDGEMENTS

It is my privilege to thank my guide **Dr. H. N. Ghosh,** without his help, constant guidance, inspiration and critical suggestions throughout the period of my doctoral work.

It is always a pleasure to thank my superiors **Dr. T. Mukherjee**, Director, Chemistry Group, **Dr. S. K. Sarkar**, Head, RPCD and **Dr. D. K. Palit**, Head, UDCS, RPCD for their constant encouragement and support throughout the period of my thesis work.

I express my sincere gratitude to **Dr. A. Dutta**, Department of chemistry, IIT Bombay, **Dr. P. V. Satyam**, IOP, Bhubaneshwar, **Dr. A. Das**, CSMCRI, Bhavnagar and Dr. D. Srivastava, CSMCRI, Bhavnagar and their students for their support and help in carrying out experiments.

I owe a lot to my colleagues **S. Verma** and **S. Rawalekar** for their help and moral support throughout the course of my work. Thanks are also due to **J. A. Mondal, Chandralekha Singh, R. Ghosh** for their help rendered from time to time.

I am indebted to my colleagues in chemistry group for their support. My appreciation also goes out to **Dr. S. N. Achary** for stimulating scientific discussions.

I owe a lot to my parents for the encouragement, support and love without which this PhD would not have been possible. Thanks are also due to my sister and nephew during difficult times. Last but not least, my wife for her support, encouragement and understanding without which this thesis would not have been possible.

CONTENTS

Title **Page Number**

Synopsis **xiii-xx**

List of Figures **xxi-xxvi**

List of Tables **xxvii-xxviii**

List of Schemes **xxix**

Abbreviations **xxx-xxxi**

Chapter 1

Introduction

1.1. Nanotechnology Before 20th Century 2-4

1.2. Physics of Semiconductors

1.2.1. Introduction 5-8

1.2.2. Effective Mass Approximation 8-9

1.2.3. Effect of 3-Dimensional Confinement on Electronic Structure 9-13

1.2.4. Confinement Effect in Real Band Structures 13-15

1.2.5. Dimensionality and Density of States (DOS) 15-17

1.3. Carrier Relaxation in Quantum Dots 17-18

1.3.1. Phonon mediated mechanism 18-19

1.3.2. Electron-Hole energy transfer mechanism 19

1.3.3. Multiparticle Auger Processes 19-20

1.3.4. Impact Ionization 20-21

1.3.5. Defect Mediated Relaxation 21

1.4. How Can QDs Help in Solar Cells? 21-23

1.5. “Improving on” QDs 24

1.5.1. Semiconductor-Semiconductor Core Shell Nanostructures 24-25

1.5.2. Semiconductor-Dye Nanostructures 26

1.5.3. Metal-Semiconductor Nanostructures 26-27

1.6. Classical Electron Transfer 27-29

1.6.1. Adiabatic and Non-Adiabatic Process 29-30

1.6.2. Classical Electron Transfer Theory 30-33

1.6.3. Quantum mechanical theory of electron transfer 33-34

1.7 Interfacial Electron Transfer from Molecular Adsorbate to Semiconductor 34-35

1.7.1. Electron Injection 35-37

1.7.2. Back Electron Transfer 37-38

1.8. Synthesis of Semiconductor Quantum Dots 38-41

1.9. Thesis Overview 42-43

1.10. Scope of the Thesis in View of Applications in Photovoltaics 42-43

1.11. Thesis Overview 43-46

Chapter 2

Experimental

2.1. Introduction 48

2.2. UV-Visible Absorption Spectroscopy 48-50

2.3. Fluorescence Spectroscopy 50-51

2.4. X-Ray Diffraction

2.4.1. Introduction 51-53

2.4.2. Instrumentation 53-54

2.4.3. Raman Spectroscopy 54-55

2.6. Transmission Electron Microscopy (TEM)

2.6.1. Introduction 56-57

2.6.2. Layout of TEM 57-60

2.6.3. Selected Area Electron Diffraction 60-61

2.6.4. Electron Energy Loss Spectroscopy (EELS) 61

2.7. Time Correlated Single Photon Counting

2.7.1. Introduction 61-62

2.7.2. Instrumentation 62-64

2.7.2.1. Constant Fraction Discriminator 64-65

2.7.2.2. Time to Amplitude Converter 65

2.7.2.3. Multichannel Analyzer 65

2.7.2.4. Data Analysis 65-66

2.8. Broadband Pump-Probe Femtosecond Transient Absorption Spectroscopy

2.8. 1. Introduction 66-70

2. 8. 2. Experimental set up

2. 8. 2. 1. Ti-Sapphire (Ti-S) Oscillator 70-71

2.8.2.2. Amplifier 72-73

2.8.2.3. Multistage Amplification 73-76

2. 8. 2. 4. Pulse Compressor 76-77

2.8.3. Second Harmonic Generation-400nm Pump 77-78

2. 8. 4. White Light Generation- 450-1100nm Probe 78-79

2. 8. 5. Laser diagnostics 79-80

2.9. References 80-82

Chapter 3

Charge Carrier Dynamics in Ultrasmall TiO_2-Alizarin System

3.1. Introduction 84-86

3.2. Experimental Section

3.2.1. Materials 87

3.2.2. Preparation of ultrafine TiO_2 nanoparticles 87

3.3. Results & Discussion

3.3.1. TEM & XRD Studies 88-89

3.3.2. Steady State UV-Vis Absorption Studies 89-91

3.3.3. Femtosecond Transient Absorption Studies 91-102

3.4. Conclusions 102-104

3.5. References 104-106

Chapter 4

Effect of Size Quantization on Charge Carrier Dynamics in Thiol Capped CdTe Quantum Dots

4.1. Introduction 108-110

4.2. Experimental Section:

4.2. 1. Materials 110

4.2. 2. Synthesis 111

4.3. Results & Discussion:

4.3.1. Steady State Absorption Studies 112-113

4.3.2. Femtosecond Transient Absorption Studies 113-123

4.4. Conclusion 124

4.5. References 125-126

Chapter 5

Charge Carrier Dynamics in Tailored CdSe/ ZnTe Core Shell Nanostructure

5.1. Introduction 128-131

5.2. Experimental

5.2.1. Materials 131

5.2.2. Synthesis of CdSe QDs 131-132

5.2.3. Shell Growth 132

5.3. Result and discussion

5.3.1. TEM & XRD Studies 133-134

5.3.2. Steady state absorption and emission studies 134-137

5.3.3. Time resolved emission studies 138-140

5.3.4. Transient absorption spectroscopy of CdSe QD 140-143

5.3.5. Transient absorption studies of CdSe/ZnTe core-shell QD 144-151

5.4. Conclusions 150-151

5.5. References 151-153

Chapter 6

Charge Separation in CdTe Decorated Graphene

6.1. Introduction 155-157

6.2. Experimental

6.2.1.Synthesis of Graphene Oxide 157

6.2.2.Reduction of Graphene Oxide 158

6.2.3Synthesis of CdTe Decorated Graphene 158-159

6.3.Results and Discussion

6.3.1.TEM Studies 159-160

6.3.2.Steady State UV-Vis Absorption and Emission Studies 160-161

6.3.3.TCSPC Studies 161-162

6.3.4.Femtosecond Transient Absorption and Kinetics of Graphene Oxide and reduced Graphene Oxide 162-172

6.3.5.Femtosecond Transient Absorption of CdTe Quantum Dot Decorated Reduced Graphene Oxide 172-179

6.4.Conclusions 179-180

6.5.References 180-183

Chapter 7

Summary and Outlook

7.1. Summary 184-187

7.2. Outlook 187-189

Chapter 8

List of Publications 190

SYNOPSIS

Energy based on nonrenewable energy sources like fossil fuels e.g. coal; petrol and diesel have been driving global growth for the past several decades [1]. Presently we have reached a point where there is a supply bottleneck leading to energy crisis [2]. If world economies have to sustain economic growth, this energy crisis must be offset before long. In this context renewable energy sources have been receiving renewed interest, as these sources are perennial [3]. Among renewable energy sources solar energy has received considerable attention. The amount of energy that earth receives in an hour is much greater than energy consumed globally, making solar energy trapping of considerable interest not only due to magnitude of energy but also due to its low carbon footprint. Among methods for exploiting energy from sunlight, photovoltaic cells has emerged as an attractive option. Photovoltaic cells have evolved with time from silicon based cells to dye sensitized solar cell. Presently DSSC have an efficiency of ~10% and it uses cheap non toxic material like dye sensitized semiconductor TiO_2 [4]. In a DSSC as demonstrated by Graetzel TiO_2 [4] acts as the acceptor of electrons from photo excited dye, this forms one half of a DSSC. Therefore electron injection and back electron transfer processes play an important role in final efficiency of DSSC. Therefore a study of photo induced processes helps in understanding the influence of injection and BET processes in improving efficiency of DSSC and literature on such studies has been exhaustive. Among recent developments in the field of photovoltaics quantum dots have received considerable attention lately due to Size dependent electronic Properties [5]. Size dependent properties enable a continuous tunability of absorption of light [6]. Their importance in solar cells has been amply demonstrated in photovoltaic devices based on QDs [7, 8]. These studies have shown considerable promise in photovoltaics. In devices based on QDs it has been shown that Size of QDs also affects photovoltaic efficiency, maximum current and V_{oc} [7, 8]. This is due to size dependent variation in electronic properties leading to change in free energy and surface properties. Work on QDs has shown that surface plays major roles in determining photovoltaics properties due to the fact that surface to volume ratio of QDs are very high because of their small dimensions. Apart from tunability of electronic properties, in QDs there are several reports on production of multiple excitons induced by excitation of QD with photons of energy many times the band gap energy [9, 10]. This novel effect also has been exploited in photovoltaics to improve the efficiency of energy conversion [11]. Additionally one can use a QD in place of TiO_2 as the electron acceptor which would help in hot carrier based DSSC. As mentioned earlier the surface, interface properties have a clear bearing on photovoltaic efficiency. Therefore it is imperative to understand photo induced dynamics which would further help in improving the properties of quantum dot. In that context transient absorption spectroscopy has been a valuable tool in understanding the influence of surfaces and interfaces in relaxation dynamics in time scale of few hundred fs to ms [12-14].

The main thrust in the present thesis is on synthesis of QDs and QD based nanostructures and study of its dynamics with change in size, surface and nanostructure formation. The QDs synthesized in the present thesis are mostly II-VI semiconductors. Nanostructures were formed with a core shell geometry and QDs decorated metal. The study not only involves influence of size but also charge separation behavior in novel nanostructures like core shell. The QD based nanostructure have been synthesized and structurally characterized by TEM, Raman spectroscopy, XRD. The dynamics was measured by femtosecond spectroscopy transient absorption.

CHAPTER 1: GENERAL INTRODUCTION

This chapter gives a brief introduction to nanotechnology and basic semiconductor physics and electronic structure of a bulk crystal with simple quantum mechanical models. A brief description of theoretical framework based on effective mass approximation to describe changes in electronic structure with size. Typical band structures in real systems like CdSe, CdTe etc is also described. A brief account of processes involved in relaxation of carriers on photoexcitation is described. Methods to improve the relaxation behavior are also discussed with particular emphasis on core shell and metal semiconductor nanostructure. A concise description of Marcus theory of electron transfer which gives the theoretical framework for electron transfer is also outlined. Additionally brief discussion on types of electron transfer processes, adiabatic and non adiabatic is included. Importance of synthesis conditions to obtain monodisperse particles is delineated along with synthesis technique used in present thesis for II-VI QDs.

CHAPTER 2: EXPERIMENTAL TECHNIQUE

A summary of experimental techniques used in this thesis for characterization of materials to dynamics study is described in this chapter. A brief outline of transmission electron microscope and additional information like electron diffraction and elemental analysis is outlined. Additionally description of steady state UV-Vis absorption, photoluminescence spectroscopy is also delineated. A brief description Time correlated single photon counting technique and instrumentations involved is explained. Hot exciton relaxation in QDs takes place in the femtosecond time scale, to study ultrafast phenomena we have used Femtosecond Transient absorption spectroscopy. Basic techniques involved in generation of a femtosecond pulse, amplification and characterization is described.

Furthermore generation of pump (~400nm) by second harmonic generation, probe (450-1000nm) by white light continuum generation is delineated. Layout of the set up used in the present thesis is also described in detail

CHAPTER 3: CHARGE CARRIER DYNAMICS IN ULTRASMALL TiO_2-ALIZARIN SYSTEM

Present chapter deals with effect of size quantization on carrier dynamics in a dye sensitized ultrasmall TiO_2 system. A QD presents a discrete set of acceptor states as opposed to a continuum of states in a bulk semiconductor. This is bound to influence ET rates from (injection) and back (BET) to dye. In such a system owing to discreteness it is might also be possible to extract hot electrons in presence of reduced relexation within individual bands in a QD. The system investigated in the present thesis is TiO_2 sensitized with alizarin dye. TiO_2 nanoparticles were synthesized by colloidal methods. Nanoparticles were characterized by XRD, TEM, Raman spectroscopy. Femtosecond dynamics were monitored by transient absorption spectroscopy. Conclusions on dynamics of injection and BET were drawn by monitoring the electron absorption signal after injection into TiO_2. These studies clearly indicate an efficient charge separation in the system investigated apart from observation of multiple injection components.

CHAPTER 4: EFFECT OF SIZE QUANTISATION ON CHARGE CARRIER DYNAMICS IN CdTe QDs

Effect of size quantization on carrier relaxation (cooling and recombination) dynamics in size series of CdTe QD is investigated in this chapter. Series of CdTe QDs of different size was synthesized by colloidal methods in water. These samples were characterized by structural and photophysical techniques. Apart from discreteness in individual bands, surface to volume ratio varied with size of samples. These factors affect not only recombination dynamics but also cooling dynamics. The bleach formation is an index of electron cooling times and recovery corresponds to recombination times. In a QD cooling of electrons is governed by several mechanisms. Therefore we have attempted to draw conclusions on cooling processes involved by studying size dependent dynamics in CdTe QDs. The dynamics were monitored throughout visible region to arrive at mechanism of cooling and recombination in QDs. These studies help in understand factors influencing relaxation dynamics in QDs.

CHAPTER 5: CHARGE CARRIER DYNAMICS IN TAILORED CdSe/ZnTe CORE SHELL NANOSTRUCTURE

Control over relaxation behavior of QDs is of immense interest as such a control will provide us a way to manipulate a nanostructure according to different application for e.g. a straddled line up in a core shell helps in improving luminescence behavior or a staggered line up helps in charge separation therefore in photovoltaics. In such nanostructures charge relaxation is modified compared to core due modification ban alignment but also due to formation of an interface. In this chapter we explore how a staggered interface alignment in a QD core shell influences carrier dynamics. Core shell samples were synthesized by colloidal methods by growing a shell over core under conditions where homogeneous nucleation is negligible. The system chosen for core shell is CdSe/ZnTe as this system has a staggered band alignment. In this case charge transfer either an electron or hole takes place depending on the band alignment. This is particularly useful in applications where charge separation is required for e.g. photovoltaics. In the present work we have attempted to answer how fast this transfer takes place by monitoring bleach formation kinetics of CdSe. The cooling dynamics with respect to thickness of shell revealed ultrafast hole transfer from CdSe to ZnTe (core to shell). This clearly indicated that charge transfer takes place much faster than cooling and trapping which is immensely beneficial charge separation.

CHAPTER 6: CHARGE SEPARATION IN CdTe DECORATED GRAPHENE

In this chapter we investigate how one can manipulate relaxation dynamics in QDs by decorating it on a metal. This study is particularly useful as metals have large density of acceptor states which enable an efficient and fast charge separation. The system we have investigated is chemically synthesized reduced graphene oxide decorated with CdTe QDs. Synthesis of QDs were accomplished by colloidal methods in presence of reduced graphene oxide. Formation of heterostructure is verified by transmission electron microscopy. Strong interaction between CdTe and graphene was confirmed by photophysical studies. Furthermore, we have unraveled how graphene affect dynamics by femtosecond transient absorption study by monitoring bleach recovery kinetics of CdTe quantum dots. These dynamics were also compared with free QDs and reduced graphene. These studies clearly indicate an efficient that charge separation of G-CdTe composite materials.

CHAPTER 7: SUMMARY AND OUTLOOK

Aim of the thesis was to investigate not only relaxations dynamics in QDs and heterostructures based on QDs but also to look for ways to improve on QDs. One of the obvious ways a quantum dot has been utilized is by varying its size which helps in tuning absorption in visible region, but does this modification itself result in an improvement of efficiency for applications like photovoltaics. In the present thesis we demonstrate several ways by which better charge separation can be achieved. The study of charge relaxation dynamics helped us understand charge relaxation in heterostructure better. Such manipulation of nanostructure showed that there is still lot of scope for improving on QD relation behavior. These studies have a direct bearing on applications like photovoltaics, nanoelectronics etc.

CHAPTER 8

List of Publications

REFERENCES

1. Bartlett, A. A. Sustained availability: A management program for nonrenewable resources. Am. J. Phys., 1986, 54, 398.
2. Deffeyes, K. S. Hubbert's Peak: The Impending World Oil Shortage. Princeton University Press: Princeton, NJ, 2001.
3. Dresselhaus, M. S.; Thomas, I. L. Alternative energy technologies. Nature, 2001, 414, 332.
4. Brian O' Regan, Michael Grätzel, Nature, 1991, 353, 737.
5. Prashant V. Kamat, Meeting the Clean Energy Demand: Nanostructure Architectures for solar energy conversion, J. Phys. Chem. C, 2007, 111, 2834.
6. D. J. Norris, M. G. Bawendi, Phys. Rev. B,1996, 53, 16338.
7. Prashant V. Kamat, J. Phys. Chem. C, 2008, 112, 18737.
8. S. A. McDonald, G. Konstantatos, S. Zhang, P. W. Cyr1, E. J. D. Klem, L. Levina, E. H. Sargent, Nature Materials, 2005, 4, 138.
9. R. J. Ellingson, M. C. Beard, J. C. Johnson, P. Yu, O. I. Micic, A. J. Nozik, A. Shabaev, A. L. Efros, Nano Lett., 2005, 5, 865.
10. R. D. Schaller, M. Sykora, J. M. Pietryga, V. I. Klimov, Nano Lett., 2006, 6, 424.
11. V. Sukhovatkin, S. Hinds, L. Brzozowski,E. H. Sargent, Science, 2009, 324, 1542.

12. V. I. Klimov, J. Phys. Chem. B, 2000, *104*, 6112.

13. R. R. Cooney, S. L. Sewall, K. E. H. Anderson, E. A. Dias, P. Kambhampati, Phys. Rev. Lett., 2007, 98, 177403.

14. P. Yu, J. M. Nedeljkovic, P. A. Ahrenkiel, R. J. Ellingson, A. J. Nozik, Nano Lett., 2004, 4, 1089.

LIST OF FIGURES

Figure Number	Figure Caption	Page Number
1.1	Schematic of Energy Band in a typical semiconductor versus bond length	5
1.2	Potential in Kronig-Penney model.	6
1.3	Typical Band Structure of Cubic and Hexagonal CdSe, where hh=Heavy Hole Band, lh=Light Hole Band, SO-Split-Off Band. These bands are also referred to as A, B, and C respectively.	14
1.4	Schematic of DOS in different confined systems.	16
1.5	Schematic of electron-hole energy transfer process.	19
1.6	Schematic of electron-hole Auger process.	20
1.7	Schematic of Impact Ionization Process	21
1.8	Schematic of Dye Sensitized Solar Cell	23
1.9	Schematic of Band Alignment in QD Core Shell	25
1.10	Schematic of Band Alignment in Metal-QD Composite	27
1.11	Reactant and Product Potential Energy Curves	28
1.12	Reactant and Product Potential Energy Curves with Interaction between Curves.	30

1.13	Reactant and Product Potential Energy Surfaces for weak interaction. A= Reactant, B=Product, q_{A0}=Reactant Equilibrium Position, q_{B0}=Product Equilibrium Position	31
1.14	Schematic of ln(k_{et}) vs ΔG^0.with different regions. Region I, Region II and Region III are called Normal region, barrierless region and inverted region respectively	32
1.15	Schematic of ET from a reactant state to a continuum of product states.	36
1.16	Nucleation and growth stages for preparation of monodisperse nanoparticles in La Mer Growth model.	40
2.1	Schematic of a typical XRD instrument	54
2.2	Schematic of a TEM instrument	58
2.3	Schematic of working principle of TCSPC technique	64
2.4	Schematic of a pump-probe set up	68
2.5	Schematic of a pump-probe set up used in the present thesis	69
2.6	Optical layout of Ti-S Oscillator used in the present studies	71
2.7	Schematic of Offner Stretcher	73
2.8	Optical layout of JADE laser used for amplification	74
2.9	Optical layout of 2-Stage Amplifier	76
2.10	Schematic of a typical compressor	77
2.11	Schematic of a WLG in set up used for present studies	79

2.12 Schematic diagram of autocorrelator 80

3.1 TEM and SAED patterns of B-TiO_2 sample 88

3.2 XRD patterns of TiO_2 samples 89

3.3 Optical absorption spectra of (a) benzophenone modified TiO_2 (B-TiO_2) in toluene (1 gm/L), (b) alizarin (Alz) in toluene (c) Alz sensitized B-TiO_2 in toluene and in inset: (d) difference spectra between c and b, which gives indication the formation of charge transfer (CT) complex between Alz and TiO_2. 90

3.4 Transient absorption spectra of B- TiO_2 -Alizarin in toluene after 400nm excitation. 91

3.5 Kinetic Decay Traces of B- TiO_2 -Alizarin in toluene after 400nm excitation at λ_{pr}=550nm 93

3.6 Schematic Diagram representing the electron transfer dynamics in both TiO_2 nanoparticle and TiO_2 quantum dot sensitized by alizarin in toluene. It shows multiexponential injection and slow back ET on quantum dot surface and single exponential injection and faster back ET on nanoparticle surface. 100

4.1 Optical Absorption Spectrum of CdTe Samples. The Samples are numbered in the increasing order of sizes. 113

4.2 Transient absorption spectra of CdTe quantum dot (QD) at different time delay after excitation at 400 nm laser 114 light. Inset: Kinetic traces monitored at 530nm (Figure 3 a) and at 610nm (Figure 3 b) and optical absorption spectra for the sample.

4.3 Normalized kinetic traces photoexcited CdTe for different particle sizes at 610 nm (1S exciton position). Panel B: Plot of cooling time (growth kinetics at 1S exciton) vs particle size showing non-linear increment. 118

4.4 Normalized kinetic traces of a) CdTe, b) CdTe with BQ and c) CdTe with BA at 610 nm (1S exciton position). Inset: Same kinetic traces at shorter time scale. 119

5.1 High-resolution TEM (HR-TEM) image of CdSe/ZnTe quantum dot core-shell (Panel A) and same picture in higher resolution Panel B). Insets: Selected electron diffraction patternof the corresponding particles. 133

5.2 XRD Pattern for CdSe/ZnTe quantum dot core-shell 134

5.3 Steady state absorption spectra of a) CdSe (thick solid line), b) CdSe/ZnTe1 (short dash), c) CdSe/ZnTe2 (dash dot), d) CdSe/ZnTe3 (dash-dot-dot) and e) CdSe/ZnTe4 (thin solid line) 135

5.4 Normalized steady state emission spectra of a) CdSe (thick solid line), b) CdSe/ZnTe1 (short dash), c) CdSe/ZnTe2 (dash dot), and d) CdSe/ZnTe3 (dash-dot-dot) 137

5.5	Time resolved emission decay traces of a) CdSe, b) CdSe/ZnTe1, and c) CdSe/ZnTe3	139
5.6	Transient absorption spectra of CdSe quantum dot (QD) at different time delay after excitation at 400 nm laser light. Inset: Kinetic decay trace monitored at 690 nm.	142
5.7	Transient absorption spectra of CdSe/ZnTe3 (top panel) and CdSe/ZnTe4 (bottom panel) Quantum dot core-shell at different time delay after excitation at 400 nm laser light.	144
5.8	Normalized kinetic traces of a) CdSe at 460 nm, b) CdSe/ZnTe3 at 480 nm, and c) CdSe/ZnTe4 at 520 nm after excitation at 400 nm laser light. Inset: Same kinetics are shown at shorter time scale.	145
6.1	Transmission Electron Microscopy (High and Low magnifications) and Electron Diffraction of G-CdTe samples.	159
6.2	Photoluminescence Spectra of a) CdTe and b) G-CdTe after exciting the sample at 380 nm. Inset: optical absorption spectra of c) CdTe and d) G-CdTe.	161
6.3	Time-resolved emission kinetics of a) CdTe and b) G-CdTe after exciting the sample at 400 nm	162
6.4	Transient absorption spectra of graphene oxide (GO) at different time delay after exciting 400 nm laser pulse	163

6.5 Transient decay kinetics of graphene oxide (GO) at 670 nm after exciting at 400 nm laser pulse. Inset: Absorbance change (Δ O. D.) graphene oxide (GO) at 670 nm at different excitation energy density (pump intensity) 164

6.6 Figure 6.6: Transient decay kinetics of graphene oxide (GO) at 670 nm after exciting at 400 nm laser pulse in absence of any quencher (GO), in presence of electron quencher (GO-BQ) and in presence of hole quencher (GO-PY) 167

6.7 Transient absorption spectra of reduced (24 hours) graphene oxide (RGO-2) at different time delay after exciting 400 nm laser pulse. Inset: Transient decay kinetics at 670 nm. 170

6.8 Femtosecond Transient absorption spectrum at different time delays for CdTe (a) and G-CdTe (b) after excitation at λ_{pump}=400nm. 173

6.9 Bleach recovery kinetics at 460 nm for a) CdTe and b) G-CdTe after 400 nm laser excitation. 174

LIST OF TABLES

Table Number	Table Caption	Page Number
3.1	Parameters for the multi-exponential Fits to the electron injection and back electron transfer (BET) kinetics of alizarin sensitized B-TiO_2 after monitoring both alizarin cation at 550 nm and electron in the conduction band at 900 nm.	94
5.1	Fits for emission decay traces for core and core shell samples	140
5.2	Fit for kinetic traces of a) CdSe at 460 nm, b) CdSe/ZnTe3 at 480 nm, and c) CdSe/ZnTe4 at 520 nm after excitation at 400 nm laser light.	147
6.1	Life times of the transient absorption signal of graphene oxide at 670 nm after exciting at 400 nm laser light in absence of any quencher (GO), in presence of electron quencher (GO-BQ) and in presence of hole quencher (GO-PY).	168
6.2	Lifetimes of the transient absorption signal of graphene oxide (GO), reduced (1 hour) graphene oxide (RGO-1) and reduced (for 24 hours) graphene oxide (RGO-2) and	171

at 670 nm after exciting at 400 nm laser light.

6.3 Fits of the time traces monitored at 460nm (Exciton Bleach). 175

6.4 Fits of the time traces monitored at 460nm (Exciton Bleach in presence of electron quencher). 177

LIST OF SCHEMES

Scheme Number	**Scheme Caption**	**Page Number**
3.1	Schematic Diagram representing the electron transfer dynamics in both TiO_2 nanoparticle and TiO_2 quantum dot sensitized by alizarin in toluene. It shows multiexponential injection and slow back ET on quantum dot surface and single exponential injection and faster back ET on nanoparticle surface.	100
5.1	Schematic representation of the energy level (both valence band and conduction band) of CdSe and ZnTe bulk semiconductor, where energy levels are shown with respect to vacuum. Charge transfer and cooling dynamics are depicted in the diagram	148
6.1	Schematic of Electron Transfer Process	179

ABBREVIATIONS

BET	**Back electron transfer**
BQ	**Benzoquinone**
CB	**Conduction band**
CCD	**Charge coupled device**
CdS	**Cadmium sulfide**
CdTe	**Cadmium telluride**
CdSe:	**Cadmium selenide**
CR	**Charge recombination**
CT	**Charge transfer**
DSSC	**Dye sensitized solar cell**
e^-	**electron**
ET	**Electron transfer**
fs	**Femtosecond**
h	**hole**
HOMO	**Highest occupied molecular levels**
HRTEM	**High Resolution Transmission Electron Microscopy**
IET	**Interfacial electron transfer**
IPA	**Isopropyl alcohol**
LUMO	**Lowest unoccupied molecular levels**
MEG	**Multiple Exciton Generation**
MPA	**3-mercaptopropionic acid**
NaOH	**Sodium hydroxide**

NCs	**Nanocrystals**
NPs	**Nanoparticles**
NHE	**Normal hydrogen electrode**
nm	**nanometer**
PD:	**Photodiode**
Py	**Pyridine**
QDs	**Quantum dots**
Qz	**Qunizarin**
SAED	**Selected Area Electron Diffraction**
SHG:	**Second harmonic generation**
TCSPC	**Time correlated single photon counting**
TEM	**Transmission Electron Microscopy**
VB	**Valence band**
WLG:	**White light generation**
XRD	**X-ray diffraction**
ZnS	**Zinc sulfide**
ZnTe	**Zinc telluride**

Chapter 1

Chapter 1

Introduction

1.1. Nanotechnology Before 20th Century

“Small is different” from the materials science perspective was realized much before Feynman’s famous talk “There's Plenty of Room at the Bottom" at an American Physical Society meeting at Caltech on December 29, 1959 [1.1]. Indian craftsmen several centuries back have used nanotechnology without realizing that the enhanced tensile strength of the swords (with high carbon) that they made comes from presence of tube forms of carbon in Wootz Steel. In fact term Wootz is westernized term for ukku in kannada and ekku in tamil [1.2]. The fact that nanotechnology was utilized by Indian craftsmen in not only Wootz steel, but also in paintings was pointed out by Robert Floyd Curl, Jr., Nobel Prize Winner in Chemistry in 1996 [1.3]. Other more famous early example of nanotechnology is Lycurgus cup which derives its color due to gold nanoparticles embedded in the glass. Michael Faraday in 1857 Michael Faraday was first to realize that size is responsible for unique optical properties of gold colloids. However the theoretical framework for describing properties was provided by Mie decades later, which correctly predicted that the color comes from varied scattering properties of metal nanoparticle arising from oscillation of conduction electrons on the nanoparticle surface called Surface Plasmon resonance. Today we know that not only size but also shape of metal nanoparticles significantly influences optical properties. Such unique properties in semiconductors were not recognized until 1981 when Ekimov et al [1.4] showed size dependent optical properties in a glass matrix. Later Brus et al proved size dependent effects in CdS colloidal solutions [1.5]. The size dependent effect in semiconductors was attributed to what is now called size quantization effect. Size quantization effect refers to the increase in band gap of semiconductors with decreasing size. Brus et al [1.6] and Efros et al [1.7] independently provided theoretical framework for this observation. It was immediately realized that size quantization effect provided us a way to control the electronic property of materials, which is immensely beneficial in different applications eg. photovoltaics [1.8], biological tagging [1.9], optoelectronics [1.10] and Quantum computing [1.11].

It was realized from UV-Visible absorption spectroscopy that size quantization effect was seen only below a particular size regime [1.5]. Size quantization effect can be explained on the basis of factors determining the electronic structure of bulk crystals. In a bulk crystal, electron and holes move in a potential created by the lattice ions. This potential is unique not only due to local bonding arrangement but also to lattice potential created due to periodicity of the lattice. Therefore the motion of charge carriers in the crystalline solid will be governed by this lattice potential. The lattice potential not only imparts a unique electronic dispersion but also governs its transport property like coherence length. Coherence length is the distance to which a carrier can travel before it scatters. In a semiconductor solid similar to charge carriers the exciton (electron-hole pair) behaves as a composite particle with a reduced mass arising from electron and holes. Therefore an exciton also has coherence length or mean free path in a particular crystal lattice. This characteristic length is also called Bohr radius of the exciton. Size quantization effect is observed for crystallite size below Bohr radius. Bohr Radius of exciton is a material property it varies from fraction of nanometers to several tens of nanometers. In bulk crystals size does not control electronic characteristics because the size of the crystal is much larger than the Bohr radius of the exciton. Bohr radius will become a function of the crystal size for sizes lower than this. In other words we can say that the wave function of the exciton will also be a function of radius of a nanoparticle. Additionally, as one reduces the radius the energy level spacing between valence and conduction band becomes larger. Additionally formation of discrete bands (valence and conduction bands) can be seen.

The discreteness of the individual bands leads to not only significant alteration of steady state properties like absorption and luminescence but also dynamical properties like carrier cooling, carrier relaxation etc. In fact it was proposed by Nozik et al [1.12] that in small nanostructures within size quantization regime carrier cooling will be hindered due to what is called as phonon bottleneck effect. The cooling times for size quantized structures were expected to be several ns. However ultrafast dynamics studies in small nanocrystals showed that cooling dynamics of carriers was still much faster (~few ps) which was explained on the basis electron-hole energy transfer and surface mediated cooling [1.13]. Apart from cooling of carriers, recombination also is significantly influenced by surface due to very large number of surface sites which might trap carriers. These microscopic variables like cooling and trapping times are ultimately related to macroscopic properties like photovoltaic efficiency, luminescence quantum yield etc. Therefore understanding the dynamics is imperative. In view of above mentioned factors and motivated by potential applications of nanomaterials it is necessary to understand what governs the dynamics, so that a better control over the properties of nanomaterials can be achieved. To control dynamics it is imperative to know how lower dimensionality affects electronic structure of a nanoparticle.

1.2. Physics of Semiconductors

1.2.1. Introduction

Before describing how dimensionality influences electronic structure it is necessary to understand the basics of semiconductors. Semiconductors by virtue of the electronic structure are materials which has forbidden zone between valence and conduction band. The difference in the energy between the valence band maxima and conduction band minima is called as band gap. The evolution of the electronic structure depends on interaction between atoms or ions comprising crystal lattice. This interaction eventually leads to overlapping electron clouds between adjacent lattice atoms which in turn splits the energy levels as shown in Fig.1.1.

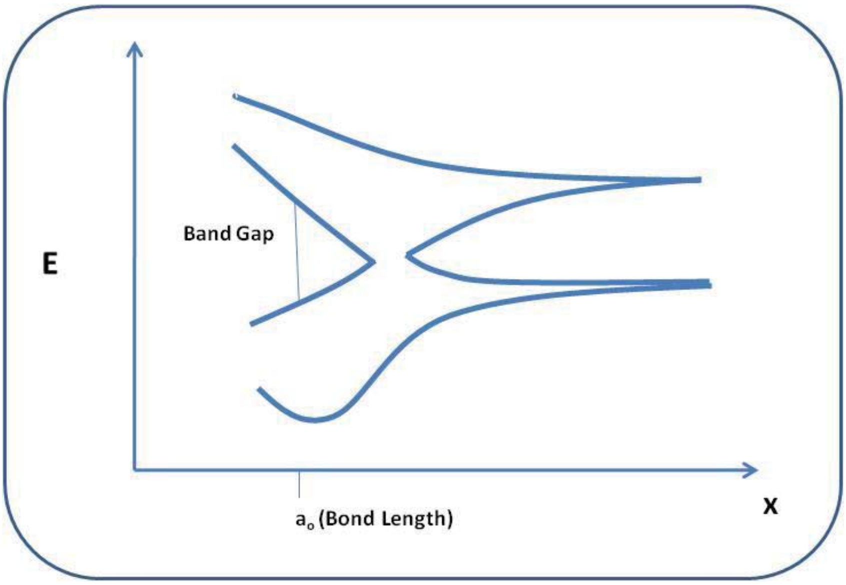

Figure 1. 1. Schematic of Energy Band in a typical semiconductor versus bond length

It is clear from the figure that the region not bounded by overlapping potential energy curves is empty i.e. there are no energy levels between the two bands. Secondly in figure 1.1 at the bond length marked in the figure there is a forbidden zone indicating that at that bond length, the material is a semiconductor. Understanding this splitting of potential energy curves requires a quantum mechanical treatment of system.

Charge carriers are subjected to a periodic component due to crystal structure. Therefore the wave function also should have a periodically varying component. These functions are called Bloch functions which automatically take into account periodicity of the lattice. Simplest model describing the semiconductor system is called Kronig-Penney model which is a modified particle-in-a-box type of treatment.

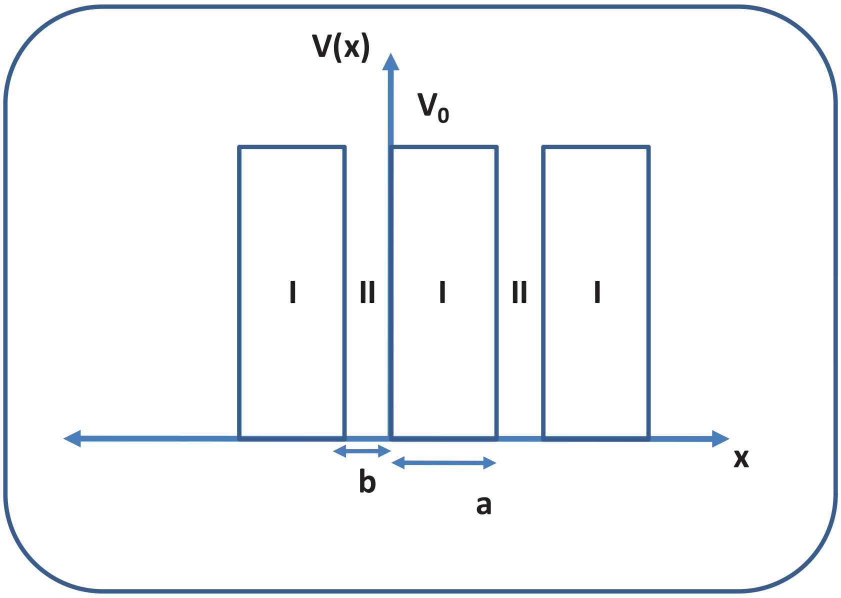

Figure 1. 2. Potential in Kronig-Penney model.

As seen from the schematic, potential barrier height is V_0 and barrier width is ‘a’. Potential repeats itself with a period of x=a+b=c. Since potential is periodic, wave function also has the same periodicity. Width of region II is ‘b’.

The Schrödinger’s equation can be set up for a single electron trapped in this periodic potential as follows,

$$H\psi = -\left(\frac{\hbar^2}{2m}\frac{d^2}{dx^2} + V(x)\right)\psi = E\psi \tag{1.1}$$

Since the potential varies in two different regions we can set up Schrödinger’s equation for the two regions as given below,

$$\begin{aligned} &\frac{d^2\psi}{dx^2} + \frac{2m}{\hbar^2}\left(E - V_0\right)\psi = 0 && \text{Region I} \\ &\frac{d^2\psi}{dx^2} + \frac{2m}{\hbar^2}E\psi = 0 && \text{Region II} \end{aligned} \tag{1.2}$$

The general solution for the above equations can be represented as

$$\begin{aligned} \psi_I &= Ae^{i\beta x} + Be^{-i\beta x}, \beta = \left(\frac{2m(E - V_0)}{\hbar^2}\right)^{1/2} \\ \psi_{II} &= Ce^{i\alpha x} + De^{-i\alpha x}, \alpha = \left(\frac{2mE}{\hbar^2}\right)^{1/2} \end{aligned} \tag{1.3}$$

The coefficients A, B, C and D can be determined by boundary conditions and normalization procedure.

The boundary conditions are both ψ and $\frac{d\psi}{dx}$ are continuous functions of x at the boundaries. Applying boundary conditions and Bloch function as given below we arrive at,

$$\begin{aligned}
&\psi_k(x) = u_k(x)e^{ikx} \\
&\cos(kc) = F \\
&F = \cos(\alpha b)\cos(\beta a) - \frac{\beta^2 + \alpha^2}{2\alpha\beta}\sin(\alpha b)\sin(\beta a)
\end{aligned} \tag{1.4}$$

The above equations show that real solutions only exist for $|F| < 1$ and the solution is wavelike. The gaps between these discontinuities are forbidden regions where no real solution exists. This treatment while being instructive as a paradigm for evolution of electronic structure in a periodic lattice, it does not include various complications that arise in the case of a charge carrier in solids. For example potential is not square well, electron at one lattice site interacts with nearby electrons and lattice site, furthermore electron- electron correlations introduces more complications. In a bulk semiconductor the potential varies along different directions. Therefore the dispersion of electrons along different directions is expected to be different. These complications were innovatively resolved in bulk semiconductors by using effective mass model. This model uses an approximation where the electrons and holes are assumed as free particles with different masses as compared to free electron mass or in other words the dispersion is assumed to be parabolic near k=0 or at zone center. The effective mass of charge carriers is a combined effect of all interaction of charge carriers in the crystal lattice.

1.2.2 Effective Mass Approximation

As mentioned previously Bloch functions are taken as Eigen functions to solve Schrodingers Equation for a solid [1.14]. Therefore wave function in a 3-D solid is given by

$$\psi_k(r) = u_k(r)e^{ikr} \tag{1.5}$$

Substituting this in Schrödinger's equation we get,

$$\left(\frac{p^2}{2m} + \frac{\hbar(k.p)}{m} + \frac{\hbar^2 k^2}{2m} + V\right)u_{nk} = E_{nk}u_{nk} \tag{1.6}$$

At regions close to the zone center we can write the energies using parabolic approximation as follows

$$E_{nk} = E_{n0} + \frac{\hbar^2 k^2}{2m^*} \tag{1.7}$$

Effective mass can be written as

$$\frac{1}{m^*} = \frac{1}{m} + \frac{2}{m^2 k^2}\sum_{n' \neq n}\frac{|\langle u_{n0}\,|\,k.p\,|\,u_{n'0}\rangle|^2}{E_{n0} - E_{n'0}} \tag{1.8}$$

It is clear from the above relationship that the effective mass is a combined effect of mass and potentials experienced by the electron. Effective mass is tensor due to different dispersions along different symmetry axes.

$$\frac{1}{m^*_{ij}} = \frac{1}{\hbar^2}\frac{\partial^2 E_{k=o}}{\partial k_i \partial k_j} \tag{1.9}$$

1.2.3 Effect of 3-Dimensional Confinement on Electronic Structure

From the previous sections of this chapter it was assumed that wave function is only dependent on the periodicity and the potentials experienced by charge carriers. Therefore it is necessary to ask, how does dimensionality influence wave function?

In the previous sections the discussion was centered on description of electronic structure in a Bulk or an Infinite crystal. In an ideal bulk crystal the electronic structure impart a coherence length or mean free path (a_b) for the charge particle. When the radius of the particle is lesser than this characteristic length i.e. $r < a_b$, the coherence length of charge carriers will be a function of radius. Additionally the charge carriers in a semiconductor i.e. electrons and holes confined within a small radius can also interact with each other by coulomb interaction and form a composite particle called the exciton. The exciton has a different coherence length as the reduced mass of exciton is different. How can one treat an Exciton in a confined solid?

The first attempt at solving this problem was carried out using the simple particle trapped in a sphere model (3-D Confinement) [1.6, 1.7], where the particle was assumed to be trapped in a potential well with infinite barriers. The crystal structure of the confined system is assumed to be unchanged, one can write the wave function by using Bloch function $u_{vk}(r)$,as

$$\psi(r) = u_{vk}(r)\varphi(r) \tag{1.10}$$

In the absence of degeneracy near the zone centre, neglecting coloumb interaction and using parabolic dispersion we can write the Hamiltonion as

$$\hat{H} = -\frac{\hbar^2}{2m_e}\nabla_e^2 - \frac{\hbar^2}{2m_h}\nabla_h^2 + V_e(r_e)V_h(r_h) \tag{1.11}$$

The confining potential for electron is given by

$$V_e(r_e) = \begin{cases} 0 & for\,|r_e| < a \\ \infty & for\,|r_e| < a \end{cases} \tag{1.12}$$

Similar potential is used for holes.

Since we assumed coulomb interaction is absent we can write the envelope wave function as

$$\varphi(r_e, r_h) = \varphi_e(r_e)\varphi_e(r_h) \tag{1.13}$$

The solution to the problem can be obtained in terms of Bessel functions for the Radial Part and spherical harmonics for angular part as given below

$$\varphi_{n,l,m}^{e,h}(r) = Y_{l,m}\sqrt{\frac{2}{a^3}}\frac{J_l\left(\chi_{n,l}\frac{r}{a}\right)}{J_{l+1}\left(\chi_{n,l}\right)} \tag{1.14}$$

Where n can take values 0, 1, 2, --- and l=0, 1, 2, ---and m values are given by $-l \le m \le l$.

$\chi_{n,l}$ is the n^{th} order of J_l . Applying the boundary condition we arrive at Energies

$$E_{n,l}^{e,h} = \frac{\hbar^2}{2m_{e,h}}\frac{\chi_{n,l}^2}{a^2} \tag{1.15}$$

It is clear from the energy Eigen values that discreteness evolves from continuum of states on introducing confinement. The shift from the bulk values can be given by

$$\Delta E = \frac{\hbar^2}{2\mu}\frac{\pi^2}{a^2} \tag{1.16}$$

μ is the reduced mass of electron-hole pair.

The above energy shift arises from confinement of carriers and is positive indicating that there will be a positive energy shift with confinement or in other words the band gap increases.

In the above treatment we have neglected coulomb interaction, however this problem can be solved by looking at scaling of coulomb interaction with radius as compared to confinement energy. The coulomb interaction scales inversely with radius, r and confinement energy varies with inverse r^2. This clearly indicates that coulomb interaction can be approximated as a correction factor to the above obtained Eigen values. Coulomb interaction acts only as a correction factor in small nanocrystal. This interacting electron hole pair is now called an exciton. When a semiconductor radius decreases from infinite to confined solid where mean free path is close to radius, coulomb interaction has a significant role to play. Theoretically this interplay between confinement energy and coulomb interaction leads to three different confinement regimes. Before going into effects of degree of confinement we define the mean free path of the exciton (a_B , also called Bohr Radius of the exciton) as

$$a_B = \frac{\hbar^2 \varepsilon}{\mu e^2} \qquad (1.17)$$

Based on a_B and attractive coulomb interaction we can define three kinds of weak (r> a_B), intermediate confinement (r~ a_B) and strong confinement (r< a_B) [1.16]

Weak Confinement Regime: In this regime confinement energy is less than coulomb interaction or Exciton binding energy. The band gap in this case can be given as

$$E_{QD} = E_B - E_c + \frac{\hbar^2 \pi^2}{2(m_e + m_h)a^2} \qquad (1.18)$$

Intermediate Confinement Regime: In this size regime confinement will be set in the carrier with smaller effective mass. Very often electrons have a low

er effective mass; therefore in such a size regime electron levels will exhibit discreteness while the hole levels will be continuous. Therefore the system may be approximated as a donor type exciton with electron governing quantization behavior.

Strong Confinement Regime: In this size regime, exciton as a whole experiences confinement leading to quantization of exciton levels.

$$E^{EX}_{n_e,l_e,n_h,l_h} = E_B + \frac{\hbar^2}{2a^2}\left(\frac{\chi^2_{n_e,l_e}}{m_e} + \frac{\chi^2_{n_h,l_h}}{m_h}\right) + E_c \qquad (1.19)$$

In the equation 1.19, E_c coulomb energy is given by $\frac{1.8e^2}{\varepsilon a}$ for the 1S states. The selection rules for optical transition are given by ($\Delta n = 0, \Delta L = 0$).

As mentioned before, above theoretical treatment oversimplifies the electronic structure. A realistic description of the electronic structure requires treatment of near the zone center and non parabolicity of the bands.

1.2.3 Confinement Effect in Real Band Structures

The model described in the previous sections introduced effect of confinement under assumption of parabolic dispersion and non degenerate band. However, real systems are seldom parabolic or nondegenerate. The present thesis deals with dynamics in II-VI semiconductors. Therefore we use the specific example of CdSe to illustrate such complexities. In CdSe, the conduction band is composed of 5s orbitals of Cd which is nondegenerate. However the valence band is composed of 4p orbitals of Se, therefore, it has a 6-fold degeneracy. In such a system, strong spin-orbit interaction lead to removal of degeneracy at k=0 arising from. Therefore, at zone center, valence band splits into $J = 1/2$ and $J = 3/2$. $J = 1/2$ is called split-off band [1.16]. Additionally for $k \neq 0$, J=3/2 sub bands further splits into $m_j = \pm 1/2$ $m_j = \pm 3/2$. m_j is projection of J along z-axis. $m_j = \pm 3/2$ is called heavy hole due to larger effective mass and $m_j = \pm 1/2$ is called light hole. For CdSe with hexagonal structure light and heavy hole bands split at $k = 0$ due to crystal field asymmetry. At $k = 0$ spin orbit coupling is 0.42eV and for hexagonal crystal split between light and heavy hole is 25meV for CdSe (see figure 1.3).

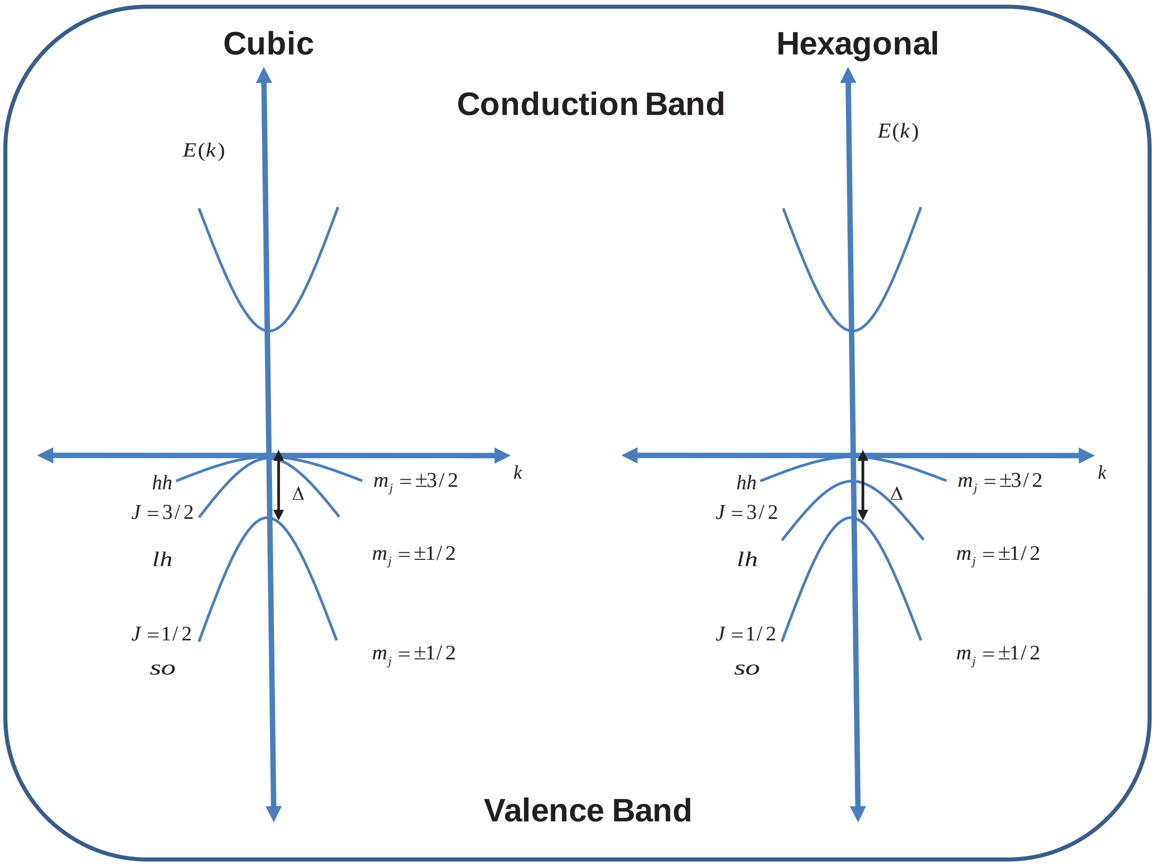
Cubic
Hexagonal
Conduction Band
$E(k)$
$E(k)$
k
k
hh
$J = 3/2$
lh
$J = 1/2$
so
$m_j = \pm 3/2$
$m_j = \pm 1/2$
$m_j = \pm 1/2$
Δ
hh
$J = 3/2$
lh
$J = 1/2$
so
$m_j = \pm 3/2$
$m_j = \pm 1/2$
$m_j = \pm 1/2$
Δ
Valence Band

Figure. 1.3. Typical Band Structure of Cubic and Hexagonal CdSe, where hh=Heavy Hole Band, lh=Light Hole Band, SO-Split-Off Band. These bands are also referred to as A, B, and C respectively.

As described above, complications introduced to band structure complicates theoretical treatment of such systems. One of the most familiar approaches to band structure computation is $k.p$ method, which is based on effective mass approximation. Within this framework it is possible to obtain dispersion curves for values close to k=0 by solving analytically. This approach includes effect of spin orbit coupling and more importantly non spherical symmetry of field. The approach used for calculating band structure when degeneracy is present was first developed by Luttinger and Kohn. The model is called Lutinger-Kohn Model. The model was particularly used to describe semiconductors with cubic symmetry [17, 18] and is particularly suited to describe II-VI semiconductors like CdS, CdSe, CdTe. This model included triply degenerate valence band.

Another interesting feature of the model is that it can describe the effect of coupling of states in valence bands. This clearly showed that $F=L+J$ is a good quantum number [1.16]. Based on this model electronic states are denoted for electrons and holes as nL_e and nL_F, where n is the principle quantum number, L is the minimum orbital quantum number and F is the total angular momentum ($F=L+J$, $J=L+S$). Therefore different electron states can be described as *1Se, 2Se, 3Se,* etc; and hole states can be described as $1S_{1/2}$, $1S_{3/2}$, and $1P_{3/2}$ etc. electron hole pair or exciton are $1S_e\ 2S_{3/2}$, $1S_e\ 1S_{3/2}$, $1S_e$-$1P_{1/2}$, etc [16].

1.2.4. Dimensionality and Density of States (DOS)

Density of states refers to number of states within an energy interval. It is one of the most important parameter defining not only steady states properties but also dynamics properties like relaxation. We derive the DOS for a bulk system as follows. Assuming particle in a confined potential of free electron model, the boundary conditions leads to

$$k_x = \frac{2\pi}{L} n_x, k_y = \frac{2\pi}{L} n_y, k_z = \frac{2\pi}{L} n_z \qquad (1.20)$$

In the above solutions n are real values

Therefore volume per state is given by,

$$k = \frac{8\pi^3}{V} \tag{1.21}$$

It can be seen that the above expression is true even when $L_x \neq L_y \neq L_z$. The total number of filled states can be written as,

$$N = 2 \times \frac{4\pi}{3} \times k_f{}^3 \times \frac{V}{8\pi^3} , \tag{1.22}$$

where k_f is k for Fermi level. Factor of 2 come from two spin states.

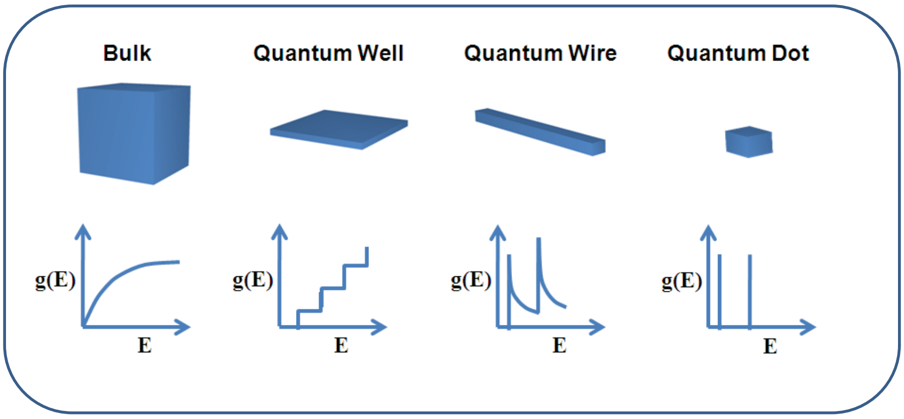

Figure 1.4. Schematic of DOS in different confined systems.

Electron Density therefore is given by

$$N = 2 \times \frac{4\pi}{3} \times k_f{}^3 \times \frac{V}{8\pi^3} \tag{1.23}$$

As mentioned above DOS can be given by,

$$g(E) = \frac{1}{V} \frac{\partial N}{\partial E} \tag{1.24}$$

Assuming a parabolic dispersion we arrive at,

$$g(E)=\frac{\sqrt{2Em^3}}{\pi^2\hbar^3} \qquad (1.25)$$

For a Quantum Well where in two dimensions particles are free, we can write DOS as

$$g_{2D}(E)=\frac{m}{\pi\hbar^2} \qquad (1.26)$$

For Quantum Wire DOS is,

$$g_{1D}(E)=\frac{1}{\pi\hbar}\sqrt{\frac{2m}{E}} \qquad (1.27)$$

For Quantum Dots levels are fully discrete.

Below schematic in fig 1.4 gives DOS versus E for different dimensionality.

1.3. Carrier Relaxation in Quantum Dots

In the previous section, discussion was mainly concentrated on the effects of quantization on electronic properties. These changes in electronic properties not only affect steady state properties but also affect dynamics properties. Several studies have shown how relaxation dynamics in quantum dots are unique. Understanding the relaxation mechanisms helps in achieving a degree of control over properties which in turn helps in optimizing performance of devices constructed from quantum dots.

On photoexcitation with $h\nu = E_g$ (Band Gap) of the semiconductor, electrons and holes are produced in Conduction and Valence Band respectively. In bulk semiconductors energy spacing within individual bands are smaller than thermal energy therefore cooling (relaxation in individual bands or intraband transitions) can happen via a phonon emission processes. In a quantum confined system the spacing in the individual bands are very often much larger than phonon energies. Therefore cooling is dominated by several alternate mechanisms as described below.

1.3.1. Phonon mediated mechanism

As mentioned above in a semiconductor cooling can be mediated by longitudinal optic (LO) phonons by Froehlich’s interaction and via acoustic phonons by deformation and piezoelectric potentials with different energy loss rates for above mentioned phonon mediated routes [1.19, 1.20]. In a confined system lowest confined levels especially for electrons in conduction band can be hundreds of meV, however typical phonon energies are of the order of 20 meV. Therefore relaxation can only be mediated by multiple phonon emission; however this process might be hindered severely due to restrictions placed by energy and momentum selection rules. This restriction imposed by selection rules can be to some extent overcome due to larger surface to volume ratio, therefore scattering from surface can play an important role in relaxing or violating selection rules, however, multiphonon relaxation requires $\Delta E = nE_{LO}$ (where ΔE is energy spacing for intraband transition and E_{LO} is energy of LO phonon). However the probability of this transition occurring by multiphonon emission is low and therefore cooling is expected to be severely hindered leading to what is called as phonon bottleneck. Another way out of this situation is multiphonon mediated by simultaneous release of acoustic (LA) and optic (LO) phonon [1.21]. However this mechanism also is delayed due to involvement of acoustic phonons.

1.3.2. Electron-Hole energy transfer mechanism

In most semiconductors the electron effective mass is much smaller than hole effective mass, this leads to a flat dispersion curve for holes or in other words DOS in valence band is much higher compared to DOS in conduction band. Additionally, valence band is degenerate in II-VI semiconductors like CdSe, CdTe etc. This degeneracy also contributes towards greater DOS of valence band. Therefore intraband transition in valence band is much faster than intraband transition in conduction bands. Therefore a coulomb interaction can transfer energy from electron to holes leading to faster cooling of electrons. In fact several studies have confirmed involvement of this mechanism in cooling [1.22, 1.23] (see fig.1.5).

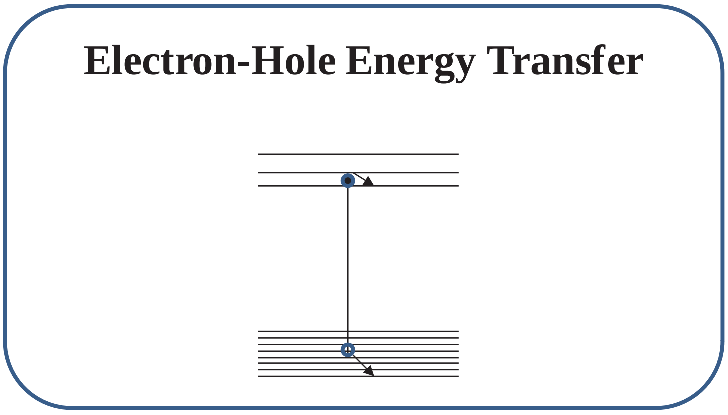

Figure 1.5. Schematic of electron-hole energy transfer process.

1.3.3. Multiparticle Auger Processes

This mechanism also is an energy transfer process by which if there are more than two particles in a quantum dot and excess energy is transferred to third particle. It is clear that such a process is involved in relaxation only under high intensities. Involvement of such process has also been experimentally verified [1.24]. Below given schematic (fig 1.6) represents one such process.

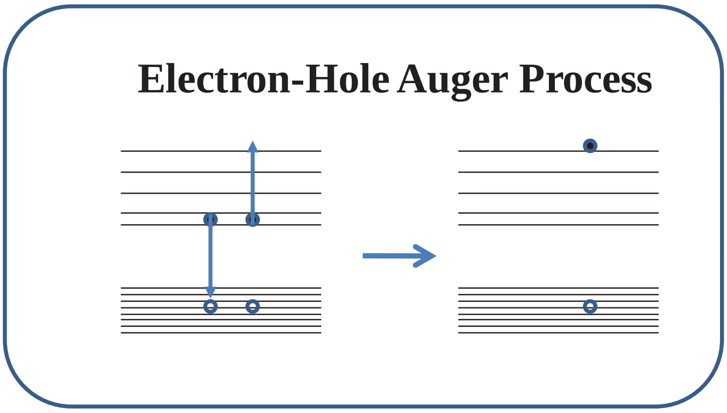

Figure 1.6. Schematic of electron-hole Auger process.

1.3.4. Impact Ionization

Impact ionization refers to relaxation of hot carriers by production of cold multiple electron- hole pairs. Since the energy required for creation of two electron-hole pair is twice the band gap approximately.

The excitation energy must be much larger than the two times band gap. Such a process is known to occur in cases where other cooling mechanisms are suppressed. In the case of lead salt semiconductors like PbS, PbSe etc this has been conclusively proved. In these cases it was observed that electron and hole effective masses are similar and other process like energy transfer is suppressed (fig 1.7.).

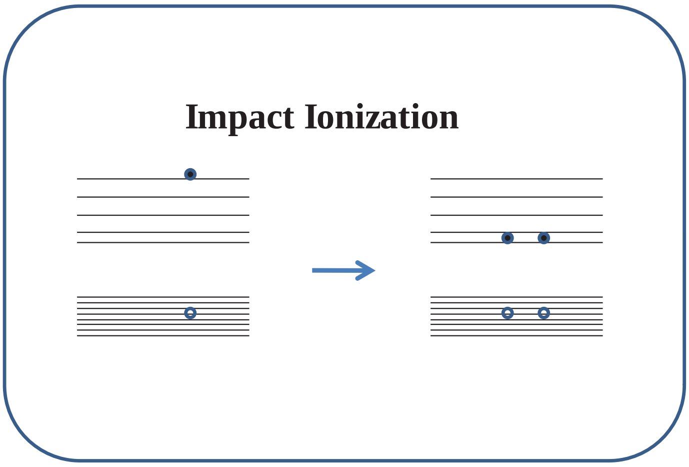

Figure 1.7. Schematic of Impact Ionization Process

1.3.5. Defect Mediated Relaxation

Surface to volume ratio in a nanoparticle is very high, which leads to creation of defects at surface. The defects could arise from dangling bonds, surface reconstruction, capping agents etc. If these defect states arise within mid gap region i.e. between the two bands then they can influence carrier relaxation by trapping the carrier [1.23]. In some cases defects can also have levels within the individual valence and conduction bands. Such defect states are called surface resonances. These states can also involve in aiding cooling of carriers.

1. 4. How Can QDs Help in Solar Cells?

One of most important application of QDs is in the field of photovoltaics which has in recent time gained much importance due to energy crises as green approach to solve the energy crises. Photovoltaic effect was first observed by E. Becquerel [1.28]. Photovoltaic technology involves use of a mediator which absorbs solar light and converts that to electricity. This forms the basis for a *solar cell or photovoltaic cell* and material that acts as a mediator is a semiconductor. The semiconductor on exposure of light creates electrons and holes in the CB and VB which has to be separated before recombination to build and efficient solar cell. The separation of electrons and holes created in photovoltaic cells can be achieved by forming and inbuilt field. Solar cells are usually divided into three generations. The first generation solar cells consisted of mainly silicon. Cell is achieved by creation of a pn junction from Si. Such cells are known to be efficient with efficiency ~24%. However cells are to be of electronic grade which means their purity should be extremely high. Therefore it is very expensive. The second generation solar cells consists of thin film based cells mainly consisting of poly-silicon, amorphous silicon, Copper Indium Selenide and Cadmium Telluride. These cells are comparatively cheaper but have a lower efficiency ~19%. The third generation solar cells are based on polymers, nanocrystals and dye sensitized solar cells. Dye sensitized solar cells use wide band gap semiconductor like TiO_2 and ZnO. The semiconductors do not absorb visible light. The light is absorbed by a dye which transfers charges to semiconductor and HOMO of cell is replenished by a redox electrolyte (see figure 1.8.). One of the first studies on influence of mechanistic aspects electron transfer reactions in a cell was carried out by Gerischer and Memming [29-30]. These studies clearly showed potentials of a dye sensitized solar cell. In 1990s, Michael Graetzel in $Ru(dcbpy)_2(NCS)_2$ [dcbpy=(4,4’-dicarboxy-2,2’-bipyridine] or (Ru-N3) dye sensitized mesoporous TiO_2 nanoparticles reported conversion efficiency of ~11% in a iodine/iodide based redox electrolyte [32]. The schematic shown in figure 1.8 describes different processes occurring in a DSSC. The efficiency of a DSSC depends on factors like electron injection time, efficiency of electron injection, free energy for back electron transfer (BET) etc. Though significant understanding on mechanistic aspects has been achieved, the efficiency has not improved from ~11%. Quantum dots have significant potential in photovoltaics due to ability to tune electronic structure by size [1.32-1.34]. Therefore V_{OC} can be tuned by just changing the size. Additionally use of wide band gap QD in a DSSC also can lead to improvements as BET process is expected to be delayed according to theory as free energy for BET increases. FET and BET process are interfacial electron transfer phenomena which can be controlled by proper choice of semiconductor and dyes with anchors to adsorb on to semiconductor, therefore, leading to possibly control performance of devices.

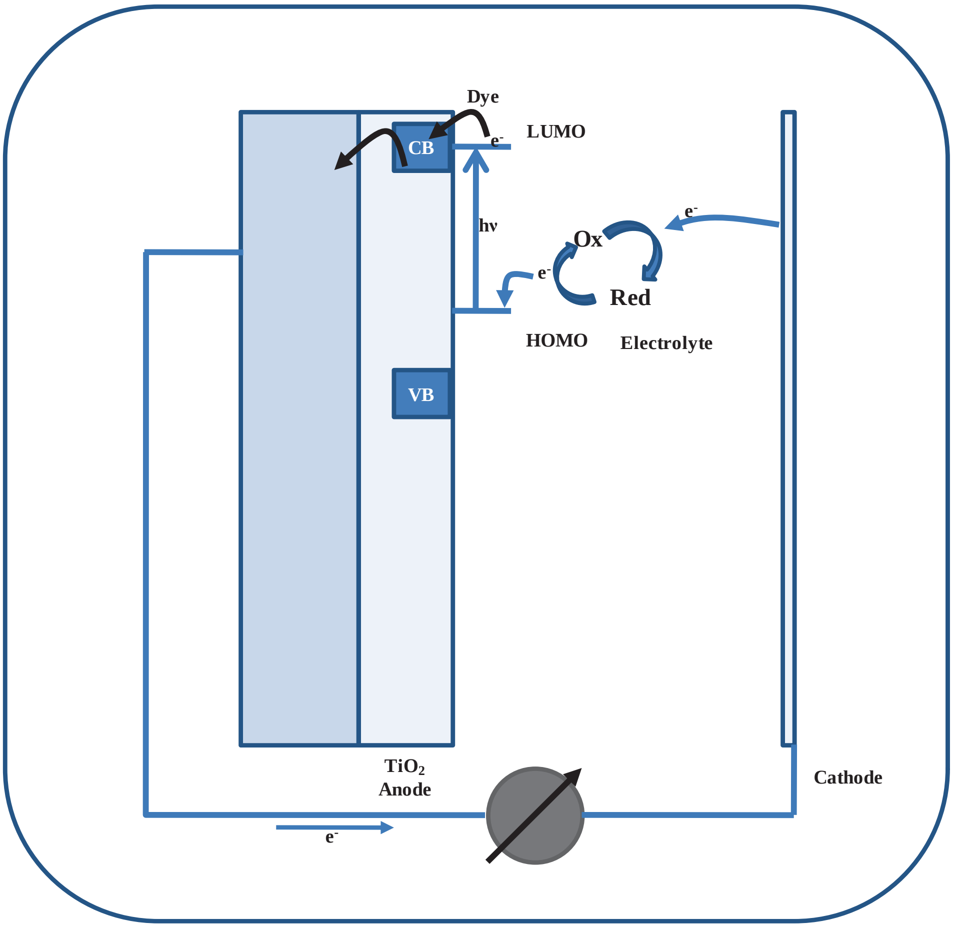

Figure 1. 8. Schematic of Dye Sensitized Solar Cell

1.5. “Improving on” QDs

As mentioned earlier QDs offer opportunities in several thrust areas of research due to tunability of properties with size. However large number of surface ions on a QD could lead to formation of traps leading to loss of carriers. Additionally since carriers are confined within a small volume the interaction between them is strong which leads to nonradiative relaxation which also can be detrimental to any device application. Some of these problems can be overcome by creation of heterostructures suited for that particular purpose. Some typical heterostructures which are used commonly to “improve on” QDs are described below.

1.5.1. Semiconductor-Semiconductor Core Shell Nanostructures

In the previous sections we have described how electronic structure is modified in a QD with size. Here we discuss the implications of how a different semiconductor grown over a quantum dot can influence its properties. It is well known that two different semiconductors have different band alignment and electronic structure. Therefore the band alignment at the interface can significantly alter static and dynamics properties due to several reasons. We list few reasons here (i) growth of another semiconductor can annihilate defects at the interface (ii) since band alignment at interface is different it can produce a charge separation or localization depending on alignment (iii) doping. These effects depend on lattice structure, spacing, band alignment etc.

Most commonly used core shell nanostructure is Type I or Type II heterostructure. In the case of type I nanostructure as described in the figure 1.9, band alignment is in such a way that on photoexcitation carriers are localized in the core. This has an added advantage that carriers are unable to sample the surface leading to less interaction with the surface i.e. if the interface is defect free then non radiative interband relaxation can be significantly reduced. Therefore such an alignment is often used in cases where larger luminescence QY is necessary for e.g. biological tagging.

Some of heterostructure that form such an alignment are CdSe/CdS, CdS/ZnS core shell [1.35]. Type II alignment offers possibility of charge separation. In fig. 1. 6, if core is excited then possibility of hole transfer to shell is free energy driven, however electrons will be localized within core leading to charge separation. Such a heterostructure is of immense importance to solar cells. Typical heterostructures with Type II alignment are CdSe/CdTe, CdSe/ZnTe [1.36].

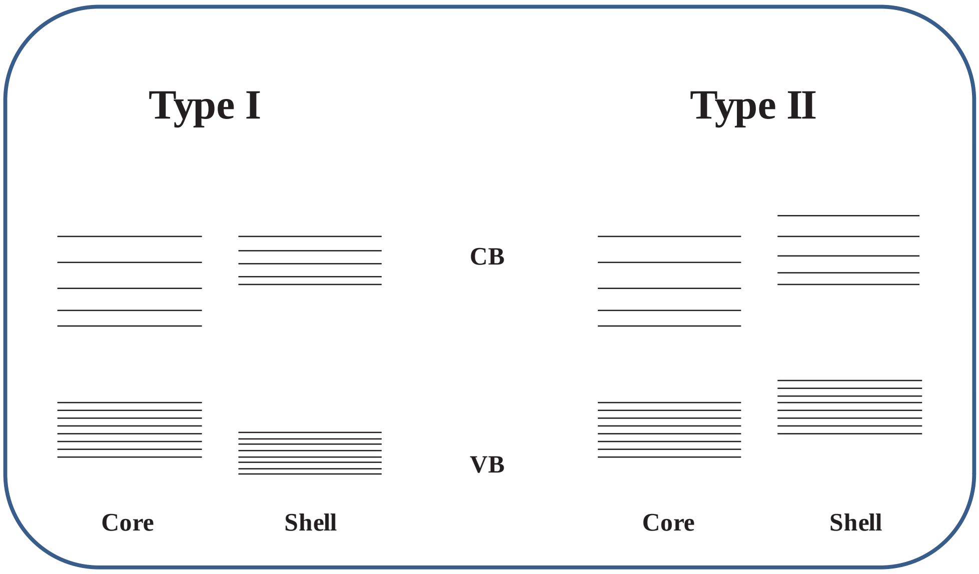

Figure. 1. 9. Schematic of Band Alignment in QD Core Shell

1.5.2. Semiconductor-Dye Nanostructures

There are several approaches in such a nanostructure, one of the approaches being use of dye for separation of carries from quantum dot. We mentioned earlier in section 1.3.4 possibility of generating multiexcitons in a single quantum dot via impact ionization. If one needs to extract these carriers we need another acceptor group which has significant affinity for one of the carriers, thereby leading to faster separation of carriers. In fact such a structure has been shown to exhibit charge separation in picoseconds time scale in CdSe and PbS with methylene blue as electron acceptor [1.37, 1.38]. Additionally other approaches include use of QD as acceptor and dye as donor similar to DSSC. One of the added advantage a quantum dot has is open circuit potential can be tuned by just varying the size of quantum dot.

1.5.3. Metal-Semiconductor Nanostructures

Several studies have shown ability of metal nanoparticles to act as electron sink in metal semiconductor composites due to positioning of Fermi level of metal below conduction band of semiconductor as shown in fig. 1. 10.

Quantitative IPCE measurement show good improvement in case of TiO_2-Au composites [1.39]. Studies on actual charge separation by Mulvaney et al [1.40] revealed that different metal nanoparticles with ZnO behave differently. This study clearly showed that a complete transfer of electrons is not present in silver, gold. In these cases electrons are shared between ZnO and metal. However in the case of Pt a complete charge transfer is achieved. Though metal as an electron sink shows promise, further quantitative analysis of charge separation yield are necessary to better understand efficiency of charge separation process.

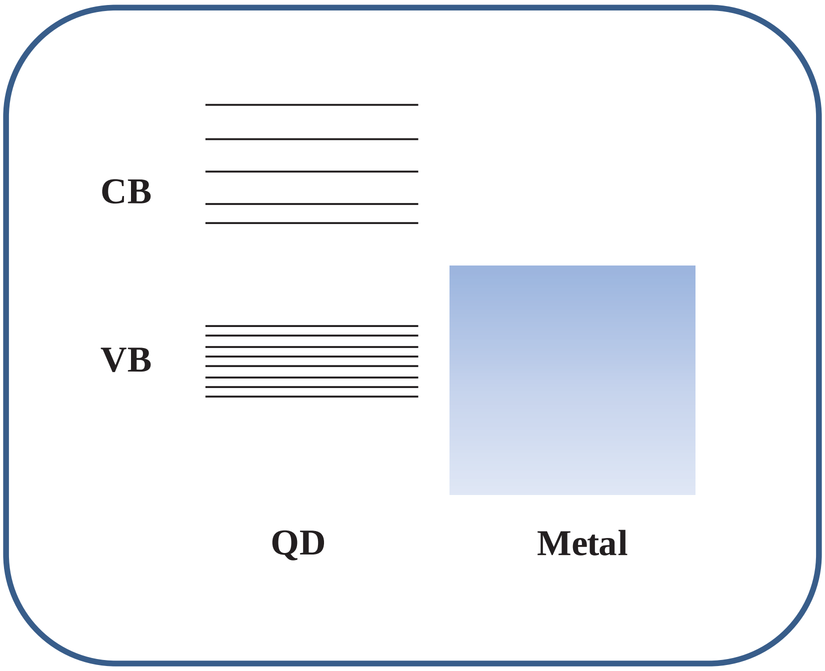

Figure. 1. 10. Schematic of Band Alignment in Metal-QD Composite

Similar to metal semiconductor composites of conducting polymers with quantum m dot have been used for charge separation. Complete inorganic QD based solar cell was first reported by Alivisatos et al [1.41]. Such a structure using polythiophene for hole separation have shown significant promise of conducting polymers in charge separation behavior [1. 41, 1. 42]. Sargent et al have used MEH-PPV, a polyvinylene based polymers for charge separation from lead salt semiconductor.

1. 6. Classical Electron Transfer

Electron transfer plays an important role not only in chemistry but also in various biological processes like photosynthesis, production of ATP etc. In physical sciences well known examples are oxidation of a metal in atmosphere, electron transfer across a metal semiconductor interface etc [1. 43].

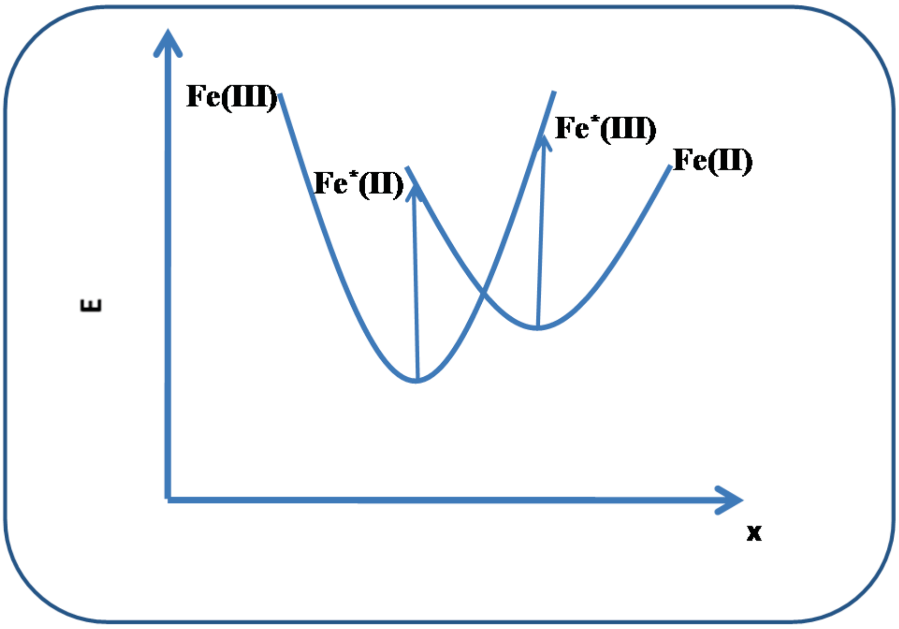

Figure 1.11. Reactant and Product Potential Energy Curves

One of the first approaches towards ET theory was put forward by Libby where he pointed to the importance of Franck-Condon principle in electron transfer involving same inorganic ions in different coordination environments like $Fe(CN)_6^{4-}$. The schematic diagram of how Franck-Condon principle plays a role is given below.

The schematic in fig 1.11 shows that on electron transfer between Fe (III) and Fe (II), the solvent environment around the ions remains unchanged as rate of electron transfer compared to reorganization of solvent molecules is faster. This energy difference arising from a wrong solvent environment acts as solvation barrier. Additionally it can be clearly seen from the figure that bond length in Fe (III) is shorter compared to Fe (II) therefore electron transfer lead to a wrong vibrational environment, this factor also contribute towards energy barrier. Therefore it is clearly apparent that electron transfer involves both change in solvent configuration and chemical structure. It is clear from the above description if we assume that electron transfer takes place from equilibrium configurations we will end up with a different vibrational configuration after electron transfer event. Therefore, such a reaction happening in dark leads to non-conservation of energy. To get away from this conundrum Marcus hypothesized that before electron transfer happens, energies of ions are matched. Additionally energy conservation and validity of Franck-Condon principle is strictly maintained in case of weak interaction between the ions.

1. 6. 1. Adiabatic and Non-Adiabatic Process

Fig 1. 12 gives potential energy surface of reactant and products R and P respectively. The interaction between reactant and product is assumed to be weak therefore splitting is assumed to be < kT. Reactant and product PES is labeled R and P respectively. If the electronic interaction is very weak the splitting at the intersection of the two surfaces is negligible. In the first case the system will always remain on the lowest surface as it moves from left to right such a process is called an adiabatic electron transfer this happens in the case where splitting is large. In the other case as reaction proceeds, the reactant remains in the same potential energy surface. Such a transfer is called non adiabatic process [1. 44].

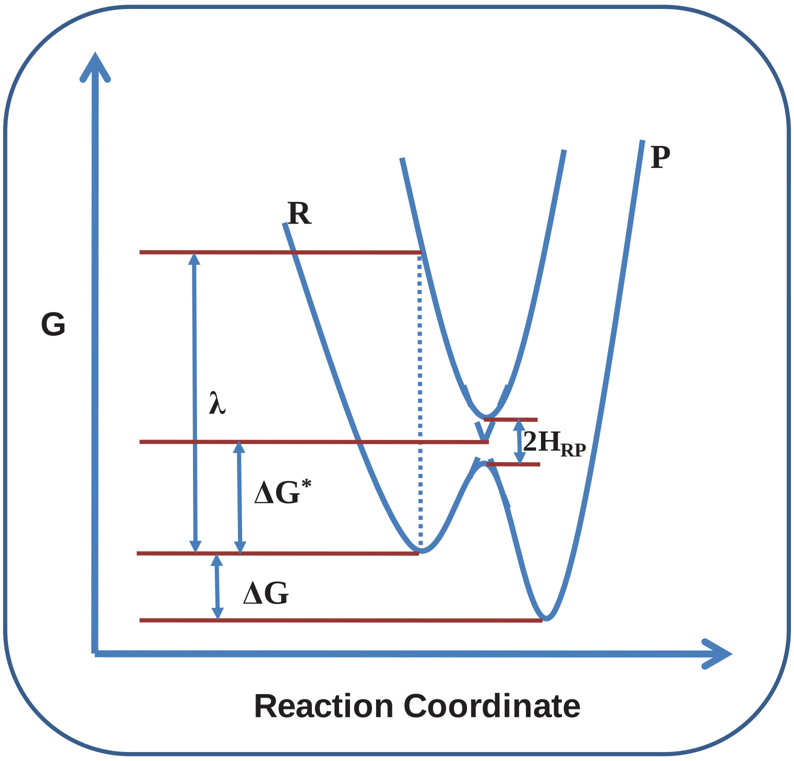

Figure 1. 12. Reactant and Product Potential Energy Curves with Interaction between Curves.

1. 6. 2. Classical Electron Transfer Theory

Fig. 1. 13 represent a plot of energy vs coordinate. ΔG^* is reactant barrier, at this position reactant and product has the same potential energy [1. 44, 1. 45].

$$V_A(q_c)=V_B(q_c) \tag{1.27}$$

Assuming that potential energy curves are parabolic, we can write

$$\frac{1}{2}f(q_c\text{-}q_R)^2=\frac{1}{2}f(q_c\text{-}q_P)^2+\Delta G^0 \tag{1.28}$$

By solving the above equation we can arrive at

$$\Delta G^* = \frac{\lambda}{4}\left(1+\frac{\Delta G^0}{\lambda}\right)^2 \tag{1.29}$$

$$\lambda = \frac{1}{2} f\left(q_A - q_B\right)^2 \qquad (1.30)$$

In equation above λ is called the reorganization energy. As discussed earlier reorganization energy has components of both solvation and vibration and can be written as,

$$\lambda = \lambda_s + \lambda_v \qquad (1.31)$$

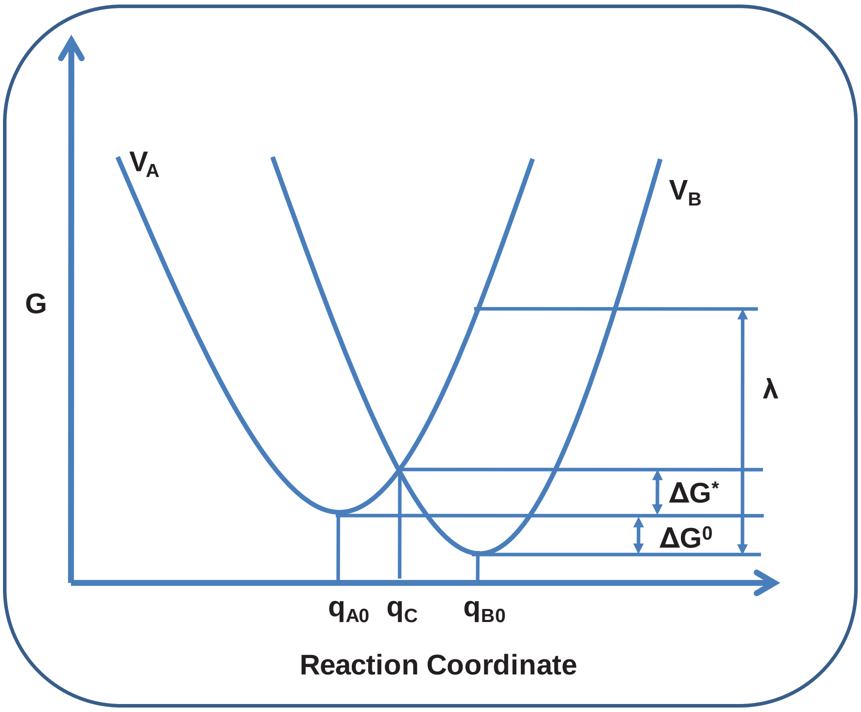

Figure 1. 13. Reactant and Product Potential Energy Surfaces for weak interaction. A= Reactant, B=Product, q_{A0}=Reactant Equilibrium Position, q_{B0}=Product Equilibrium Position

Solvation reorganization energy was obtained by Marcus by assuming solvent as a dielectric continuum.

$$\lambda_s = \left(\Delta e\right)^2 \left(\frac{1}{2a_1} + \frac{1}{2a_2} - \frac{1}{R}\right)\left(\frac{1}{\varepsilon_\infty} - \frac{1}{\varepsilon_0}\right) \qquad (1.31)$$

a_1 and a_2 are radii of donor, acceptor, R is distance between the centres of donor and acceptor. ε_∞ and ε_0 are optical and static dielectric constants.

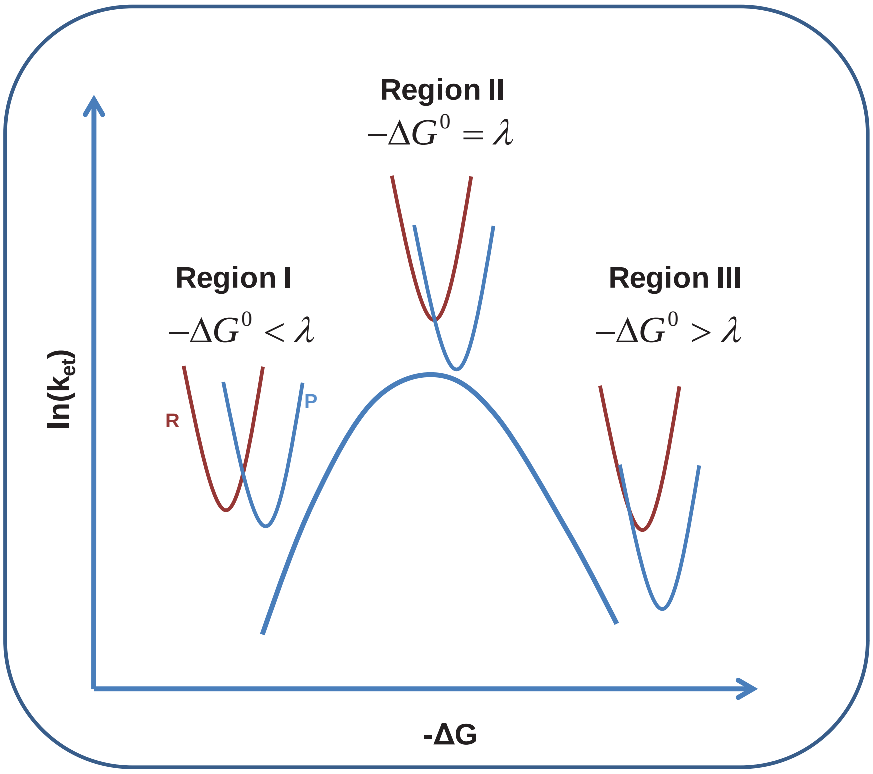
Region II
$-\Delta G^0 = \lambda$
Region I
$-\Delta G^0 < \lambda$
Region III
$-\Delta G^0 > \lambda$
R
P
ln(k$_{et}$)
-ΔG

Figure 1.14. Schematic of ln(k$_{et}$) vs ΔG^0.with different regions. Region I, Region II and Region III are called Normal region, barrierless region and inverted region respectively

Activation free energy is given by the above equation. Using the free energy we can write rate of electron transfer in Arrhenius form

$$k_{et} = A \times \exp\left(\frac{-\Delta G^*}{k_b T}\right) \tag{1.32}$$

Preexponential factor A is determined by type of electron transfer involved.

Vibrational contribution can be written by taking into consideration change in configuration between reactant and product.

Most counterintuitive prediction of Marcus theory is existence of inverted region where while ΔG^0 is highly negative or reaction exoergic. The rate of reaction decreases due to increase in reorganization energy as shown in fig. 1.14.

1.6.3. Quantum mechanical theory of electron transfer

In the previous treatment of the electron transfer problem it was assumed that transmission coefficient is 1, i.e all reactant reaching the transition state gives rise to product. However, according to quantum theory this is seldom true as there is a finite overlap between donor and acceptor. Additionally, transmission coefficient must be treated explicitly to include effects of electron tunneling. The electron tunneling probability depends on electronic coupling between the donor and acceptor. In cases where H_{RP} is large, the reaction proceeds through lower PES (see fig.1. 12) or reaction is called adiabatic. If H_{RP} is small reaction is nonadiabatic as mentioned in section 1. 6. 1. Non adiabatic cases can be treated well within the framework of semiclassical Marcus theory. However for an adiabatic reaction the interaction strength, H_{RP} plays a significant role in electron transfer dynamics. In the inverted region involvement of higher vibrational modes towards electron transfer cannot be neglected. In such cases considered one high frequency mode, electron transfer rate can be written as,

$$k_{et} = \frac{4\pi^2}{h} \frac{1}{\sqrt{4\lambda_s k_b T}} \left(H_{RP}\right)^2 \sum_{n=0}^{\infty} \langle 0 | n \rangle^2 \exp\left(\frac{-(\Delta G^0 - nh\nu + \lambda)^2}{4\lambda_s k_b T} \right) \qquad (1.34)$$

In the above expression reactant is in ground vibrational state “0” and product is in higher vibrational state of index n.

$$\langle 0 | n \rangle^2 = \left(\frac{s^n}{n!} \right) \exp(-s) \text{ and } s = \frac{\lambda_i}{h\nu} \tag{1.35}$$

If we include all vibrations then we get,

$$k_{et} = \frac{4\pi^2}{h} \left(H_{RP} \right)^2 (FC) \tag{1.36}$$

FC is the Franck-Condon Factor which is sum of all contributions solvation and vibration.

1. 7. Interfacial Electron Transfer from Molecular Adsorbate to Semiconductor

ET in a semiconductor-dye system is a heterogeneous process. In this case electron transfer involves coupling between multitudes of semiconductor band levels with frontier orbitals of the dye molecules with a change in phase at the interfaces. In some of the cases investigate in the thesis we investigate electron transfer in such systems.

The theoretical framework for such processes was independently developed by Marcus [1.45], Gerischer [1.46], and Levich and Dogonadze [1.47]. In unconfined systems or so called bulk semiconductors delocalized band states and trap states contribute towards ET process. While all the states need to be considered in building an ET theory, description of trap states are more complicated due to it energetic heterogeneity etc. The ET process described in the paper mostly involves ET from molecular adsorbate to semiconductor CB and BET.

1. 7. 1. Electron Injection

ET in dye-semiconductor system involves reactant state mostly localized on dye LUMO and product state consisting of electron in CB of the semiconductor. While reactant state in dye molecule are mostly consists of only one orbital while the product states are a continuum in a semiconductor. Therefore Franck-Condon overlap with weighted DOS should be considered for electron transfer rates. In the case of an adiabatic coupling, the problem is nontrivial due to involvement of several strongly interacting potential energy surfaces (PES). In nonadiabatic case, Marcus et al [1.45] showed ET rates as given below

$$k_{ET} = \left(\frac{4\pi^2}{h}\right)\frac{1}{\sqrt{4\pi\lambda k_B T}}\int dE\rho(E)(1 - f(E, E_F))\left|\bar{H}(E)\right|^2 \exp\left[-\frac{(\lambda + \Delta G^0 + E)^2}{4\pi\lambda k_B T}\right] \quad (1.37)$$

In the above equation, free energy (ΔG^0) is given as = $E_{CB} - E_{ox}$ (E_{CB} = energetic position of conduction band and E_{ox} = oxidation potential of adsorbate LUMO; $\rho(E)$ is the DOS at energy E. $\rho(E)$ has contribution from CB and surface states. $\bar{H}(E)$ is the strength of electronic coupling between adsorbate LUMO and states in the semiconductor at the same energy E; and λ the total reorganization energy. The Fermi occupancy factor $f(E - E_F)$ is introduced to include only unoccupied states. It is generally neglected due to assumption that at room temperature electron population is negligible at room temperature in a wide band gap semiconductor.

In real systems the electronic interaction between semiconductor and adsorbate is inhomogeneous leading to a distribution of electronic coupling, H, which in turns leads to a distribution of injection rates. Therefore population of injected electron, $N_e(t)$, can be written as,

$$N_e(t) = N_0 \left[1 - \int_0^\infty g(H) e^{-K_{ET}(H)t} dH \right] \tag{1.38}$$

In the above equation N_0 is the total number of excited molecules. Assuming injection is the only deexcitation mechanism and acceptor states on CB then DOS is given by

$$\rho(E)dE = \frac{(2m^*)^{3/2}}{2\pi^2\hbar^3}\sqrt{E}dE \tag{1.39}$$

In the above equation m^* is the effective mass of electrons in the conduction band.

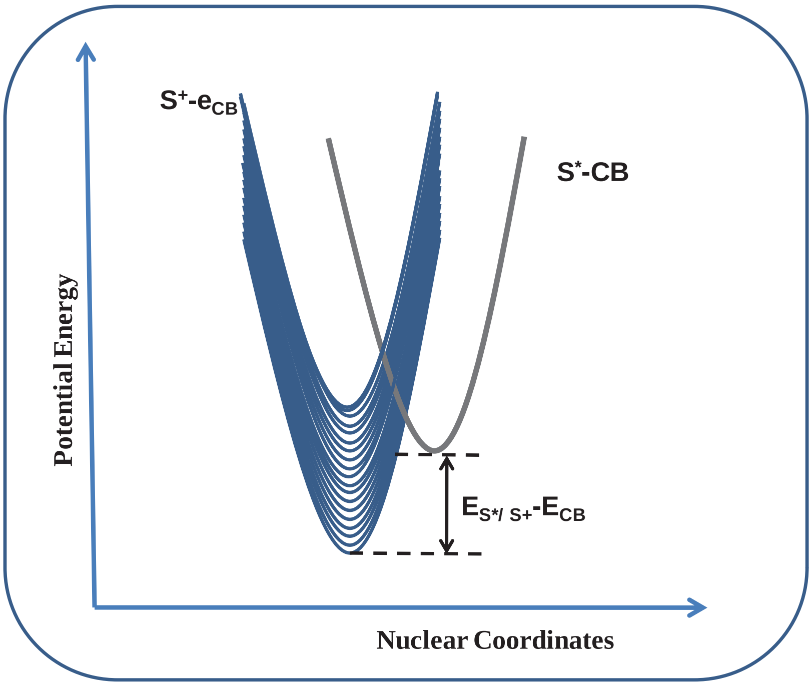

Fig. 1. 15. Schematic of ET from a reactant state to a continuum of product states.

Under assumption of invariance of electronic coupling with energy we can conclude that electron injection rates will increase for states higher in energy in CB or $E_{ox}(S^*)$–Ecb due to higher DOS. Additionally we can also conclude that low ET rates for small driving force due to larger reorganization energy. In more complicated schemes coupling of different dye vibrational levels with CB levels is also considered.

Under conditions of strong coupling or adiabatic limit, nuclear motion in the system or the electronic dephasing times in the solid governs electron transfer rates. In such cases ET is barrier less and independent of energy of the injecting state and proceed in time scale of < 100fs. In adiabatic case electron injection effectively competes with energy relaxation and in many cases a 100% injection yield is expected.

1.7. 2 Back Electron Transfer

BET refers to electron transfer from semiconductor nanoparticle to the oxidized molecular adsorbate, reactant in this case is electron in semiconductor and product state is electron in ground state of the dye. In this case the electron can be in a trap or CB minima, therefore electronic energetics and free energies varies. Furthermore in most of these cases there is reactant state districution. Therefore ET rates are the averages of these factors. Additionally electron diffusion between different trap sites also needs to be considered.

However in simple case where electron diffusion between trap sites is much slower than BET, BET kinetics can be given as:

$$N_e(t) = N_0 \int_0^{r_0} drP(r) \exp\left[-\int_0^t k(r,t)dt \right] \tag{1.40}$$

In the above equation $P(r)$ is the spatial distribution of trapped electrons and r_0 is the adsorbate distance from semiconductor surface. $k(r,t)$ is the ET rate for trapped electrons at that distance. It is clear from the equation that ET rates are highly non-exponential.

According to Marcus theory as described earlier, in normal region $\left|\Delta G^0\right| > \lambda$ therefore BET rate constant increases with increasing driving force. For $\left|\Delta G^0\right| < \lambda$ or inverted regime BET rate constant decreases with increasing driving force. The existence of inverted region has been verified in several systems.

1. 8. Synthesis of Semiconductor Quantum Dots

Synthesis methodology of semiconductors may be classified into basically two methods (i) Top down approach and (ii) Bottom Up approach. In the top down approach we start with a bulk nanocrstal and reduced the size and create nanoparticles. Familiar top down approaches are focused ion beam etching and ball milling [1.48, 1.49]. In bottom up approach we start with precursor molecules and coax them by synthesis control to form crystals. All chemical synthesis based approach falls under this category for e.g. colloidal methods, sol gel approach, MOCVD, MBE, ALD etc [1.50]. In this approach we can have significant reproducibility for given reaction conditions. In our synthesis for all of present study we use colloidal methods for synthesis of quantum dots. To study charge carrier dynamics for different sizes it can be clearly seen that we need a sharp distribution of size. Therefore a proper size control is of utmost imperative for studying size dependent properties. It is known previously that in colloidal synthesis, precipitation or nucleation and growth can happen at the same time. Therefore under this condition it is difficult to achieve good size distribution. To achieve good size distribution it is essential to separate nucleation and growth [1.51]. This is achieved by using optimal concentration of precursors and capping agents during synthesis. Function of capping agent is multi fold (i) It binds to the surface strongly therefore controls growth, (ii) It enables dissolution of nanoparticle in a solvent (iii) Very often it caps the surface electronically thereby eliminating trap states on the surface of nanoparticle. One of the most familiar approaches to colloidal synthesis of quantum dots is arrested precipitation technique. In this technique one of the precursors in solution is maintained at high temperature and the other precursor is injected rapidly into the solution leading to formation of nuclei and subsequent growth takes place over these nuclei forming monodisperse nanoparticles at a lower temperature to reduce further nucleation. To understand how nucleation and growth is separated it is necessary to recognize different phases of reaction. Let us take the case of CdSe where cadmium precursor used is CdO dissolved in Oleic acid and selenium precursor is freshly prepared TOPSe at reaction temperature of 300˚C. TOPSe is added to cadmium precursor maintained at 300˚C swiftly leading to very high super-saturation. This leads to formation of nuclei instantly also called burst nucleation. Formation of nuclei is a high barrier process however due to high super-saturation and temperature, nucleation commences. On addition of TOPSe temperature decreases by ~20-30˚C and additionally precursor concentration also decreases due to formation of nuclei leading to lower probability of formation of further nuclei. Once nucleation is achieved, growth commences. Therefore this method offers a way to separate nucleation and growth thereby enabling formation of monodisperse nanoparticles. The growth stage is not simple as growth of different size particles takes place at different rates. The precursor concentration versus time is depicted in figure 1.16 below.

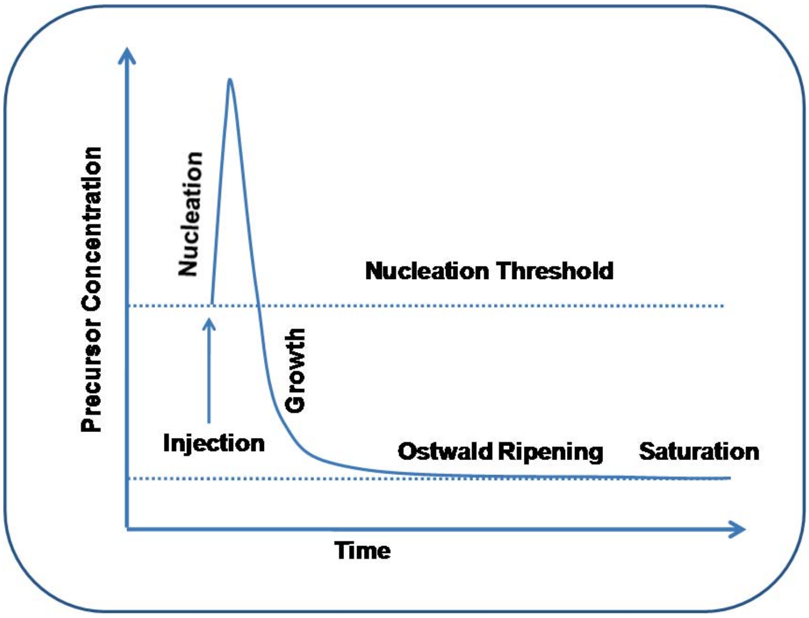

Figure 1. 16. Nucleation and growth stages for preparation of monodisperse nanoparticles in La Mer Growth model.

The schematic in figure 1.16 represent growth of monodisperse nanoparticles in LaMer model which shows a distinct temporal separation between nucleation and growth. This model also tells us why nucleation is separated from growth. As soon as precursors are added a burst nucleation which takes place till the concentration is above nucleation threshold below nucleation threshold, no new nuclei are formed and remaining precursors leads to growth. Therefore synthetic conditions can be achieved where the nucleation threshold is tuned to optimize monodipersity of nanoparticles. Within this model monodispersity is achieved when consumption of precursor does not exceed precursor addition rate. Moreover it can be seen from the schematic that if during nucleation, growth is much less then one can achieve a good size distribution. While nucleation is one of the factors governing monodispersity in initial times, growth stage also can lead to loss of initially achieved monodispersity. The growth stage can be divided into (i) Fast growth stage and (ii) Slow growth stage. In the fast stage growth of nanoparticles takes place mainly from remaining precursors in the solution. In this growth stage size focusing happens as smaller nanoparticle grows faster than larger nanoparticles due to higher surface energy. However in slow growth stage also called Ostwald ripening, smaller nanoparticles dissolve and this forms further precursor for growth of larger nanoparticles. In this stage size defocusing takes place.

Therefore different sizes of nanoparticles with good size distribution (10-15%) can be achieved by this method. Additional narrow size distribution can be achieved during processing stage. To clean nanoparticles by removing precursors can be achieved by addition of non solvent. For oleic acid capped nanoparticles, methanol, ethanol, acetone etc are good non solvent. This is achieved by controlled addition of nonsolvent into reaction solution. In the initial stages largest nanoparticles precipitate. These precipitates can be removed by centrifugation and the procedure can be repeated to get finely focused size distribution. In the present study we employ a water based approach for synthesis of quantum dot based nanostructures as this synthesis method does not require harsh conditions or organometallic precursors for synthesis.

1.9 Thesis Overview

In present thesis, we interrogate dynamics in QDs, QDs based nanostructures, and QD-Dye systems by ultrafast transient absorption technique. The intended aim is to throw more light on dynamics in these nanostructures. We especially look for cooling and recombination dynamics and the contribution from both the charge carriers towards these processes. We study how the carrier dynamics is dictated by size in CdTe quantum dots.

Additionally we also look for how BET process is influenced size in weak quantization limit in TiO_2 nanostructures. Also we investigate novel QD nanostructures to improve upon the behavior of charge carriers. Since we look to increase charge recombination times which are especially suited for a photovoltaic applications, we construct core shell and metal semiconductor nanocomposites. In core shell system we use staggered band aligned system like CdSe/ZnTe. We analyze how dynamics is influence by thickness of shells. In metal QD nanostructures we construct CdTe decorated reduced graphene nanostructure.

All the samples were synthesized in our laboratory and characterized using XRD, TEM, Raman spectroscopy, UV-Vis absorption and PL spectroscopy. The dynamics of electrons and holes were deciphered using suitable quenchers. The studies point to immense potential of QDs and QD based nanostructures in photovoltaics.

1.10. Scope of the Thesis in View of Applications in Photovoltaics

The thesis is aimed to understand charge carrier dynamics broadly speaking studies of which will be immensely useful in photovoltaics. However large part of the thesis consists also of synthesis of these QDs as tailor made novel nanostructures are investigated vis a vis their potential in photovoltaics. The first study employs ultrasmall TiO_2-Alizarin system where TiO_2 is in weak confinement regime. The dynamics was monitored for cation absorption and free electron absorption in TiO_2 after photoexcitation of dye. Therefore essentially we are monitoring an interfacial electron transfer phenomena, which is one of the prominent process occurring in a DSSC. CdTe QDs were synthesized and their size dependent dynamics also were studied to throw more light on factors governing dynamics. CdSe/ ZnTe core shell with varying shell size were interrogated to investigate carrier cooling and rate of charge transfer across the interface from core to shell. In addition to semiconductor nanostructures we have also investigated metal-seconductor nanocomposite (CdTe decorated Graphene) for their charge separation behavior.

1.11. References

1.1 Feynman, R.P., "There's plenty of room at the bottom (data storage)". Journal of Microelectromechanical Systems, 1992, 1, 60 (Reprint).

1.2 Walter Graetzer, Giant Molecules, 2009, Oxford University Press.

1.3 D. Maclurcan and N. Radywyl, Nanotechnology and Global Sustainability, 2011, CRC Press.

1.4 A. I. Ekimov & A. A. Onushchenko, JETP Lett., 1981, 34, 345.

1.5 R. Rossetti, S. Nakahara, L. E. Brus, J. Chem. Phys., 1983,79, 1086.

1.6 L. E. Brus, J. Chem. Phys., 1983, 79, 5566.

1.7 A. L. Efros, and A.L. Efros, Soviet Physics Semiconductors-USSR, 1982, 16, 772.

1.8 A. J. Nozik, Physica E: Low-dimensional Systems and Nanostructures, 2002, 14, 115.

1.9 X. Michalet, F. F. Pinaud, L. A. Bentolila, J. M. Tsay, S. Doose, J. J. Li, G. Sundaresan, A. M. Wu, S. S. Gambhir,S. Weiss, Science, 2005, 307, 538.

1.10 E. H. Sargent, Adv. Mater., 2005, 17, 515.

1.11 Daniel Loss and David P. DiVincenzo, Phys. Rev. A, 1998, 57, 120.

1.12 A. J. Nozik, Annu. Rev. Phys. Chem., 2001, 52, 193.

1.13 V. I. Klimov, J. Phys. Chem. B, 2000, 104, 6112.

1.14 P. Harrison, Quantum Wells, Wires and Dots, 3rd Edition, Wiley.

1.15 A. S. Davydov, Quantum mechanics, 1987,ed. Akadamieverlag. Berlin.

1.16 Al. L. Efros and M. Rosen, Annu. Rev. Phys. Chem., 2000, 30, 475.

1.17 J. M. Luttinger, Phys. Rev., 1956. 102, 1030.

1.18 J. M. Luttinger, and W. Kohn, Phys. Rev., 1955, 97, 869.

1.19 S. Prabhu, A. Vengurlekar, J. Shah, Phys. Rev. B, 1995, 51, 14233.

1.20 V. Klimov, H. P. Bolivar, H. Kurz, Phys. Rev. B, 1995, 52, 4728.

1.21 T. Inoshita and H. Sakaki, Phys. Rev. B, 1992, 46, 7260.

1.22 E. Hendry, M. Koeberg, F. Wang, H. Zhang, C. de Mello Donegá, D. Vanmaekelbergh, and M. Bonn, Phys. Rev. Lett., 2006, 96, 057408.

1.23 V. I. Klimov and D. W. McBranch, C. A. Leatherdale and M. G. Bawendi, Phys. Rev. B 1999, 60, 13740.

1.24 H. Htoon, J. A. Hollingsworth, R. Dickerson, and V. I. Klimov, Phys. Rev. Lett., 2003, 91, 227401.

1.25 R. J. Ellingson, M. C. Beard, J. C. Johnson, P. Yu, O. I. Micic, A. J. Nozik, A. Shabaev, and A. L. Efros, Nano Lett., 2005, 5, 865.

1.26 G. Allan and C. Delerue, Phys. Rev. B 2006, 73, 205423.

1.27 A. Franceschetti, J. M. An, and A. Zunger, Nano Lett., 2006, 6, 2191.

1.28 E. Becquerel. C. R. Acad. Sci 1839, 9, 561.

1.29 H. Gerischer, H. R. Schoppel, B. Pettinge, J Electrochem Soc 1972, 119, C230.

1.30 R. Memming, F. Schroppel, Chem Phys Lett, 1979, 62, 207.

1.31 B. O’Regan, M. Grätzel, Nature, 1991, 335, 737.

1.32 P. V. Kamat, J. Phys. Chem. C, 2008, 112, 18737.

1.33 A. J. Nozik, Physica E, Low-Dimensional Systems and Nanostructures, 2002, 14, 115.

1.34 V. Aroutiounian, S. Petrosyan, and A. Khachatryan, K. Touryan, J. App. Phys., 2001, 89, 2268.

1.35 B. O. Dabbousi, J. Rodriguez-Viejo, F. V. Mikulec, J. R. Heine, H. Mattoussi, R. Ober, K. F. Jensen, M. G. Bawendi, J. Phys. Chem. B, 1997, 101, 9463.

1.36 S. Kim, B. Fisher, H.-J. Eisler, and M. Bawendi, J. Am. Chem. Soc., 2003, 125, 11466.

1.37 Y. Yang, W. R. -Córdoba,T. Lian, J. Am. Chem. Soc., 2011, 133, 9246.

1.38 J. Huang, Z. Huang, Y. Yang, H. Zhu and T. Lian, J. Am. Chem. Soc., 2010, 132, 4858.

1.39 M. Jakob, H. Levanon, P. V. Kamat, Nano lett., 2003, 3, 353.

1.40 Wood, A.; Giersig, M.; Mulvaney, P. J. Phys. Chem. B, 2001, 105, 8810.

1.41 I. Gur, N A. Fromer, M. L. Geier and A. P. Alivisatos, Science, 2005, 310, 462.

1.42 S. A. McDonald, G. Konstantatos, S. Zhang, P. W. Cyr, E. J. D. Klem, L. Levina and E. H. Sargent, Nat. Mater., 2005, 4, 138.

1.43 C. C. Moser, J. M. Keske, K. Warncke, R. S. Farid, P. L. Dutton, Nature 1992, 355, 796.

1.44 R. Memming, Semiconductor Electrochemistry, 2001, ed. Wiley-VCH. Weinheim.

1.45 R. A. Marcus, Ann. Rev. Phys. Chem., 1964, 15, 155.

1.46 H. Gerischer, Z. Phys. Chem. NF, 1960, 26,223, 325.

1.47 Levich, Dogonadze, Dokl. Acad. Nauk. SSSR, 1959, 124, 123.

1.48 C Lam, Y.F Zhang, Y.H Tang, C.S Lee, I Bello, S.T Lee, Journal of Crystal Growth, 2000, 220, 466.

1.49 M. G. Ancona, S. E. Kooi, W. Kruppa, A. W. Snow, E. E. Foos, L. J. Whitman, D. Park, L. Shirey, Nano Letters, 2003, 3, 135.

1.50 Clemens Burda, Xiaobo Chen, Radha Narayanan, Mostafa A. El-Sayed, *Chem. Rev.*, 2005, 105, 1025.

1.51 C.B. Murray, C. R. Kagan, M.G. Bawendi, , Annu. Rev. Mater. Sci., 2000, 30, 545.

Chapter 2

Chapter 2

Experimental

2.1. Introduction

The present thesis work is aimed at understanding carrier dynamics in QD based nanostructures. Some of QD nanostructures presented are novel and require synthesis in our laboratory. Therefore characterization of these nanostructures is of paramount importance before carrying out carrier dynamics studies. We have used a variety of structural and optical characterization techniques to characterize these materials. Structural characterization techniques performed includes electron microscopy, electron diffraction, X-Ray diffraction, and Raman spectroscopy. Optical characterization was carried out by steady state UV-Vis absorption and photoluminescence (PL) studies. Carrier dynamics was mainly studied by time correlated single photon counting (TCSPC) and broadband ultrafast pump-probe transient absorption spectroscopy. The instrumental layouts of the instruments used and basic principles of these characterization techniques are described in this chapter.

2.2. UV-Visible Absorption Spectroscopy

Atoms and molecules have discrete electronic levels and transition from ground to different excited states can be affected by light. Since electronic levels in a particular chemical species are unique, these can be used as fingerprint for identification of molecules. The absorption of light in ultraviolet-visible (UV-Vis) region can be used to characterize chemical species. Since a particular peak height is proportional to concentration of the species, one can use the technique for both quantitative and qualitative evaluation of a chemical species [2.1-2.3]. UV-Vis absorption spectra were collected using Biomate model UV-visible spectrophotometer with a range of 200-1100nm and resolution of 1nm.

As mentioned earlier the technique exploits the excitation of a chemical species using light. Obviously a particular molecule absorbs in a range of wavelength around absorption maxima. Not only intrinsic but also extrinsic factors govern peak position and broadening for e.g. solvent properties.

The system consists of a calibrated source where incident light of a particular wavelength is known. Now if a chemical species absorbs around λ_{max}, then intensity of transmitted light at that wavelength decreases. Decrease in intensity of transmitted light is a function of concentration and path length (length of passage through the sample).Below given equation gives relationship between the absorbance and different factors

$$A = \log_{10}\left(\frac{I_0}{I}\right) = \varepsilon c l \qquad (2.1)$$

In above equation A is the absorbance, I_0 is incident intensity I is transmitted intensity for a particular wavelength and l is path length, ε is molar absorptivity constant and c is concentration of that species. We assume that decrease in intensity arises from absorption of light by sample and not scattering. Scattering is especially large in cases where solubility of sample is poor. Additionally concentration of samples are expected to be kept low as at higher concentration factors like intermolecular interactions and changes in refractive index affect measurement. The scan over entire UV-Vis region gives rise to absorption spectra which forms the basis of this technique.

2.3. Fluorescence Spectroscopy

Fluorescence spectroscopy is a commonly used technique in characterizing different samples. This technique exploits the emission from a species on optical excitation. The emission peak position, width contains valuable information on the sample [2.4, 2.5]. For the present thesis we have used a Hitachi fluorimeter F-4010 model which employed 150W high pressure xenon lamp as excitation source, different monochromators for excitation and emission wavelengths and photomultiplier tube (PMT) as detector. For spectral range 280-650nm, IP-28 (Hamamatsu) and for range 400-800nm, R-928F (Hamamatsu) PMT was used.

In fluorescence spectroscopy, molecule of interest is excited into a higher electronic level with a particular wavelength of light and radiative relaxation of the molecule is recorded in a wavelength range. The emission generally occurs from a vibrationally relaxed configuration of excited electronic state, therefore is generally red shifted with respect to absorption spectra of that particular transition. The shift between absorption and emission maxima is referred to as Stoke shift. Stoke shift can be due to vibrational relaxation, intramolecular charge transfer etc. In the case of semiconductors radiative relaxation can take place from band edge also called band edge emission or it takes place from a trap which is called a trap state emission. Generally trap state emission band is broad due to energetic heterogeneity arising and distribution of bonding configurations. Apart from fluorescence one can also monitor what is called excitation spectra. In excitation spectra, emission wavelength is held constant and excitation wavelength (till position of emission wavelength) is varied. This gives rise to a plot of emission intensity versus excitation wavelength.

One of the most important applications of fluorescence spectroscopy is in biolabeling, therefore a high quantum yield is a desirable trait for such applications. Therefore fluorescence forms an important monitoring technique. Other parameters of immense interest are Quantum yield, which is defined as given below.

$$Quantum\ yield\,(Q.Y) = \left(\frac{N_{Em}}{N_{Ab}}\right) \qquad (2.2)$$

N_{Em} =Number of photons emitted, N_{Ab} =Number of photons absorbed

Simpler way to arrive at quantum yield with respect to a known reference with emission position closer to the samples.

$$Q.Y_{Sample} = Q.Y_{\mathrm{Re}\,ference}\left(\frac{F_{Sample}}{F_{\mathrm{Re}\,ference}}\right)\left(\frac{A_{\mathrm{Re}\,ference}}{A_{Sample}}\right)\left(\frac{n_{Sample}}{n_{\mathrm{Re}\,ference}}\right)^{2} \qquad (2.3)$$

A is the value of integrated absorbance, F is integrated fluorescence and n is the refractive index of solution in the above equation. Generally for quantum yield measurement A of sample is maintained below 0.1.

2.4. X-Ray Diffraction

2.4. 1. Introduction

The synthesized QDs are crystalline phases, their size and crystal phase have a significant impact on charge carrier dynamics. Overall information regarding crystallinity is obtained by X-Ray diffraction technique [2.6, 2.7]. It helps in identifying both crystallinity and different polymorphs if any, for a particular synthesized QDs. Powder XRD is a versatile technique which does not require any samples preparation to collect the diffraction patterns. In a powdered sample i.e. powder XRD, a random orientation of crystal phases exists (especially for spherical crystallites). The diffraction from a sample with random orientation of crystal planes appear at different angles, this forms the basis for identification of different phases. The angle of diffraction is clearly indicative of distances between the planes. The relationship between lattice plane spacing and angle of diffraction is given by Bragg's law.

$$n\lambda = 2d\sin\vartheta \qquad (2.4)$$

In equation 2.4 n is the order of diffraction; ϑ is diffraction angle; d is the lattice spacing. Another important factor which helps in indexing an XRD pattern is the intensity of diffraction. The intensity is also a function of atomic scattering factors and miller indices of the planes. The atomic scattering factors influences intensity as the scattering centers in atoms are electrons. Therefore higher the number of electrons, greater is scattering from that particular atom. Phase characterization can be done just by comparing the diffraction pattern obtained for samples with that of previously reported patterns as given by database from by Joint Committee on Powder Diffraction Standards (JCPDS), International Centre for Diffraction Data (ICDD).

Apart from phase characterization one can obtain information on particle size assuming the particles are spherical. For a bulk crystallite or a large crystal, scattering signal is sharp, however in nanocrystallites the peaks are broadened due to coherence lengths of X-ray. Therefore the broadening is related to size of the diffracting domain therefore of crystallite size.

$$D = \frac{k\lambda}{\Delta 2\vartheta\cos\vartheta} \qquad (2.5)$$

In the equation above, k is the shape factor and is generally close to 1; D is the crystallite size. The broadening of an x-ray peak is actually a combination of instrumental broadenings arising from incident x-ray peak breadth and detectors etc. Instrumental factors are eliminated by use of standard which is generally a single crystal and has peak near that particular 2ϑ value. The broadening is calculated as given below.

$$\beta^2 = \beta_D^2 + \beta_I^2 \qquad (2.6)$$

Here β_D arises from domain size and β_L arises from instrumental factors. As mentioned earlier this is a crude method for estimating size as broadening can also arise from stress in the sample. Therefore β_D is also a function of stress and samples are assumed to be spherical.

2.4. 2. Instrumentation

Figure 2.1 shows a schematic of XRD instrument. The first step is creation X-Rays which is accomplished by bombarding high energy electrons on a metal target. By this process, apart from broad distribution of X-rays created due to deceleration on electrons also called Bremsstrahlen, sharp lines are also created which are superimposed on the broad distribution. These sharp lines arise from characteristic X-ray coming from knocking down of core electrons creating a “hole” and subsequent filling of higher electrons. Performing a diffraction experiment requires intense sharp X-ray as the diffraction angle is also dependent on x-ray energies; therefore a broad distribution is ineffective for performing diffraction. The mainly used targets in a set up are metals like copper, molybdenum, chromium etc. The filtering of broad distribution is accomplished by using a filter which has a 1 unit atomic number less than the target material. The resultant beam is further monochromatised by using a single crystal monochromator. In a PXRD, the samples in powdered form are spread over an amorphous substrate (generally glass slides) in presence of a binder like colloidion in amyl alcohol. The detectors are generally scintillation counters. The detector is scanned over different angles and intensities are plotted with respect to angles. The peak position observed are angle where Bragg condition is satisfied.

In the present thesis, we have used a Philips X-ray machine, model-PW 1710 with Ni filtered Cu Kα radiation (λ=1.5406Å), using silicon as an external standard. The measurements are performed in a range of 10˚-80˚ in a continuous scan mode, with a step width of 0.02˚, and scan of 1˚ per minute. The measurement of ϑ corresponding to each peak position and peak intensity is important for identification of materials. The measured data is compared with database of standards samples with the help of JCPDS-ICDD (Joint Committee on Powder Diffraction Standards-International Centre for Diffraction Data) [2.8].

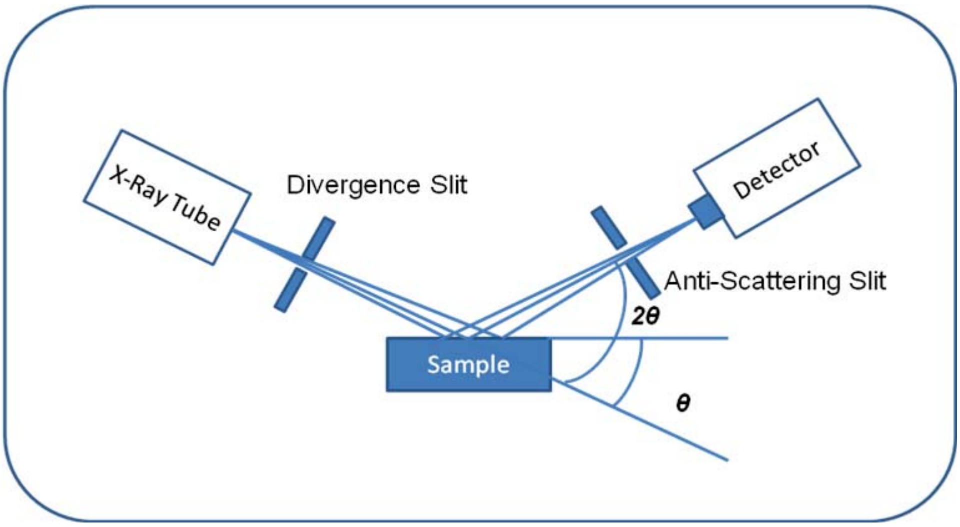

Figure. 2. 1. Schematic of a typical XRD instrument

2.5. Raman Spectroscopy

Raman spectroscopy is a technique complementary to infrared spectroscopy. Raman spectroscopy is used to study mainly vibrational modes in a system [2.9]. Since vibrational peaks positions are fingerprints of a molecular species it can help in characterization of a sample. Raman spectroscopy is based on inelastic scattering of light. On excitation of a sample, the electrons are pushed to a virtual level and from the virtual levels electrons returns to ground state (Rayleigh scattering) or return to higher vibrational state (Stokes line). Additionally the sample may be excited from higher vibrational state to virtual state and returns to ground vibrational state also called anti stokes line. Anti stokes light has a greater energy than the incident light.

$$\Delta \bar{\nu} = \left(\frac{1}{\lambda_0} - \frac{1}{\lambda_s} \right) \tag{2.7}$$

λ_s and λ_0 is wavelength of scattered and incident (excitation) light in the above equation.

The Stokes line is more intense compared to Antistokes line as at room temperature ground vibrational state is most populated state of a molecule. Visible wavelengths are used in Raman spectroscopy, as scattering of visible light is more efficient compared to IR due to inverse scaling of scattering cross section with wavelength. Very often a tunable excitation source is used to achieve a resonance in scattering when incident light is close to excited molecular level. Such a process is called resonance Raman scattering. In case of resonance Raman scattering, cross section for scattering increases by ~10^4. Scattered light is collected at either in 90˚ or 180˚ with respect to excitation light. CCD detectors are used for detection in most of current spectrometers. In present thesis we have used a LABRAM1, ISA make spectrometer in the back scattering geometry with 488 or 514 nm line of Ar ion laser.

2.6. Transmission Electron Microscopy (TEM)

2.6. 1. Introduction

Most characterization techniques discussed previously are optical characterization. In typical synthesis of nanomaterials, a distribution of particles sizes or presence of multiple phases or amorphous phases are present. Before carrying out the carrier dynamics it is necessary to obtain this information as all of the above factors mentioned earlier can influence charge carrier dynamics. One of the versatile techniques that give all this information is a transmission electron microscope. Since the features that are to be studied are in nanometer size regime, imaging is only possible if wavelength of probe used is close to the size of the features that is to be imaged. In a TEM, electrons are used as probes since their wavelength can be tuned according to energy [2.10, 2.11]. In modern TEMs accelerating voltage of ~100-1500keV are used. The wavelength of electrons for these voltages is in Pico meters; therefore TEM can in principle image lattice planes. However due to aberrations involved, the resolution of a TEM instrument is limited. However state of the art TEM machines have overcome these problems in aberration corrected TEM. Additionally one can perform electron diffraction and obtain crystallinity and crystal structure. Additional information can also be obtained from inelastic scattering of electrons. These inelastic scattering events can arise from a number of processes like phonon scattering, plasmon scattering, ionization etc. These energies can be used for chemical characterization of the sample. In a TEM, there are two common modes of imaging: bright field and dark field imaging. Bright field image is collected by monitoring un-scattered electrons after passing through the sample and objective aperture. Therefore regions where sample is not present will appear bright and region with samples will appear black due to scattering of electrons leading to reduced intensity. Image produced with scattered electrons (after interaction with the sample) gives rise to a dark field image. The contrast produced in a dark field is much higher; however the intensities are lower. Therefore dark field imaging requires larger exposure times. The dark field imaging is carried out by moving objective aperture to monitor un-scattered beam. However this is of poor quality as we intercept electrons in region where aberrations are dominant. In crystalline samples the diffraction spots or rings are monitored therefore specific planes are monitored.

2.6. 2. Layout of TEM

The schematic of a typical TEM is given in the figure 2.2. It consists of an electron source based on thermionic emission for e.g. tungsten wire. One of an important requirement to get a sharp image is presence of good temporal and spatial coherence of electrons. Tungsten guns suffer from the problem of energy spread of emitted electrons and brightness. These properties contribute to limitation in terms of temporal and spatial coherence. Therefore in recent times field emission guns have replaced thermionic emission guns which have better coherence properties. Field emission guns have a small probe size. However cost of field emission guns is very high as compared to thermionic emission guns. Therefore thermionic electron guns are still in use in most TEMs around the world. To reduce the problem arising due to heating the filament to high temperature, low work function materials like LaB_6 is used. However this type of material requires much higher vacuum due to poisoning of LaB_6 in presence of oxygen. Apart from coherences, brightness of the source is also another factor determining the choice of electron guns.

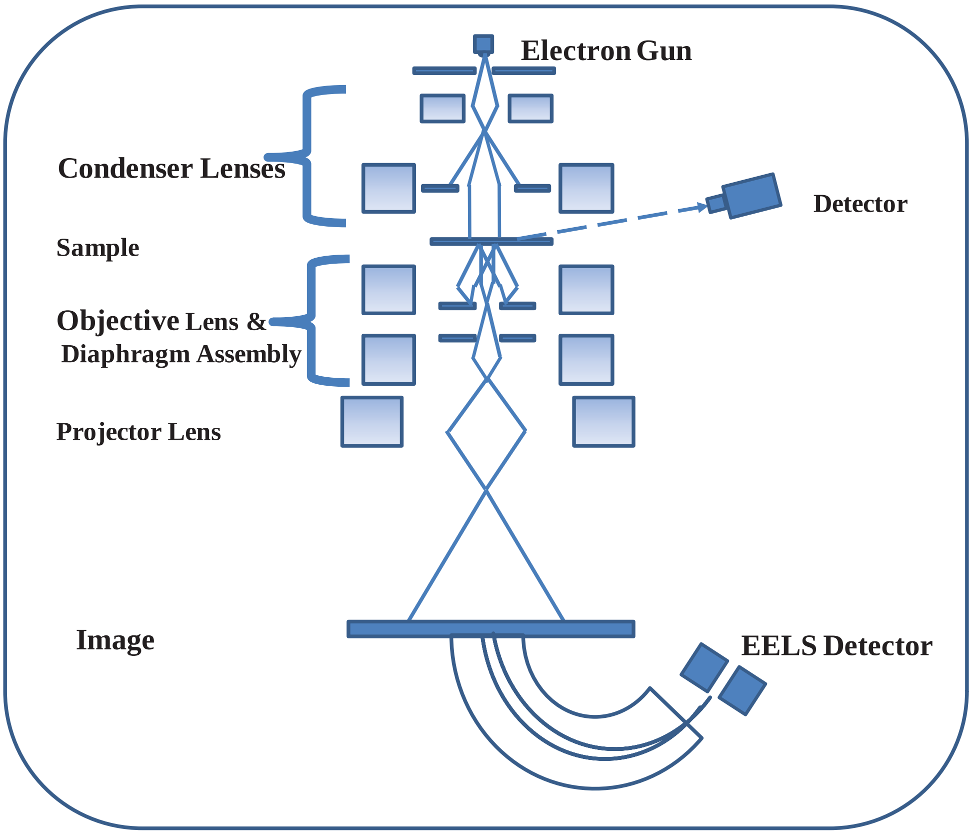
Electron Gun
Condenser Lenses
Detector
Sample
Objective Lens &
Diaphragm Assembly
Projector Lens
Image
EELS Detector

Figure. 2.2. Schematic of a TEM instrument

The condenser lens functions as sample illuminator. Electron probe over the sample can be as small as few nm in high magnification and can also uniformly illuminate entire sample for lower magnification. Recent scanning TEMs have electron probes lesser than nm. In order to achieve this, combination of condenser lens system is used. The system also consists of what is called as condenser stigmator which corrects astigmatism arising from the condenser lenses. In TEM, stigmator is always invariably adjusted during column alignment.

The specimen stage generally circular in shape, consists of a holder for the specimen where the samples are "illuminated" by electrons. The grids are placed on specimen state for imaging. In present study, carbon coated copper grid are used. The sample dispersed in a volatile solvent is drop casted and allowed to dry. The samples are expected to be thin enough to allow the electrons to pass through for image formation. The main imaging system in a TEM instrument is the objective lens system. This lens is highly converging with a very small focal length. The objective lens produces an enlarged image on a screen placed several cm below the lens. Due to small focal length of the lens the image produced at a large distance is highly magnified. Apart from producing magnified image the objective lens reduces aberrations by rejecting electrons scattered at large angles. The most common aberrations involved in lenses are chromatic and spherical aberration. Since these aberrations limits the resolution of lenses it is necessary to understand these aberrations to reduce it. Spherical aberration is a defect arising from the lenses. In this case the off axis electrons are focused at different points other than the focal plane. Aberration produces a disc instead of a sharp image therefore limiting the resolution. Spherical aberration present in these lenses are given by,

$$r_s = C_s \alpha^3 \tag{2.8}$$

In the equation above r_s is radius of disc; C_s is the coefficient of spherical aberration, and α is angle of electron beam with respect to axis. This type of aberration arises from the electron lenses therefore cannot be eliminated completely. However it can be minimized by using a strongly focusing lens. Additionally an aperture is also used to reduce the angular deviation of electrons.

The other common aberration is called chromatic aberration; similar to light this type of aberration arises due to electron kinetic energy variations which determine wavelength of electrons. Therefore electrons of different kinetic energies will be focused at different spots.

The kinetic energy variation arises due to several causes. One of the causes of spread in kinetic energy is energy variations during thermionic emission which arises due to statistics of emission. Fluctuation in accelerating voltage is also another cause of energy spread. These causes are intrinsic to the instrument. Additionally chromatic aberration can also arise from inelastic scattering process after interaction with the sample. This is a statistical process and energy loss is not the same for all the electrons. This aberration causes aberration in magnification stage. The aberration is quantified by below given equation.

$$r_s = \alpha C_c \left(\frac{\Delta E_o}{E_o} \right) \tag{2.9}$$

Where C_s is the chromatic aberration coefficient, E_0 is energy and ΔE_o is the energy spread. To reduce this aberration lenses with high focusing power is used. Increase in accelerating voltage also leads to a decrease in this aberration.

Additional problems in focusing also occur due to astigmatism. This arises due to lack of axial symmetry. This is corrected by a stigmator which is quadruple lens.

2. 6. 3. Selected Area Electron Diffraction

Apart from imaging mode, TEM instrument can also be used to obtain electron diffraction patterns. Diffraction occurs due to elastic scattering of electrons in crystalline samples. In a crystalline sample presence of long range order gives rise to rings or spots arising from constructive interference of scattering from different planes. The angular position of spots or rings is related to crystalline structure or symmetry. In a particular crystalline sample there will be several ring or spots placed radially from the central point or un-diffracted beam. The rings that are seen consist of large number of merged spots. The spots arise from diffraction from a particular plane of a crystallite. The radial distance from the centre is related to the lattice spacing and TEM parameters. Since the magnification parameters of TEM are known, lattice spacing can be obtained. Now in a polycrystalline sample azimuthal orientation of crystals with respect to the optic axis is random. Therefore each of these crystals will diffract at different azimuthal angle creating a series of spots radially arranged around an axis as a result it appears like a ring. The position of the rings from the central maxima helps in phase characterization of a material.

2. 6. 3. Electron Energy Loss Spectroscopy (EELS)

In a TEM the electrons impinging on sample are monoenergetic. On interaction with the sample electrons can undergo inelastic scattering. The loss of energy can correspond to plasmon and phonon excitation, band related transition, ionizations etc. These energy loss phenomena mentioned are very specific to a crystal. Additionally inner shell ionizations are specific to a particular element. Therefore we can obtain information on both elemental composition and crystalline property at the same time. This is accomplished by quantifying energy lost by electrons. Very often EELS is used to obtain elemental mapping in a particular sample [2.12].

2.7. Time Correlated Single Photon Counting

2.7.1. Introduction

Previous section dealt with steady state measurement i.e. measurement carried out under equilibrium. One can gain a greater insight into a system from measurements carried out in time domain. For example in a biological system same fluorophore can have vastly different lifetimes depending upon environment. Such species can be easily monitored by a time domain measurements due to large spectral overlap between absorption and emission. Most commonly used time domain measurement is time correlated single photon countung. Here decay profile of a fluorophore is recorded after excitation. Modern TCSPC instruments use pulses as short as picoseconds by modelocking in conjunction with fast detectors, micro channel plate (MCP) and photomultiplier tube (PMT). However, commonly used TCSPC systems use LEDs as the light source and with PMT as detector.

2.7.2. Instrumentation

A typical schematic is of working principle is given in figure 2.3. Principle of TCSPC is based on detection of delay time between excitation and emission photons [2.4, 2.13]. This is done under conditions where detection rate is less than 1 emission photon for 100 excitations. Therefore profile obtained under such conditions represents decay profile of a fluorophore. As shown in the schematic the start of the experiment is by detection of photons from light source which could be LED, laser or lamp etc depending on the instrument. Light source is divided into two parts. One part is sent to a photodiode producing an electrical signal which is sent to constant fraction discriminator (CFD). CFD defines exact point for the START for time to amplitude converter (TAC). TAC consists of the capacitor which charges when START signal arrives and stops when STOP signal arrives from the other CFD. The electrical output generated is proportional to time and forms the basis for time delay detection between START and STOP pulse. The other part excites the sample and emission is monochromatised by a monochromator and sent to PMT which detects emission photon.

The electrical signal is then channeled to CFD and subsequently to TAC, which stops charging. The TAC output is channeled to a MCP which gives a numerical value for the time delay through an analog to digital converter. The value associated is added to different channels corresponding to different delay times and a combined histogram is generated for each of the channels and the waveform obtained is the decay profile at that wavelength.

Once the signal is detected it needs to be analyzed to delink lamp profile and different components in decay. If excitation pulse is a delta (δ)-pulse or sharp pulse and detection is very fast the decay profile is the actual decay of the system. However excitation pulse always has a finite width and detection system also has a finite response time. Therefore the decay profile measured is actually a convolution of decay profile of the samples and the light source. Hence mathematical deconvolution procedure is used to obtain the fits. To perform a deconvolution procedure we need to obtain the profile of the light source. This is done by using a scattering solution with no emission and measure Rayleigh scattering for that excitation wavelength. The profile hence obtained is called an instrument response function. The width contains information on profile of both detector and lamp profile. Decay profiles are generated with a fixed angle between excitation and emission polarization, this angle is called magic angle (54.7˚). This is done to avoid anisotropy effects in decay profiles generated. The maximum decay counts was taken as 5000 or 10000 for all the samples measured. This is done to ensure good statistics for fitting. TAC range used in the present thesis was set from 50-250ns depending on different systems studied in the present thesis.

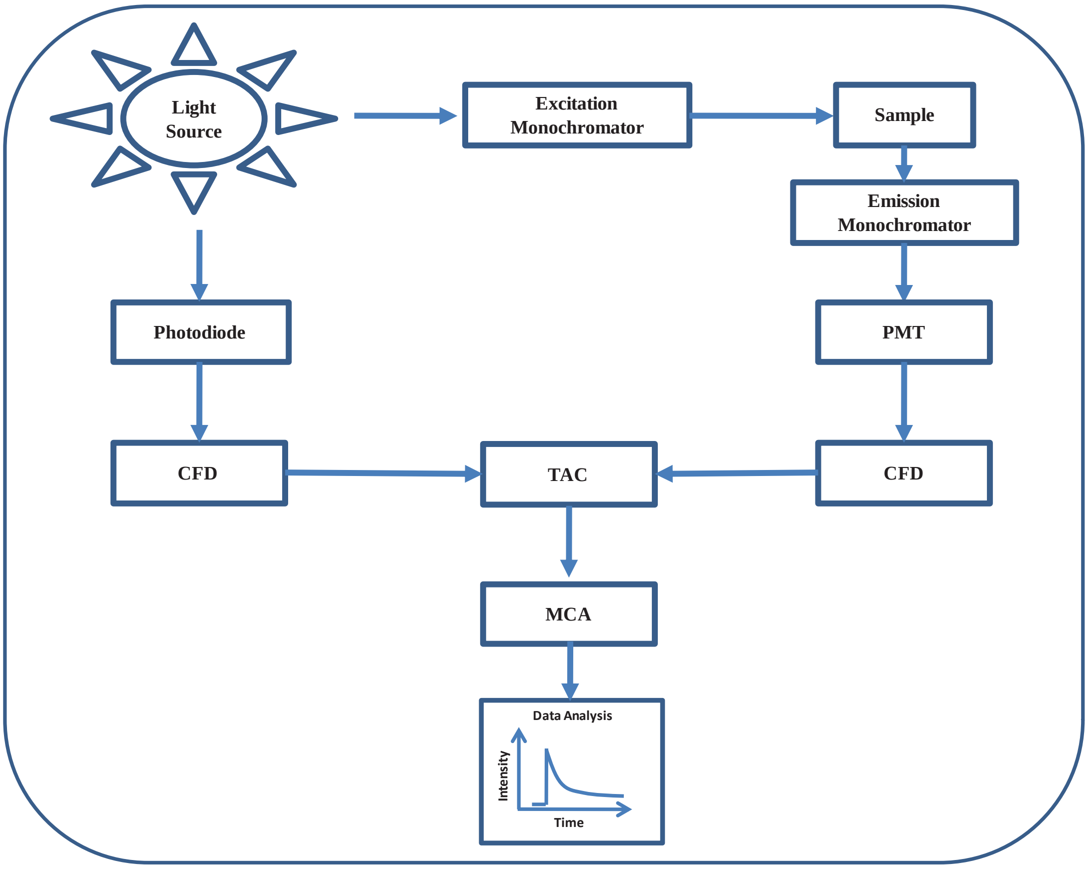
Light
Source
Excitation
Monochromator
Sample
Emission
Monochromator
Photodiode
PMT
CFD
TAC
CFD
MCA
Data Analysis
Intensity
Time

Figure 2. 3. Schematic of working principle of TCSPC technique

2.7.2. 1. Constant Fraction Discriminator

CFD is a signal processing device used as a timing device where exact time position of arrival of a signal is to be obtained. A CFD is introduced in TCSPC in presence of a simple leading edge discriminator as in a leading edge discriminator the varying signal amplitudes introduce timing errors. Since signals generated in PMT have a pulse height distribution, timing errors are introduced which can affect timing measurements. CFD used a constant fraction of the input pulse to moderate this problem. In a CFD, input pulse is split by half, so that one half of the signal is a constant fraction of the input and the other half is delayed and inverted. The two signals are then added and zero crossing time is taken as the timing trigger.

2.7.2. 2. Time to Amplitude Converter

TAC is device that generates time interval between two events. This is done by generating an amplitude signal which is proportional to time between the events. In TAC, START is zero time and until the STOP signal arrives, TAC generates an electrical output. Therefore timing between the START and STOP is proportional to output of TAC. The TAC range is initially defined so that complete decay profile can be generated within the channels of MCA. If the signal does not arrive within the TAC range the TAC is reset and it waits for the next START signal. After STOP signal arrive TAC has a waiting period as it consists of a capacitor which needs to be completely discharged.

2.7.2. 3. Multichannel Analyzer

Multichannel analyzer is a series of single channel analyzer with a fixed voltage width (from TAC) and increasing voltage. Thus a plot of signal with increasing channel number gives decay profile a species. The data is digitized so can be read in a computer and analyzed.

2.7.2. 4. Data Analysis

As mentioned earlier the data that we obtain is convoluted profile of instrument response and decay profile of fluorophore. Therefore a deconvolution procedure needs to employed to retrieve lifetime values. Let us consider $F(t)$ to be obtained decay curve. $F(t)$ is a convolution of IRF, $R(t)$ and fluorescence decay $I(t)$. The IRF is assumed to a series of δ function with amplitude proportional to intensity for that time. Therefore IRF can be written as sum of δ functions for varying times. Therefore,

$$F(t)=\int_{0}^{t} R(t)I(t-t^{'})dt^{'} \qquad (2.10)$$

Since $R(t)$ and $F(t)$ is known, $I(t)$ can be obtained by least square fit with χ^2 close to 1.

2.8. Broadband Pump-Probe Femtosecond Transient Absorption Spectroscopy

2.8. 1. Introduction

Photoinduced relaxation processes involve both radiative and nonradiative relaxation. Techniques like TCSPC measure dynamics for radiative relaxation processes. Gaining complete relaxation behavior of a system involves study of both radiative and non radiative relaxation [2.14]. For example as discussed earlier in chapter 1, relaxation mechanisms of quantum dots like cooling and recombination dynamics, involve non radiative relaxation like Auger processes and trapping etc [2.15]. One of the techniques that is widely used to study these processes is transient absorption where we measure changes in absorption occurring on photoexcitation. For the present study we use visible pump and visible-near infrared (NIR) probe to study the dynamics. Since changes in absorption are monitored, information on both radiative and non radiative relaxation processes can be obtained. The technique used in the present thesis is broadband visible pump-visible NIR probe spectroscopy.

Pump-probe technique is one of the simplest and most commonly used transient techniques to interrogate a photoinduced reaction dynamics [2.16-2.18]. As the name suggests the sample is first photoexcited by a pump and investigated by a broadband probe pulse. The dynamics is measured by delay between the pump and the probe pulses at different wavelengths. The temporal resolution of the setup is mainly limited by the pulse duration of pump and probe pulses. The pump pulse first excites the molecule and places the molecules into a new electronic state. Probe pulse spatially overlapped with pump pulse with an adjustable time delay from pump monitors the new electronic state or bleach of ground state. The time delay between pump and probe pulses are accomplished by varying the optical path length between the two pulses. For e.g. light waves travel a distance of 1μm in 3.3 fs in air, therefore enabling time delay by introducing an optical delay. Typical schematic of a pump-probe setup is given below.

The measurement of dynamics is achieved by first introducing a time dependent perturbation in this case by using pump pulses at t = 0. The probe pulse interrogates the sample at $t+\Delta t$, Δt is variable delay. The detector in this case a photodiode measures the probe pulse intensity before $I_{0,\nu}$ and after $I_{\nu,\Delta t}$ the perturbed sample at frequency ν. From Beer-Lambert law,

$$I_{\nu,\Delta t} = I_{0,\nu} \times 10^{-\varepsilon_\nu N_{\Delta t} l} \qquad (2.11)$$

In the above equation ε_ν is the molar absorption coefficient at frequency ν *;* $N_{\Delta t}$ is the number of molecules absorbing at time Δt at frequency ν and l is the path length of sample.

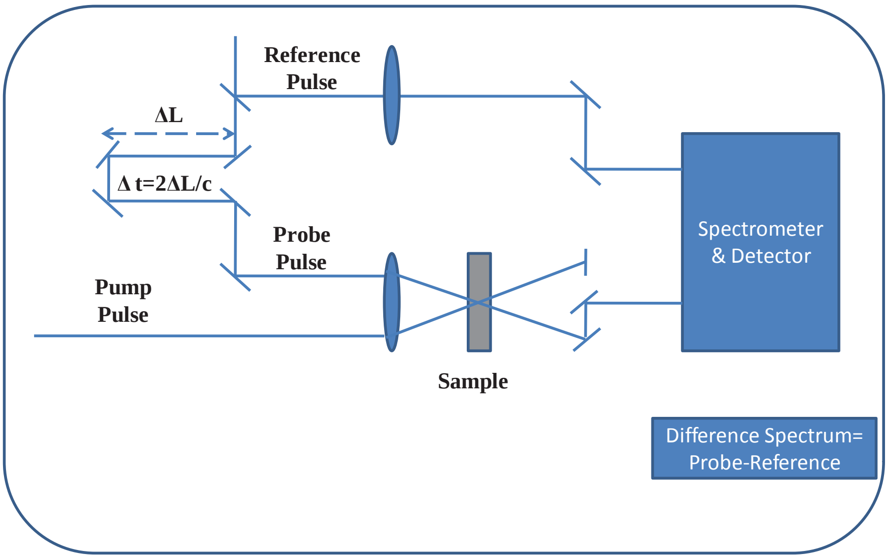
Reference
Pulse
ΔL
Δ t=2ΔL/c
Probe
Pulse
Pump
Pulse
Sample
Spectrometer
& Detector
Difference Spectrum=
Probe-Reference

Figure. 2.4. Schematic of a pump-probe set up

The measured Absorbance is defined as

$$A_{\nu,\Delta t} = \log\left(\frac{I_0}{I_{\nu,\Delta t}}\right) = \varepsilon_\nu N_{\Delta t} l \tag{2.12}$$

Time-resolved information of dynamics of transients are provided by time dependent changes in absorbance at that frequency.

$$\ln A_{\Delta t} = \ln N_0 \varepsilon_\nu l - {\Delta t}/{\tau} \tag{2.13}$$

The typical set up used for performing Femtosecond transient absorption spectroscopy is described in the figure 2.5.

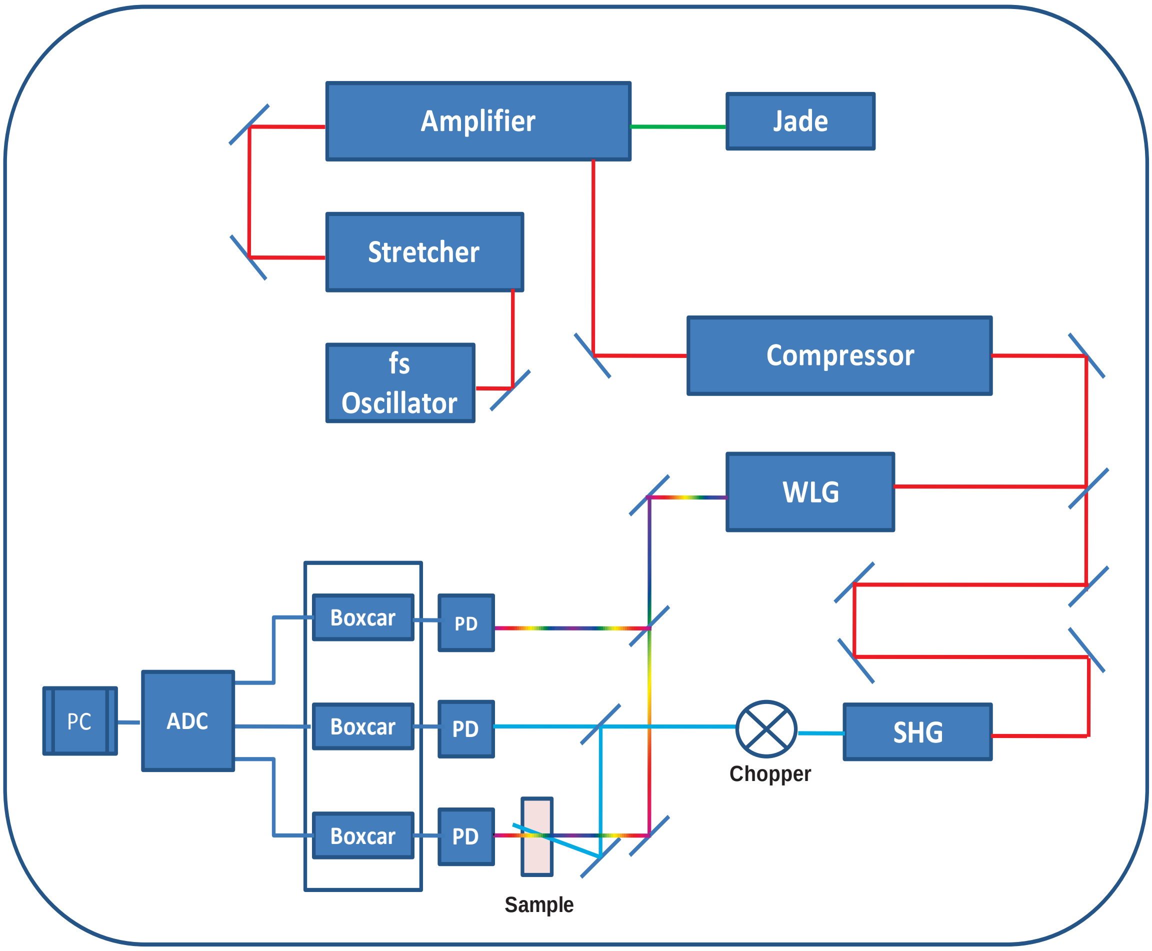
Amplifier
Jade
Stretcher
fs Oscillator
Compressor
WLG
Boxcar
Boxcar
Boxcar
PD
PD
PD
PC
ADC
Chopper
SHG
Sample

Figure. 2.5. Schematic of a pump-probe set up used in the present thesis

The white light continuum probe beam is split into signal and reference beams using a neutral density filter. The beam defined as signal beam is focused into the sample cell of 1 or 2 mm path length. The sample solution in the cell is circulated by a peristaltic pump for measurements to reduce degradation of the sample during measurement. Dependence on reorientation effects of molecules on dynamics is eliminated by adjusting pump probe polarization to 54.7^0 (magic angle). The pump and signal probe beams are focused non-collinearly on sample cell. The signal reference and pump beams are measured by integrating photodiodes for each pulse. Mechanical Chopper is operated at 500Hz to divide pump pulses into pump and no-pump condition since frequency of pump is 1kHz. Signal at no-pump condition is taken as I_0 and at pump condition is I. Absorbance change is negative logarithm of I/I_0. The noise from laser fluctuations is corrected by comparing signal and reference beams by using ratio to the signal.

2. 8. 2. Experimental set up

2. 8. 2. 1. Ti-Sapphire (Ti-S) Oscillator

The first processes involve in creation of pump pulses for the experiment is obtaining the femtosecond pulses. This is accomplished in Ti-S oscillator by a process called as self phase modulation [2.19, 2.20]. The Ti-S crystal in the oscillator is pumped by a second laser called diode pumped solid state laser (DPSS). The DPSS laser has an output of 532nm and 3.8W in continuous wave mode (CW). For high intensities of pump, the refractive index of Ti-S medium is an intensity dependent quantity and can be written as

$$n(\nu, I) = n_0 + n_2(\nu)I \tag{2.14}$$

n_0 is the refractive index for frequency ν under normal conditions; $n_2(\nu)$ is the nonlinear component of refractive index in the above equation. Since $n_2(\nu)$ is positive for Ti-S, at high intensity the medium itself acts as convex lens. Since the laser is operated in TEM_{00} mode, central part of the beam has a greater intensity; therefore the beam converges towards the center.

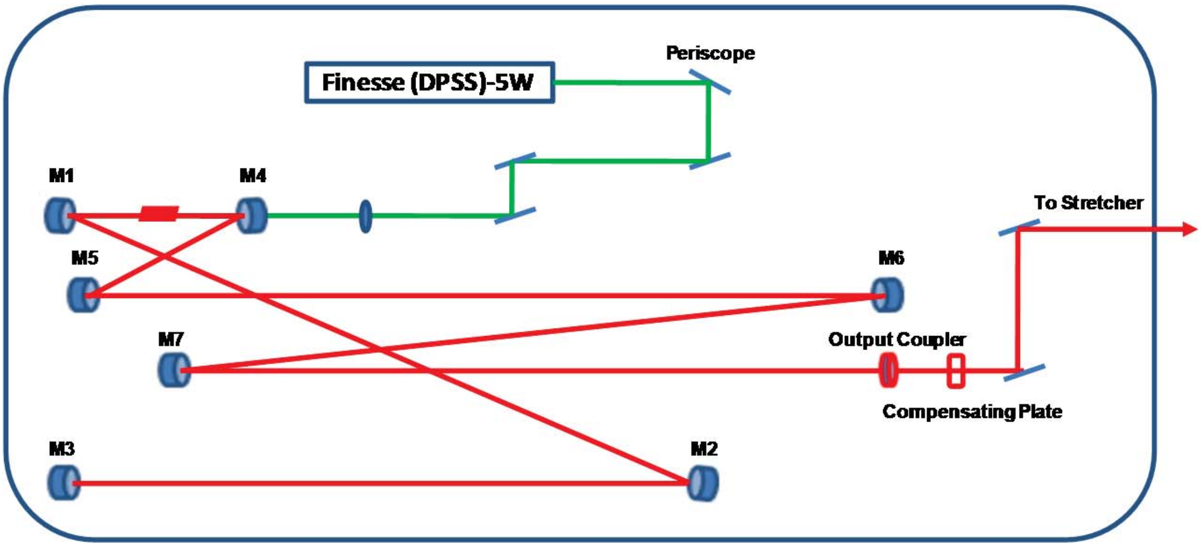

Figure 2.6. Optical layout of Ti-S Oscillator used in the present studies.

Generally beams from DPSS are focused through mirrors on the either side of Ti-S medium; an additional focal length component is added due to self-focusing inside Ti-S medium. The additional focal length of Ti-S medium at a particular intensity makes the resonator stable for close to pulse maximum thereby enabling production of a femtosecond pulse. By this process a <10fs pulse can be achieved with energies of ~nJ. Such a mode locking process is called Kerr-Lens mode locking. The repetition rate is defined by cavity round trip time, in the present set up it is ~100MHz. Since mode locking is achieved by highly nonlinear interactions, significant group velocity dispersion (GVD) is introduced in the pulse. GVD is compensated by use of chirped mirrors which shapes the pulses [2.21]. Additionally the intensity of light due to self focusing also lead to birefringence of the crystals therefore polarization of light is also affected. This is compensated by Brewster angle cut Ti-S crystals. For most of the present study we use a Femtosource synergy oscillator with ~50fs (FWHM), 500mW (~3.8W) and 88MHz.

2. 8. 2. 2. Amplifier

As mentioned earlier femtosecond pulse energies from Ti-S oscillator are too low to perform transient absorption measurements. Therefore these pulses have to be amplified several orders of magnitude for experiments. This can be achieved by use of amplifiers. Because pulse durations are in fs time domain and during amplification peak power of the pulse increases by orders of magnitude, it can lead to irreparable damage to the optics. Therefore the fs pulses are chirped and broadened temporally to ~100ps before amplification. Therefore this technique is called as chirped pulse amplification [2.22]. After amplification we again compress the pulse to fs time domain. The typical amplifiers generally achieve an enhancement of five orders of magnitude. A typical layout of the process is given in the diagram. Stretching the pulse involves use of dispersive elements like prism or gratings to create group velocity dispersion. A typical schematic of stretcher is given in the figure 2.7.

In the present set up used, the pulse width is ~50nm. On incidence of the femtosecond pulse on the stretcher red and blue wavelengths are diffracted at different wavelength. Therefore the path difference between the different wavelengths is used to stretch the pulse. This creates an effect of stretch in terms of time. The schematic also describes the stretcher used in present study. The present set up uses a type of stretcher called an Offner stretcher. The stretcher consists of a Grating and a combination of silver coated concave and convex mirrors. The focal length of the convex mirror is half of the focal length of concave mirror and the mirrors are separated by ~30cm. The stretched pulse on hitting the grating is elongated therefore after stretching the pulse needs to be reconstructed without losing the chirp introduced by stretcher. The exact arrangement of mirrors allows us to do just that. The stretch introduces in time is ~300ps after the stretching stage.

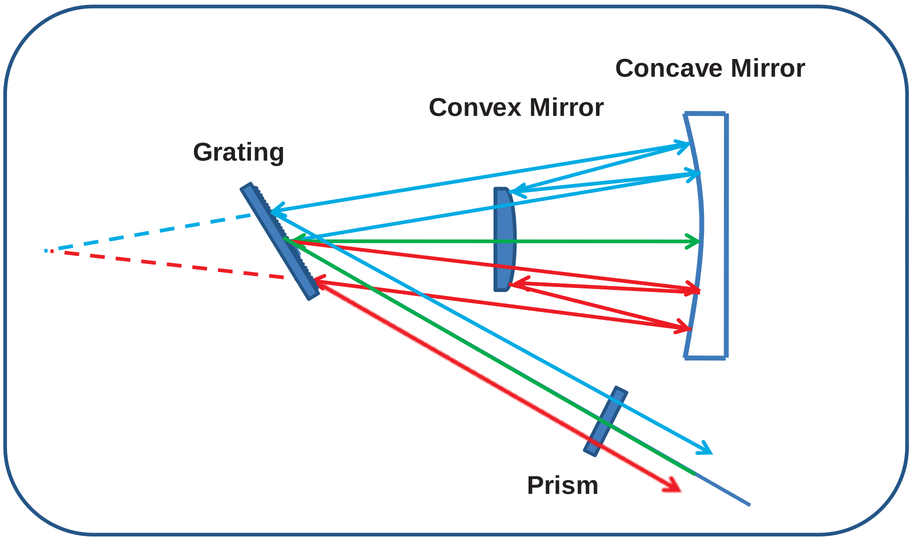

Figure 2.7. Schematic of Offner Stretcher

2. 8. 2. 3. Multistage Amplification

The amplification is achieved through a two-step process. The first stage is a regenerative amplifier and the second stage is a multipass amplifier. In both of the amplification stage Ti-S is used as the gain medium.

The amplifier used in the present study uses a combination of regenerative amplifier and a multipass amplifier. In a regenerative amplifier the seed pulses from stretcher are chosen and trapped in a cavity for amplification. This is accomplished by a combination of optical isolator, Pockels cell and polarizer. For the purpose of amplification of the seed pulse another laser is required which pumps the gain medium which is Ti-S in the present system. The pump pulse used in the present system is a diode pumped solid state laser which gives a power of 20W. The output produced is a second harmonic of Nd:YLF. YLF is naturally birefringent and can sustain high powers with few kHz repetition rate. The output beam is multimodal and circular. The second harmonic is generated in Lithium triborate (LBO) which is isolated by a dichroic mirror. The diode pump chamber, acousto-optic crystal and LBO are cooled by water maintained ~20C. In the present study the pump laser used is JADE from Thales Lasers. The output energy, wavelength, polarization and repetition rate are 20W, 527nm, horizontal and 1kHz respectively. The pulse width of JADE is ~280ns.The design of JADE laser is described in the figure 2.8.

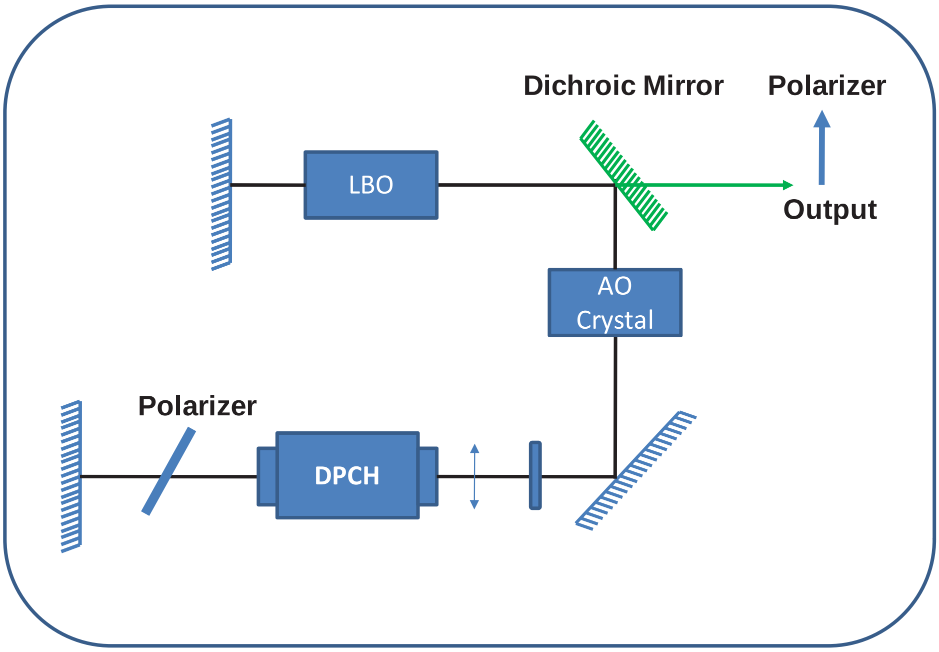

Figure 2.8. Optical layout of JADE laser used for amplification.

Layout of regenerative amplifier is given in the figure 2.9. The amplifier cavity is linear and consists of highly reflective mirrors for 800nm light. The gain medium used in the present system is Ti-S. The regenerative amplifier is pumped by JADE and is seeded by the stretcher output with pulses stretched to hundreds of ps. The polarization of seed pulse from stretcher is horizontal. The seed pulses go through a wave plate and faraday isolator, this changes the polarization from horizontal to vertical. The vertically polarized seed is reflected by a combination of 2 polarizers adjacent to faraday isolator. When these pulses enter in the amplifier, they are passed through combined wave plate and faraday rotator (also called as optical path selector), changes its polarization from horizontal to vertical. These pulses are then reflected by the polarizers (reflects only vertically polarized light). Next the pulses enter Pockel cell. When no voltage is applied to the Pockels cell it functions as a quarter wave plate. Therefore a round trip in Pockel cell changes the polarization of the seed pulse to horizontal. Since polarizer T_p reflected only vertically polarized light, horizontally polarized seed enters Regen cavity. When pulse enters Regen cavity high voltage is applied to Pockel cell making it function as a half wave plate. Therefore pulses entering Pockel cell will have their polarization unchanged during a round trip. This seed pulse then extracts stored energy in Ti-S pumped by JADE. The trapped pulses make several round (8ns round trip time) trips between highly reflective mirrors until it extracts energy from Ti-S. The pulse is amplified during each round trip and when seed pulse is in the cavity no other pulse is allowed to enter the cavity. Typically the seed pulse makes 15 to 20 round trips for maximum amplification. After amplification the pulses are extracted. By again changing polarization from horizontal to vertical using Pockel cell the pulses are reflected by polarizers and are extracted out of the cavity and fed into the 2 pass amplifier. Amplification obtained in the regen is typically 10^5. The next stage of amplification is by a 2-pass amplifier. This amplifier also has a Ti-S gain medium and is pumped by part of JADE output. The amplifier consists of a mirrors and the input pulse passes through the amplifier and is extracted by these arrangement of mirrors.

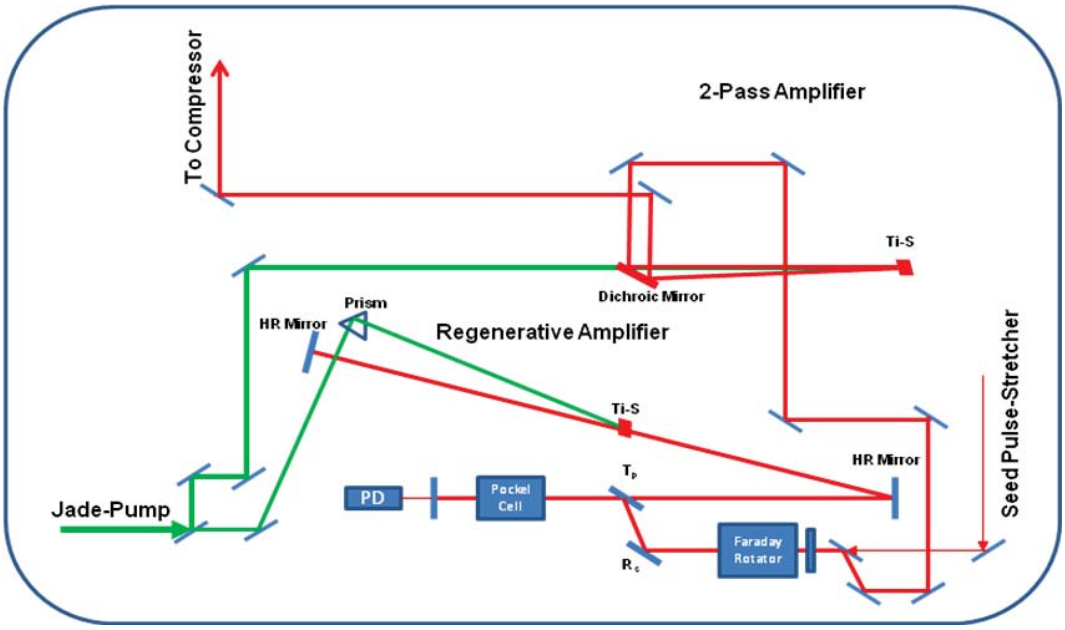
To Compressor
2-Pass Amplifier
Ti-S
Dichroic Mirror
Prism
HR Mirror
Regenerative Amplifier
Ti-S
Seed Pulse-Stretcher
HR Mirror
Jade-Pump
PD
Pockel Cell
T_p
R_s
Faraday Rotator

Figure 2.9. Optical layout of 2-Stage Amplifier.

In the present thesis we have used a combined multistage regen/2-pass amplifier Alpha 1000 from Thales Laser system (France). The amplifiers are pumped by second harmonic of JADE laser which is a Q-switched Nd:YLF at 527nm, with ~300ns. JADE output is ~18W and ~5W is used in REGEN and ~13W is used in multipass amplifier. The output pulse from amplification is ~3.5W. The synchronization of Q-switching and Pockels cell is done by synchronization unit Masterclock. The amplified pulse is fed into the compressor to shorten the pulse duration back from hundreds of ps to fs time domain.

2. 8. 2. 4. Pulse Compressor

The schematic of compressor is given in the figure 2.10.

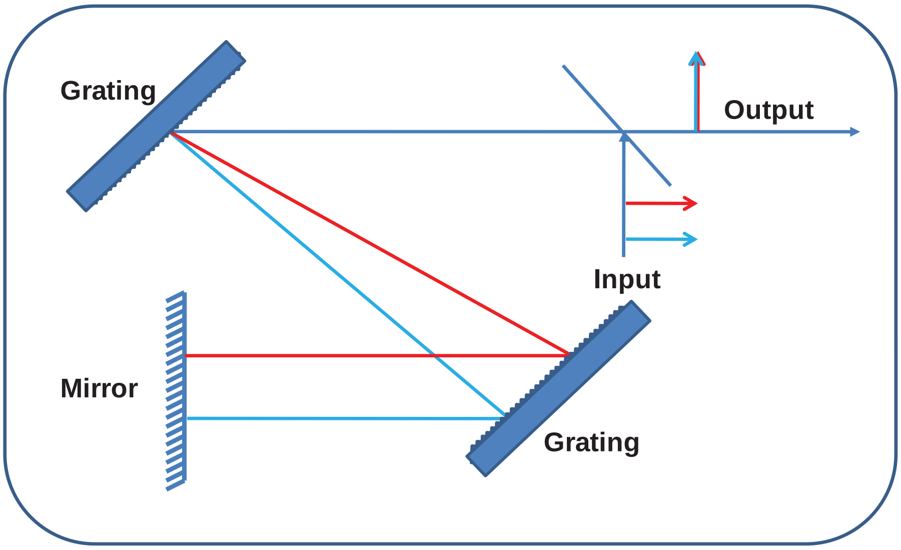

Figure 2.10. Schematic of a typical compressor.

The compressor consists of pair of gratings placed parallel to achieve negative dispersion. The negative dispersion delays the red part of spectrum compared to blue. The compressed pulse has duration of 50fs. Since the amplified pulse has a very high peak power this pulse can be exploited to exhibit nonlinearity, which in turn is useful in second harmonic and white light generation. The compressed pulse has energy of 1.13W with wavelength centered at 800nm. This pulse is used to generate 400nm pump and white light ranging from 450nm-1100nm used as the probe for our studies.

2. 8. 3. Second Harmonic Generation-400nm Pump

The second harmonic generation of 800nm output of Ti-S amplifier system is accomplished by using β-barium borate (BBO). The induced dielectric polarization in a material in presence of electric field of light is given by

$$P = \varepsilon_0(\chi^{(1)}E + \varepsilon_0\chi^{(2)}E^2 + \varepsilon_0\chi^{(3)}E^3 + \ldots) \tag{2.15}$$

Here E is the electric field of light, $\chi^{(n)}$ is the susceptibility of nth nonlinearity and magnitude decreases for the higher nth order terms. Therefore it is clear from the equation that harmonic generation is present only when light intensities are very high. For many crystals used for SHG is seen for light intensities of the order of GW/cm^2.The second term in the equation is responsible for second harmonic generation.

Let's consider the second order term

$$P_2 = \varepsilon_0 \chi^{(2)} E^2 \tag{2.16}$$

For an electromagnetic wave $E = E_0 \cos(\omega t - kr)$,

$$P_2 = \varepsilon_0 \chi^{(2)} E_0^2 \cos^2(\omega t - kr) = \frac{1}{2}(\varepsilon_0 \chi^{(2)} E_0^2 + \varepsilon_0 \chi^{(2)} E_0^2 \cos 2(\omega t - kr)) \tag{2.17}$$

Additionally harmonic is generated only if the phases of the two waves match. This condition is given by $k(\omega) = k(2\omega)$. This condition is satisfied in uniaxial birefringent crystals like BBO that have two different refractive indices n_o and n_e for the ordinary and the extraordinary waves where $n_e(2\omega, \theta) = n_o(\omega)$. In our set up we use pulse energy of ~100μJ/pulse at 800nm which is focused on 0.5mm BBO crystal to generate ~10μJ/pulse of second harmonic at 400nm.

2. 8. 4. White Light Generation- 450-1100nm Probe

To monitor transients after a pump pulse excitation, we use a probe pulse with wavelengths ranging from visible to near IR region. This is done by creating white light using a part of 800nm amplified output. The phenomenon responsible for generation of white light is self phase modulation. The 800nm pulse with time duration of 50fs and energy of few μJ has a very high peak power. Under this high intense regime refractive index is a function of light intensity. For a Gaussian pulse, temporal intensity profile can be described by

$$I = I_o \exp\left(-\frac{t^2}{\tau^2}\right) \tag{2.18}$$

An intense pulse with a Gaussian profile leads to phase change which in turn changes the frequency and broadens the pulse. Additionally the nonlinear interaction introduces a frequency chirp i.e. for a positive nonlinear refractive index leading edge of the pulse is downshifted in frequency. In our system white light is generated by focusing ~ few μJ 800nm pulse on 1.5mm sapphire thick plate as shown in the below given schematic.

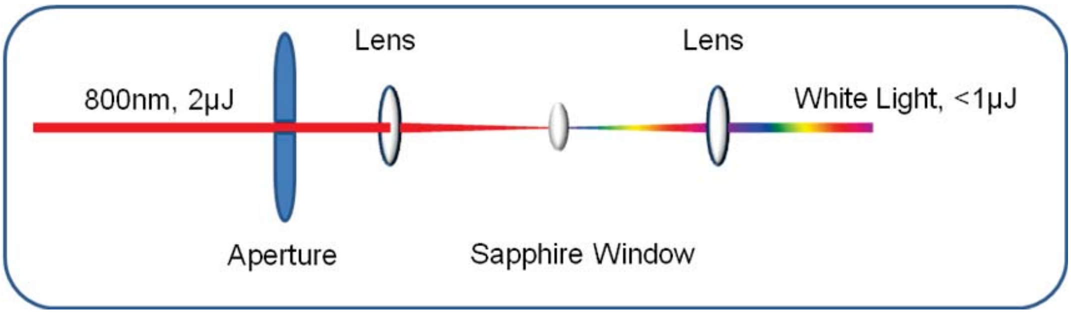

Figure 2.11. Schematic of a WLG in set up used for present studies.

2. 8. 5. Laser diagnostics

The pulse obtained after compression is diagnosed by Autocorrelator to obtain its time profile. The schematic of an autocorrelator is given in the figure 2.12. The input beam is split into exactly 2 equal parts where one of beams moves through an optical delay and they are made to converge at a SHG crystal. Since efficiency of SHG is directly proportional to the intensity. In the present study we used a model ASF-20 autocorrelator for pulse width diagnostic. Additionally average power and stability of the pulses are monitored by Coherent field master and oscilloscope of Tektronix makes (TDS-200).

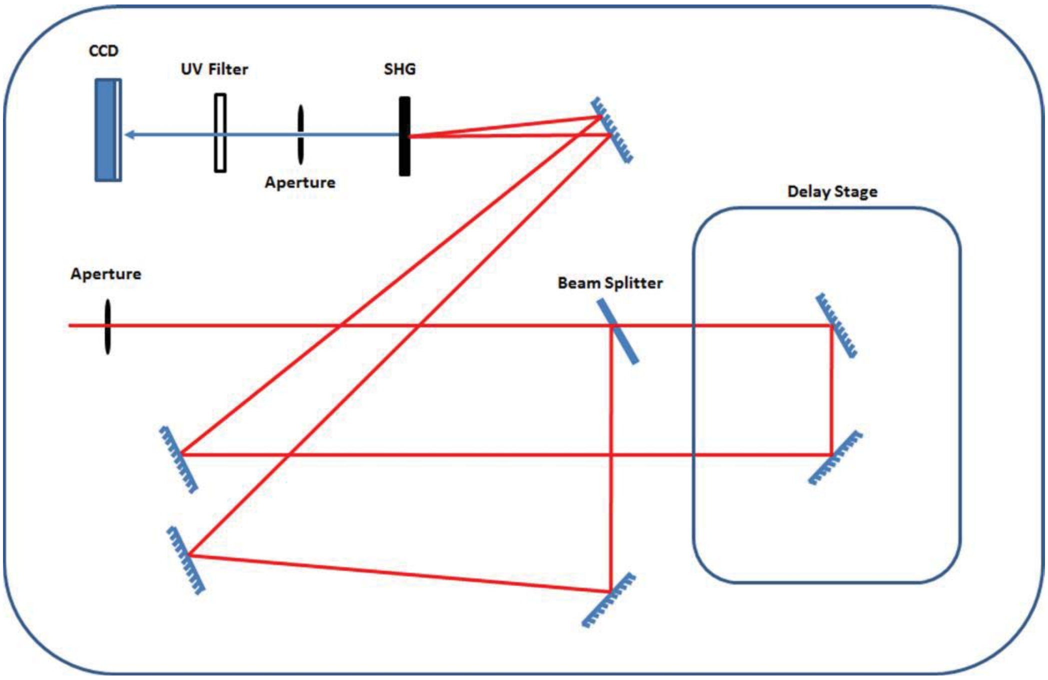

Figure. 2.12. Schematic diagram of autocorrelator

2.9. References

2.1. Modern Spectroscopy, J. Michael Hollas, 1996, 3rd Ed., John Wiley and Sons.

2.2. Quantitative Spectroscopy: Theory and Practice, B. C. Smith, 2002, Academic Press.

2.3. Spectra of atoms and molecules, P. F. Bernath, 1995, Oxford University Press.

2.4. Principles of Fluorescence Spectroscopy, J. R. Lakowicz, 2010, Springer.

2.5. Principles and applications of Fluorescence Spectroscopy, J. R. Albani, 2007, Blackwell Publishing.

2.6. Dynamical Theory of X-Ray Diffraction, André Authier, 2001, IUCr & Oxford Science Publication.

2.7. X-Ray Diffraction, B. E. Warren, 1990, Dover Publications.

2.8. Joint Committee on Powder Diffraction Standards (JCPDS), International Centre for Diffraction Data (ICDD), Swarthmore, PA.

2.9. Introductory Raman Spectroscopy, John R. Ferraro, Kazuo Nakamoto and Chris W. Brown, 2nd Edition, 2003. Elsevier Inc.

2.10. Transmission Electron Microscopy, David B. Williams, Carter, C. Barry, 2nd Ed., Springer Series.

2.11. Transmission Electron Microscopy- Physics of Image Formation, L. Reimer, H. Kohl, 5th Ed., Springer Series.

2.12. A. R. Lupini, S. J. Pennycook, Ultramicroscopy, **2003**, *96*, 313.

2.13. Time-Correlated Single-Photon Counting, D. V. O'Connor, D. Phillips, **1984,** Academic Press: London.

2.14. Analysis and control of ultrafast photoinduced reactions. O. Kuhn, L. Wöste, 2007, Springer Series in Chemical Physics.

2.15. Ultrafast spectroscopy of semiconductors and semiconductor nanostructures, J. Shah, 1999, 2nd Ed., Springer.

2.16. Chemical Applications of Ultrafast Spectroscopy (International Series of Monographs on Chemistry), G. R. Fleming, 1986, Oxford University Press.

2.17. Ultrafast Spectroscopy, G. R. Fleming, Laura J. Kaufman, John Wiley and Sons.

2.18. J. Manz, L. Wöste, Femtosecond Chemistry, Vols. I and II, VCH, New York, 1994.

2.19. R. L. Fork, B. I. Green, C. V. Shank, *Appl. Phys. Lett.* **1981,** *38*, 671.

2.20. Photonics: Linear and Nonlinear interaction of laser light and matter, R. Menzel, 2nd Ed., 2001, Springer.

2.21. A. Stingl, M. Lenzner, Ch. Spielmann, R. Szipocs and F. Krausz, Opt. Lett, 20, **1995**, 602.

2.22. C. Rulliere, "Femtosecond Laser Pulses; Principles and Experiments", Springer, **1998**.

Chapter 3

CHAPTER 3

Charge Carrier Dynamics in Ultrasmall TiO_2-Alizarin System

3.1. Introduction:

Solar energy conversion in the recent times has emerged as the ideal choice for solution of the energy crisis that is plaguing energy hungry economy because it is nonpolluting, abundant and longevity of the resource with several billion years. This has led to increased involvement of scientists in the research involving the tapping the energy by means of a “solar cell”. One of the approaches towards solar energy trapping that have gained importance in the recent times due to its cost effectiveness is the dye sensitized solar cell (DSSC) or the so called “Gräetzel Cell”[3.1]. The choice of semiconductor for this application has been TiO_2, because it is inexpensive, non-polluting and gives a very high photon to current conversion efficiency. Efficiency of the best dye sensitized cell was about ~10% [3.2] using TiO_2. This approach relies on sensitization of wide band gap semiconductor like TiO_2 with a dye since TiO_2 itself does not absorb in the visible region of the solar spectrum. Organic dyes have been used for sensitization of the semiconductor as they had a very high absorption coefficient of absorption of the dye; these dyes were replaced by Ru-based MLCT complexes. It was realized that injection time of the electron in the semiconductor, the efficiency of the electron injection, the back electron transfer time, the free energy of the reaction etc; all of these factors govern the overall efficiency of the cell.

Therefore the study of interfacial electron transfer dynamics between the dye and semiconductor could give information not only on the dynamics but it could also throw light on the relationship between the dynamical variables and the efficiency of the solar cell. The studies on the dye sensitized TiO_2 revealed that the injection times for most of the dyes take place in ~ 100fs [3.3-3.4]. This is due to the fact that the TiO_2 has a very large density of states owing to a very large electron effective mass, leading to a large electron coupling between the semiconductor and the dyes. However, the back electron transfer times show considerable variation between different dyes. The time scales for the back electron transfer process ranges from hundreds of fs to milliseconds [3.5-3.13]. Electron transfer parameters are very important factors for designing an efficient solar cell. One of the dyes that have been widely studied for sensitization is alizarin, due to the fact that this dye has absorption from 400-500 nm and is known to form a strong complex with TiO_2. This leads to an interesting phenomenon, i.e. formation of a charge transfer complex on the surface of TiO_2 [3.3, 3.4, 3.14]. This type of CT complex leads to a direct injection of the electron from the HOMO of the dye to the conduction band of the electron. But this issue to still not understand well, because recent theoretical results show that even in a very strong binding dye like alizarin molecule, electron transfer takes place from the LUMO of the dye to the TiO_2 conduction band rather than via a CT mechanism. The electron transfer in this case takes place adiabatically within 6 fs, which is expected of a strong binding dye [3.4]. Huber et al [3.4] in the study of electron injection from alizarin to TiO_2 reasoned that in a strong coupling dye like alizarin, the ultrafast electron injection can be explained on the basis of adiabatic process. The adiabaticity in the electron transfer process implies that the electron transfer takes place in the same Born-Oppenheimer surface and therefore is less dependent on the density of states. However, if one is dealing with a size confined system where there exists discreteness in the conduction band then if the electron injection is adiabatic then we will not observe multi-exponential injection due to the fact that electron injection will be much less dependent on the density of states. However, in case of nonadiabatic mechanism we would observe a slow multi-exponential injection in a size quantized system. Such multiple injection has been observed in N3 sensitized ZnO [3.15]. The main reason for the multiple electron injection has been reasoned as due to discreetness of the conduction band in a size quantized system. In the present study we have carried out interfacial electron transfer dynamics studies on alizarin sensitized ultrasmall, surface modified TiO_2. We find that the injection dynamics is multiphasic, with a slower back electron transfer. We also compare the dynamics results in ultrasmall TiO_2 with surface modified bulk TiO_2. The results of the present study show the first evidence of the finite size effect on the electron injection in TiO_2. The results of this study are particularly important in fabricating extremely efficient solar cells as the study shows that like molecular engineering one can manipulate the band gap to optimize or rather increase the performance of a solar cell opening up another path called the Band Gap Engineering approach to TiO_2 based solar cells. Also the result proves that even in a strong binding dye there might be some nonadiabaticity to the electron injection process. Furthermore, in a nanoparticle after injection in the conduction band the energy of the electron often released via phonon emission, which leads to lesser output voltage. However, in a QD the hot electron itself can be extracted thereby leading to lesser loss of energy and voltage.

3. 2. Experimental Section

3.2.1. Materials: Titanium(IV) tetraisopropoxide {$Ti[OCH(CH_3)_2]_4$} (Aldrich, 97%), benzophenone (Aldrich), Trioctylphophineoxide, TOPO (Aldrich), toluene (Aldrich), methanol (Aldrich), acetone (Aldrich).

3.2.2. Preparation of ultrafine TiO_2 nanoparticles:

The ultrafine TiO_2 nanoparticles have been prepared by arrested precipitation method. Briefly 15 gm of benzophenone was heated to a temperature of 200°C in an Ar atmosphere. This temperature was held for ½ hour and further heated to 300°C. At this temperature, benzophenone itself behaves as solvent. Titanium tetraisopropoxide (distilled before the use) was rapidly injected into above solvent. On injection the solution temperature decreases by 15°C and maintained the reaction mixture at 280°C for further 15 min. The solution was cooled to 80°C and methanol was added for the precipitation of TiO_2. The precipitates were centrifuged and repeatedly washed with methanol and acetone and dispersed in toluene and then re-precipitated 3 times and dried in the ambient for further studies. The nanoparticles capped with and trioctylphosphine oxide (TOPO) and benzophenone will be referred to as T-TiO_2 and B-TiO_2 hereafter.

3.3. Results & Discussion

3.3.1. TEM & XRD Studies

The HRTEM image of the samples showed that average particle size is ~3.4nm. TEM analysis revealed particles with a narrow size distribution. The sizes of the particles were in the size range 3.3–3.8 nm (TEM not shown). HRTEM results displayed in figure 3.1 show that the particles are of anatase phase. This was also confirmed by SAED. The EDAX analysis confirmed atomic ratio of Ti and O for TiO_2.

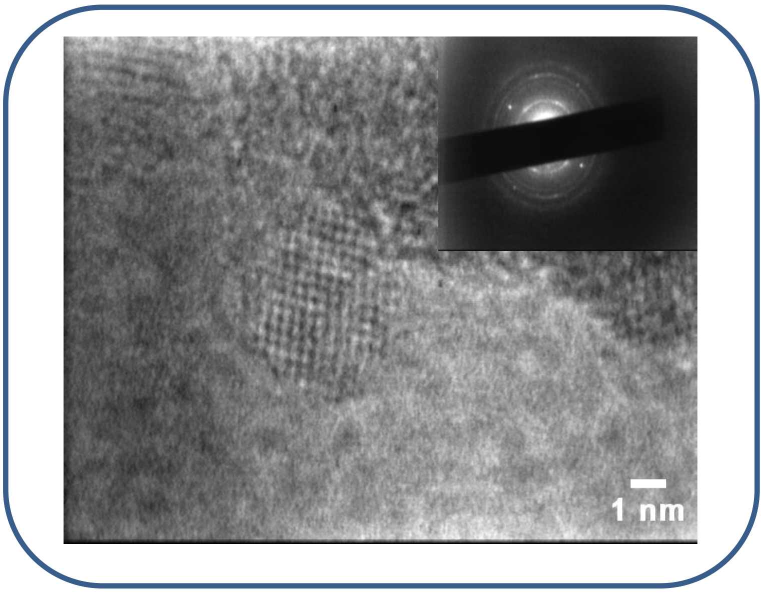

Figure 3.1. TEM and SAED patterns of B-TiO_2 sample

The samples were also characterized by XRD to obtain and confirm the phase information obtained from HRTEM and SAED. The XRD patterns are represented in Figure 3.2. The XRD patterns could be indexed to the anatase phase of TiO_2. The peak position and intensity of corresponding planes are also displayed in the figure. Additionally XRD peak positions and intensity show absence of other TiO_2 phases like brookite and rutile. From the XRD pattern we can conclude that the anatase phase is the only phase present with absence of amorphous phase. The peaks are also broadened clearly indicating nm domain size of particles.

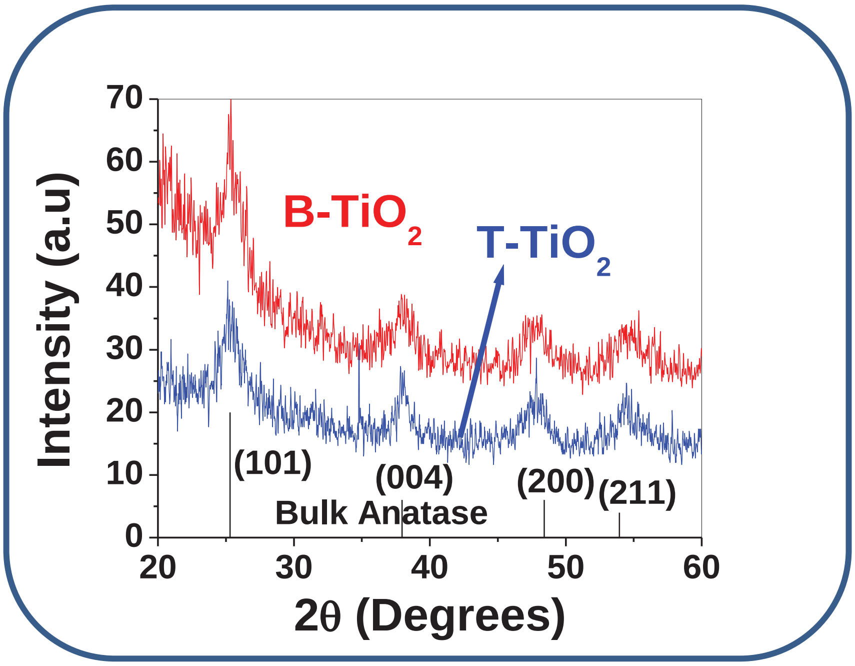

Figure 3.2. XRD patterns of TiO_2 *samples*

3.3.2. Steady State UV-Vis Absorption Studies

To study interfacial ET dynamics it is very important to monitor optical absorption spectroscopy of dye molecules in presence of nanoparticles. Figure 3.3 shows the optical absorption spectra of the dye in toluene (3.3b) and on TiO_2 (3.3c). It is clearly observed from the figure that the absorption peak appears in toluene at ~421 nm. However, in presence of TiO_2 particles the absorption peak broadened considerably towards the red side.

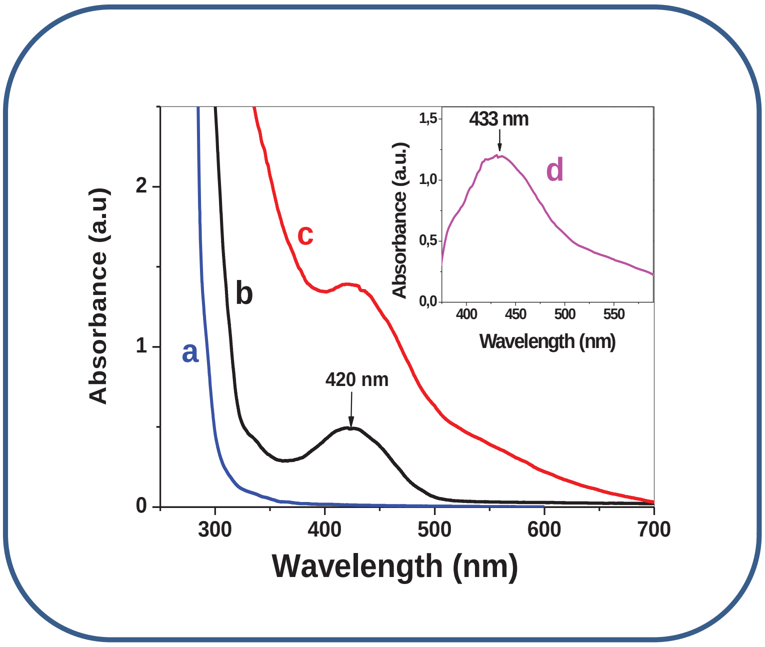

Figure 3.3: Optical absorption spectra of (a) benzophenone modified TiO_2 (B-TiO_2) in toluene (1 gm/L), (b) alizarin (Alz) in toluene (c) Alz sensitized B-TiO_2 in toluene and in inset: (d) difference spectra between c and b, which gives indication the formation of charge transfer (CT) complex between Alz and TiO_2.

We have shown the subtracted spectrum is given in the inset in figure 3.3. The spectrum clearly shows a red shifted peak at ~433nm. It is well known in the literature that alizarin and TiO_2 nanoparticles forms charge transfer complex due to strong interaction. The binding of the dye to the TiO_2 surface takes place via the catecholate linkage with the formation of 5-membered ring between the surface Ti-OH linkage and the OH moiety on alizarin. These results are in accordance with previous studies on the alizarin- TiO_2 system. However, in the previous studies on alizarin on TiO_2 there was a complete shift of the peak position inferred as due to a state formation between Alizarin and the surface Ti of TiO_2. Theoretical calculations reveal that a π-d LMCT is formed on adsorption of alizarin to the surface of TiO_2. The concentration of the dyes were kept below 0.1 mM therefore aggregation of the dyes was not possible. In the present case the surface modifier used was benzophenone which is also neutral; therefore, we do not expect much change due to surface modifier. Therefore the changes observed in the absorption are due to the interaction between the TiO_2 and alizarin molecule only.

3.3.3. Femtosecond Transient Absorption Studies

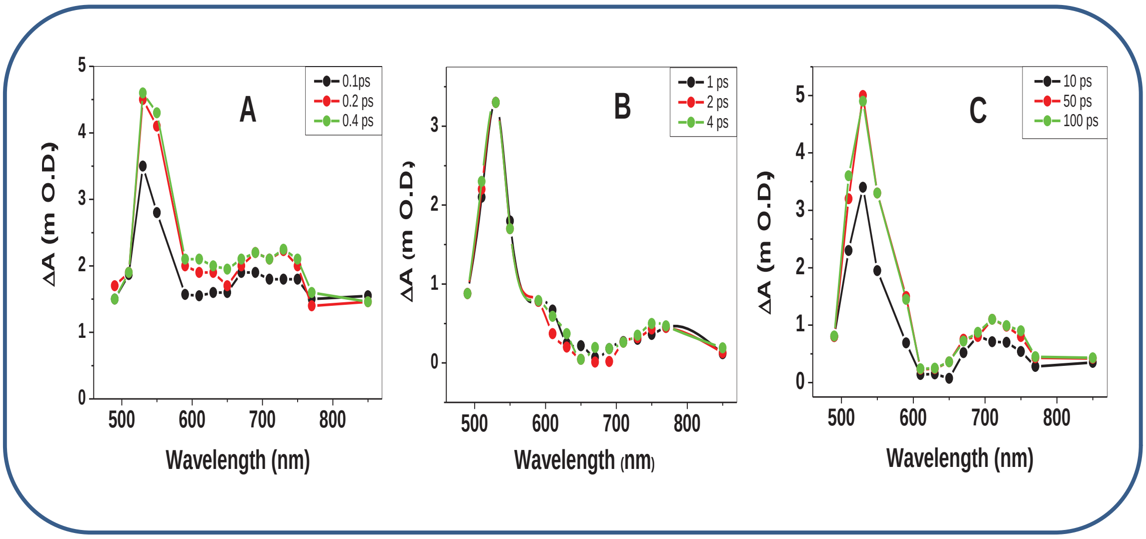

Figure 3.4: Transient absorption spectra of B- TiO_2 -Alizarin in toluene after 400nm excitation.

To gain information of the interfacial electron transfer dynamics between alizarin and TiO_2 we have carried out femtosecond transient absorption study by exciting the samples at 400 nm and following the dynamics using probe light in the wavelength range 470-900 nm. We have shown the time resolved transient absorption spectra in Figure 3.4. The spectrum shows a prominent peak in the region 500-600nm, which can be assigned to the cation radical of alizarin [3.3]. Also the spectrum shows a broad featureless band in the wavelength range 700-900nm which can be attributed to injected electron into the conduction band of TiO_2.

The spectrum has been shown in three parts between 0.1-0.4 ps, 1-4 ps, and 10-100 ps. The spectrum clearly shows that in the time scale up to 0.4 ps, there is an ultrafast increase in the absorption in the entire spectral region indicating the event of ultrafast electron injection. In the time delay upto 1ps we have observed rapid decrease in the absorption signals indicating a very fast back electron transfer reaction. Again from 1-100ps time domain the signal appears to increase, indicating another injection process. It is interesting to observe that there appears multiple injection process in the present case and the time constants of which becomes clear from the decay kinetics at individual wavelengths. It is reported in the literature [3.16] that there is a drastic increase in the molar extinction co-efficient of the dye cation absorption in dye- metal ion system in presence of surfactant assembly.

Dynamics of electron transfer dynamics was carried out by monitoring at 550 nm is represented in Figure 3.5. The kinetics was monitored under low fluence and therefore we do not induce any nonlinearity in the transient absorption studies. The kinetics clearly reveals that there is a pulse width limited electron injection and very fast decay followed by a further injection and a very slow back electron transfer. To ascertain that the initial ultrafast kinetics 0-1.5ps is not due to window/spike we have recorded kinetics with only TiO_2 dissolved in toluene without the dye, there we did not observe any signal. This observation confirmed that the ultrafast components are genuine and not due to experimental artifacts. The kinetic decay trace at 550nm reveals that the injection event is multi-exponential with 3 injection time constants and with two back electron transfer (BET) time constants of 0.4 ps and > 1 ns respectively. The dynamics at 900 nm which monitors the absorption arising due to the conduction band electrons, interestingly reveal the similar dynamics in terms of the time constant albeit with different contribution to various injection times and also the back electron transfer times. This reveals that the dynamics observed at the dye cation maxima and the conduction band electron monitors the same events. The individual contributions to the electron injection time and BET times are given in the Table 3.1.

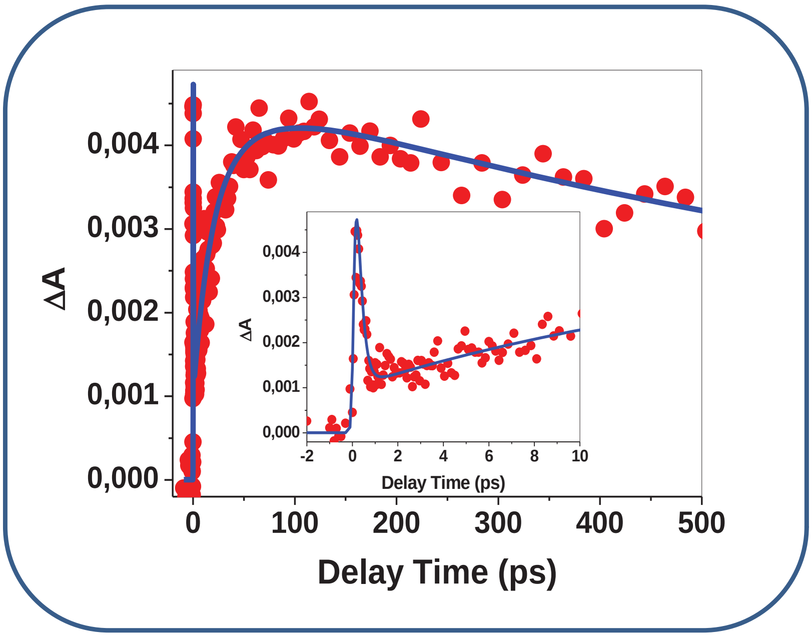

Figure 3.5: Kinetic Decay Traces of B- TiO_2 -Alizarin in toluene after 400nm excitation at λ_{pr}=550nm.

In the present investigation we have observed multi-exponential electron injection in alizarin/TiO_2 system. There could be several reasons to why this can happen. Some of the known possibilities are multilayer formation or aggregation of the dyes on TiO_2 surface. However, in the present investigation we have kept the concentration of alizarin below 10^{-4} M, where possibility of aggregation is very remote. Assuming that the dye molecules are evenly distributed on the surface of TiO_2 we can argue that the concentration is not enough to form aggregate on the dye surface. We have carried out the ultrafast dynamics study on surface modified TiO_2 bulk particle (capped with DBS) and did not observe any multiple injection dynamics where the conditions (concentration of the dye, laser intensity etc) are very similar as compared to the present investigation. The dynamics revealed that the electron injection event in the case of bulk surface modified particle is monophasic and the injection event is pulse width limited which we have already reported in our previous study [3.3]. This proves that the injection dynamics observed in the case is not from a dye aggregate or multilayers of the dye.

Wavelength (nm)	Electron Injection Times			BET Times	
	τ_{inj}^{1},ps (A_1)	τ_{inj}^{2},ps (A_2)	τ_{inj}^{3},ps (A_3)	τ_{BET}^{1},ps (A_2)	τ_{BET}^{2},ps (A_3)
550	0.11 (60%)	17 (27%)	50 (13%)	0.2 (44.7 %)	> 1ns (55.3%)
900	0.08 (85%)	18 (8.5%)	50 (6.5%)	0.2 (80%)	> 1ns (20%)

Table 3.1. Parameters for the multi-exponential Fits to the electron injection and back electron transfer (BET) kinetics of alizarin sensitized B-TiO$_2$ after monitoring both alizarin cation at 550 nm and electron in the conduction band at 900 nm.

The other possibility in the presence case is finite size effect, which could lead to discreteness in the conduction band levels leading to different injection times to different levels within the conduction band. The average size of the particles in the present case is r= ~1.7nm. In case of TiO$_2$, the size of Bohr exciton radius is a range of values. This is due to the fact that the electron and hole effective mass is not known accurately due to unavailability of high quality single crystals.

According to Brus [3.17] the radius r_B of an exciton can be calculated in terms of

$$r_B = \frac{\varepsilon}{m_e^* / m_e} a_0 \qquad 3.\mathbf{1}$$

Now the effective mass of the electron, m^*_e of TiO_2 has been determined by several authors, who report values between 5 and 13 m_e [3.18-3.20]. So the Bohr radius of the exciton as observed previously is in the range of 0.75 nm-1.9 nm. The previous studies [21-22] on TiO_2 colloids revealed size quantization in the particles with diameter of < 3nm. In the present case we observe a clear shift in the absorption onset to blue side for particle sizes <3.8 nm. Our TEM studies show that the nanoparticles formed are of high quality and the absorption spectrum is highly blue shifted. The comparison of the size in the particles used in the present study reveals that the particle size is just within the maximum reported bohr exciton radius of 1.9 nm. Nevertheless the system just within the confinement regime could still exhibit finite size effect. Also in a system of finite size the density of states in the conduction band especially near bottom of the conduction band is discrete due to the fact that the individual crystallite comprises of less number of TiO_2 molecules. Therefore we reason out that in the present case though the size of TiO_2 is below the size quantization regime it could exhibit a multiexponential injection due to the finite nature of the system.

Previously multi-exponential injection has been observed in Ru based MLCT complex-TiO_2 system where the reason for the multiexponential injection was due to singlet and triplet state injection events [3.15, 3.23-3.26]. In the present case a triplet injection is not possible and therefore this as the cause of multiphasic kinetics can be ruled out. Previous studies on the multiexponential injection by Lian et al [3.27] on ZnO/N3 dye reasoned out that although the system used was quantum confined ZnO (r-=~3nm) they have also discussed the possibility of dye aggregation and multilayer formation on the ZnO films. While the same dye gave a pulse width limited injection on TiO_2. This could be due to the fact the studies were conducted on bulk TiO_2. Furthermore, studies on size quantized ZnO with coumarin dyes by Murakoshi et al [3.28] revealed that the injection time based on their fluorescence study at femtosecond resolution was multiexponential, with lifetimes from fs-ns, while injection into TiO_2 occurred in a time of 150 fs. They attributed it to the solvent effect on the interfacial dynamics as they had used a methanol solution for ZnO and aqueous solution for TiO_2. In the present case this could not be the reason as we have observed earlier [3.29] that the injection dynamics using a surface modified normal TiO_2 (synthesized by sol-gel procedure) in toluene and found a pulse width limited injected for the bulk TiO_2-alizarin system. Therefore ruling out all the other causes that could give a multiexponential injection we conclude that in the present case it is due to discreteness in the conduction band. Furthermore, the injection times are large i.e 3 orders of magnitude larger than that of the bulk samples therefore this cannot be explained on the basis of change of solvent.

The literature study on multiexponential injection as mentioned earlier have all been carried out on weak binding dyes. Like Ru-bipyridyl complex N3 and C-343. On the contrary the dye used in the present case is strong binding dye where injection is believed to proceed via adiabatic process [3.4]. Most electron injection event in literature studies could be explained on the basis of classical Marcus relation [3.30]. This equation is strictly valid only for nonadiabatic system, where the injection of the electron from the dye excited state proceeds into the CB via electron tunneling since the interaction between the dye and the semiconductor is weak, whereas in case of an adiabatic electron transfer process the electron transfer proceeds in the same Born-Oppenheimer surface as it moves from the dye to the CB of the semiconductor. The difference in the two majorly lies in the fact that since in nonadiabatic case the electron tunneling occurs, injection times and efficiency of injection depend on the electron coupling between the dye and the semiconductor or in other words the density of states has major effect on the injection time and yield, whereas in the case of an adiabatic electron transfer process it is independent on the density of states. As mentioned earlier, studies [3.4] on alizarin/ TiO_2 system revealed an ultrafast injection with a time of 6 fs. Theoretical studies on Alizarin/ TiO_2[3.31] revealed that the electron injection event in this system could be explained on the basis of adiabatic process. While the molecular dynamics by the same group on the electron injection from alizarin to hydrated Ti^{4+} ion revealed that unlike bulk TiO_2 the injection takes place via nonadiabatic process [3.31]. Duncan et al [3.32] based on their molecular dynamics study concluded that in case of the hydrated Ti^{4+} the non availability of the acceptor levels leads to weaker coupling between the dye and semiconductor. The experimental results by Huber et al [3.4] and molecular dynamics calculations [3.31] suggested that electron injection process in alizarin/ TiO_2 system can be an adiabatic process. Again alizarin molecule strongly coupled with TiO_2 through catecholate moiety which makes a 5 member ring like catechol/TiO_2 complex. Both experimental observation [3.33] and theoretical calculations [3.34-3.35] suggested that on interaction with TiO_2 nanoparticles, catechol molecule a new band originated and a direct charge transfer from catechol to semiconductor surface take place during photoexcitation justifying the process an all adiabatic process. Now by observing the type of binding in alizarin/TiO_2 system and from ultrafast measurements [3.4], it is obvious to think that electron injection process can also be an all adiabatic process. However, recent consolidated theoretical review by Duncan and Prezhdo [3.36] suggests that the story is completely different as compared to catechol/TiO_2 system. Being a larger molecule than catechol, alizarin has extended □-electron system and therefore, smaller excitation energy. Due to the presence of electronegative quinine oxygens lowers the absolute value of the ground and excited states. As a result the optical activity for the charge-transfer excitations in the TiO_2-bound alizarin is significantly smaller than in catechol system, even though the chromophore-semiconductor coupling is exactly the same. As suggested by Duncan and Prezhdo [3.36] that the π* orbital of alizarin, spread over the entire molecule and is much more extended the π * orbital of catechol and therefore mixed less with Ti orbitals and as a result it offers weakly optically active charge-transfer transition bound to Ti through catecholate moiety. So it clearly realized that electron injection process in alizarin/TiO_2 cannot be all adiabatic process. It has been realized that to demonstrate the theoretical prediction it is very important to create a perfect platform where one can observe electron injection process in alirarin/TiO2 system can be mixture of both adiabatic and nonadiabatic process. In the present investigation we have observed that the electron transfer process is multi-exponential and there are longer injection components corresponding to times of 17 ps and 50ps in addition to the ultrafast component (Table 3.1). Therefore the electron transfer event in the present case purely suggests that electron injection in alizarin/TiO_2 cannot be all adiabatic as suggested by Duncan and Prezhdo in their recent review. According to the optical absorption in UV-vis measurements and the size of the particles as measured in high resolution TEM suggest that the present system is a finite one which could in fact lead to a decrease in the density of the acceptor states on the TiO_2 surface and this could give rise to multi-exponential injection. This fact itself is significant in the sense that if one can control the injection into different acceptor levels within the conduction band. The loss of energy via the emission of phonons once the electron is injected into the conduction band gap be drastically reduced leading to an increase in the efficiency of the solar cell.

Additionally, the injection dynamics reveal that although dynamics followed at 550 nm and 900 nm are similar in terms of their lifetimes indicating similar origin to their injection events, the contribution to the individual injection components is considerably different. It can be clearly seen from the kinetics at two wavelengths that the fastest injection components contribution increases when monitored at 900 nm compared to 550 nm. This could be explained on the basis of the fact that while 550 nm wavelength corresponds to the cation absorption which is solely dependent on the concentration of the cation produced, where the molar extinction co-efficient of cation does not change. As a result kinetics at 500 nm gives the true picture of ET dynamics. However, at 900 nm optical density depends on the concentration of electrons in the conductions band and also cross-section (extinction co-efficient) of the injected electron. The cross-section of injected electron depends on the density of states at energetic position of the injected in the CB. So when the injected electron lies in the higher energy level where the levels are more closely packed and has a higher absorption coefficient as compared to the region near the minima of the conduction band. The density of states near the conduction band minima is given by

$$\rho_0(E)dE = \frac{\left(2m^*\right)^{3/2}}{2\pi^2\hbar^3}\sqrt{E}dE \qquad 3.\mathbf{2}$$

In the above equation, m^* is the effective mass of the electron and the rest of the symbols have their usual meaning [3.15]. The above expression clearly shows that the density of states nears the conduction band minima increase as we move higher in energy.

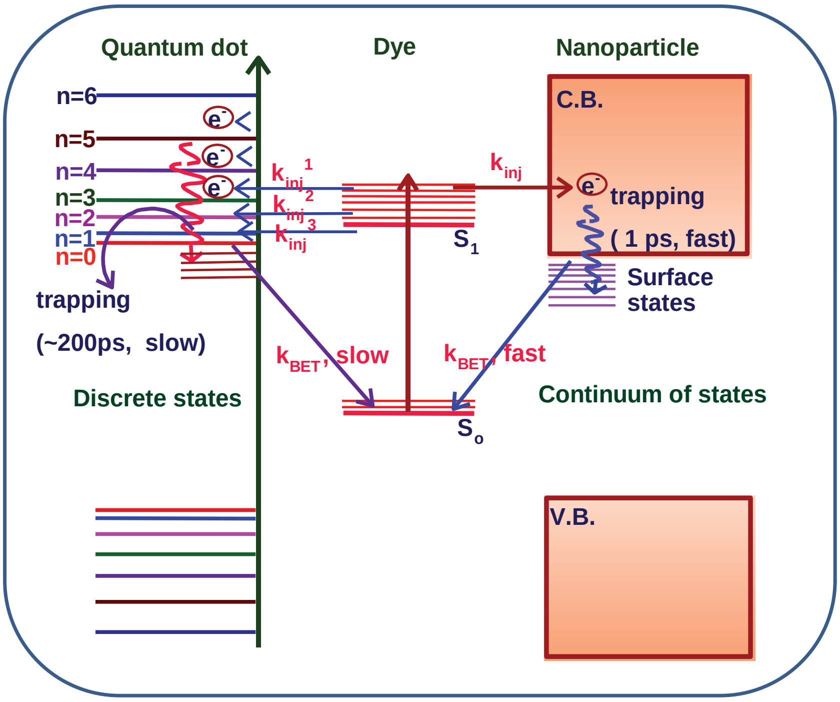
Quantum dot
Dye
Nanoparticle
n=6
n=5
n=4
n=3
n=2
n=1
n=0
e-
k inj 1
k inj 2
k inj 3
k inj
C.B.
trapping
(1 ps, fast)
Surface states
S1
trapping
(~200ps, slow)
Discrete states
k BET, slow
k BET, fast
Continuum of states
So
V.B.

Scheme 3.1. Schematic Diagram representing the electron transfer dynamics in both TiO_2 nanoparticle and TiO_2 quantum dot sensitized by alizarin in toluene. It shows multiexponential injection and slow back ET on quantum dot surface and single exponential injection and faster back ET on nanoparticle surface.

Furthermore, in a finite system this is further accentuated due to introduction of discreteness. The variation in the cross section of the injected electron in the CB affects the kinetics monitored in the near IR region. The decrease in the density of states also gives rise to a slower injection time for the injection from near the bottom of the conduction band compared to the hot electron injection. From the above argument we can build a general picture of the injection event assigning the fast lifetime to injection from higher vibrational FC states of the dye, immediately after excitation which happens in hundreds of fs the next injection event happens in ps time scales. The two ps components (17 ps and 50 ps) could be due to difference in the electron coupling of the dyes to the TiO_2 surface. The representation of the injection event based on the above conclusion is given in Scheme 3.1.

While the study of injection dynamics gave us the information on the levels involved and the type of electron transfer that happened. The BET study would give us a plethora of information on how fast the electron returns back to the HOMO of the dye cation. This is very important factor controlling the efficiency of a solar cell, the greater BET time, the better efficiency. The BET times are given in the Table 3.1. The BET components show a very fast component 0.2 ps and a slow component of >1 ns. The fast component can be attributed to the charge recombination dynamics of hot injected electron which is been injected into the higher quantized states and which is very strongly coupled with the parent cation. However, the second component is found to be > 1 ns which is much slow compared to previous result [3.28] which had a BET times of 7 ps and >400 ps for bulk TiO_2 and 35ps and >400ps for surface modified TiO_2. This is a very interesting behavior could be a clear evidence of Marcus inversion region where the increase in the free energy arises due to the increase in the CB position due to size quantization. The explanation of the above observation can be given on the basis of Marcus theory. The BET in a semiconductor and an adsorbate can be given by the below given expression

$$k_{BET} = \left(\frac{4\pi^2}{h}\right)[V]^2\left(\frac{1}{\sqrt{4\pi\Lambda kT}}\right)\exp\left\{-\frac{(\Delta G^0+\Lambda)^2}{4\Lambda kT}\right\} \qquad 3.\mathbf{3}$$

In equation 3.3, BET rate constant (k_{BET}) depends on the coupling element (H_{AB}), the overall free energy of reaction ($\Delta G^0 = E_{\mathrm{C}} - E_{\mathrm{S/S+}}$), the potentials of electrons in the conduction band of the semiconductor (E_{C} = -0.49 V) and the redox potential of the adsorbed dye ($E_{\mathrm{S/S+}}$) (Scheme 3.1). The electronic coupling remains the same therefore the BET times are mainly governed by the free energy and the reorganization energy. Since we are comparing similar system the reorganization energy is similar there we come to the conclusion that the free energy change is the only factor determining BET rate. This can be explained only on the basis of size quantization. In a size quantized system not only the conduction levels become discrete, the conduction band also moves upward which effectively increases the free energy $(-\Delta G^0)$ of charge recombination reaction. Again due to the discrete nature of the different energy levels of the conduction band the carrier relaxation dynamics of injected electron will be much slower as compared to the bulk system. As a result the energy level of the injected electron lies at much higher level as compared to the bulk one. So for a given injected electron and parent cation pair free energy of charge recombination reaction will be much higher as compared to the bulk system. Higher free energy of charge recombination falls in the Marcus inversion regime, which reduces rate the BET of reaction. These observations further accentuate the evidence of the injection dynamics result which essentially concluded that the injection dynamics could only be accounted on the basis of the finite size effects.

3. 4. Conclusions

In conclusion, ultrafast transient absorption studies have been carried out to throw light on the interfacial electron transfer dynamics in alizarin/TiO_2 system. Optical absorption spectra showed the appearance of shoulder on the red side of the main alizarin absorption indicating a charge transferred state. The electron transfer dynamics was compared with alizarin/bulk TiO_2 surface modified particle. The injection dynamics revealed multi-exponential injection indicating injection into different discrete levels in CB. The multi-exponential injection indicates a nonadiabatic injection unlike the conclusion of the previous study. The aggregation and the multilayer formation as the cause of the multi-exponential injection has been ruled out due to dilute solution of alizarin that has been used in the present study. Based on the injection dynamics study we have arrived at the model for the injection into the semiconductor considering the discreteness in the CB. For the sake of comparison we compared the present results with that of bulk TiO_2/alizarin, this revealed a monoexponential pulse width limited injection. Furthermore, the BET dynamics revealed that it is considerably slower on the B-TiO_2 compared to that of bulk TiO_2 system. This was explained within the framework of Marcus inversion, where an increase free energy due to upward shift of the conduction band levels and also its discrete nature which in turn slow down the carrier relaxation time and eventually increase the lifetime of the electron at higher energy level, and finally led to an decrease in the BET. These observations are significant as previously it was believed that in a strong coupling dye the ET takes place via adiabatic route, but the present set of results seem to indicate that ET event is nonadiabatic based on the multiexponential injection. Based on this observation we can also predict that in a relatively weaker binding dye the injection time will be still slower and the BET rate will be more slow, which has tremendous implication for the solar cell application because the organic dye have gone out of favor among the scientists working on the solar cell because they have a very fast BET rate as compared to Ru-polypyridyl complexes. This study proves that this problem can be solved using ultrasmall TiO_2. Alternately one can design solar cells with ultrasmall TiO_2 and Ru based sensitizer to further improve the efficiency from the present best efficiency of 10%.

3.5. References

1. O’Regan, B.; Graetzel, M. *Nature* **1991**, *353*, 737.

2. Nazeeruddin, M. K.; Kay, A.; Rodicio, I.; Humphrybaker, R.; Muller, E. Liska, P. Vlachapoulos, N.; Graetzel, M. *J. Am. Chem. Soc.* **1993**, 115, 6382.
3. Rehm, J. M.; Mclendon, G.L.; Nagasawa, Y.; Yoshihara, K. ; Moser, J.E.; Graetzel, M. *J. Phys. Chem. B*. **1996**, 100, 9577.
4. Huber, R.; Moser, J.-E.; Graetzel, M.; Wachtveitl, J. *J. Phys. Chem. B*. **2002**, 106, 6494.
5. Martini, I.; Hodak, J. H.; Hartland, G. V.; Kamat, P. V. *J. Chem. Phys.* **1997**, *107*, 8064.
6. Martini, I.; Hodak, J. H.; Hartland, G. V. *J. Phys. Chem. B* **1998**, *102*, 9508.
7. Hilgendroff, M.; Sundstrom, V. *J. Phys. Chem. B* **1998**, *102*, 10505.
8. Ramakrishna, G.; Das, A.; Ghosh, H. N. *Langmuir* **2004**, *20*, 1430.
9. Benko, G.; Kallionen, J.; Korppi-Tommola, J. E. I.; Yartsev, A.P.; Sundstrom, V. *J. Am. Chem. Soc.* **2001**, *124*, 489.
10. Moser, J.; Graetzel, M. *J. Am. Chem. Soc.* **1984**, *106*, 6557.
11. Kamat, P. V.; Fox, M. A. *Chem. Phys. Lett.* **1983**, *102*, 379.
12. Eichberger, R.; Willig, F. *Chem. Phys*. **1990**, *141*, 159.
13. Lanzafame, J. M.; Miller, R. D. J.; Muenter, A. A.; Parkinson, B. A. *J. Phys. Chem.* **1992**, *96*, 2820.
14. Huber, R.; Sebastian, S.; Moser, J. E.; Graetzel, M.; Wachtveitl, J. *J. Phys. Chem. B*. **2000**, 104, 8995.
15. Ai, X.; Anderson.; N. A.; Guo, J.; Lian, T. *J. Phys. Chem.* **1999**, 103, 6643.
16. W.L. Hinze, Solution Chemistry of Surfactant, K.L. Mittal (ed) vol 1, pp 79-127. Plenum Press, New York, 1979.

17. L. E. Brus, *J. Phys. Chem.* 1986, **90**, 2555.

18. Acket, *G.* A.; Volger, J. *Physica (Amsterdam)* **1966,** *32,* 1680.

19. Pascual, J.; Camassel, J.; Mathieu, H. *Phys. Rev. B Condem. Matter* **1978,** *18,* 5606.

20. Agekyan, V. T.; Berezhnaya, A. A,; Lutsenko, V. V.; Stepanov. ***Y.*** A. *Sov. Phys. Solid State* **1980,** *22,* 6.

21. Serpone, N.; Lawless, D.; Khairutdinov, R., *J. Phys. Chem,* **1995**, 99, 16646.

22. Kormann, C.; Bahnemann, D. W.; Hoffmann, M.R, *J. Phys. Chem.* **1988**, 92, 5196.

23. Benko, G.; Myllyperkio, P.; Pan, J.; Yartsev, A. P.; Sundstrom, V. *J. Am Chem. Soc.* **2003**, 125, 1118.

24. Benko, G.; Kallioinen, J.; Myllyperkio, P.; Trif, F.; Korppi- Tommola, J. E. I.; Yartsev, A. P.; Sundstrom, V. *J. Phys. Chem.B* **2004**, 108, 2862.

25. Kallioinen, J.; Benko, G.; Sundstrom, V.; Korppi- Tommola, J. E. I.; Yartsev, A. P. *J. Phys. Chem.B* **2002**, 106, 4396.

26. Kuciauskas, D.; Monat, J. E.; Villahermosa, R.; Gray, H. B.; Lewis, N. S.; McCusker, J. K. *J. Phys. Chem. B* **2002**, 106, 9347.

27. Asbury, J. B.; Wang. Y. Q.; Lian. T. *J. Phys. Chem.* **1999**, 103, 6643.

28. Murakoshi, K.; Yanagida, S.; Capel, M.; Castner, J. E. W. *Interfacial Electron Transfer dynamics ofPhotosensitised Zinc Oxide Nanoclusters*; ACS Symposium Series 679, The American Chemical Society: Washington DC, **1997**.

29. Ramakrishna, G.; Singh, A. K.; Palit, D. K.; Ghosh, H. N. *J. Phys. Chem. B.* **2004**, 108, 1701.

30. Marcus, R. A.; Sutin, N. *Biochim. Biophys. Acta.* **1985**, 811, 265.

31. Duncan, W. R.; Stier, W. M.; Prezhdo, O. V. *J. Am Chem. Soc.* **2005**, 127, 7941.

32. Duncan, W. R; Prezhdo, O. V. *J. Phys Chem.* **2005**, 109, 17998.

33. Wang, Y.; Hang, K.; Anderson, N. A.; Lian, T. *J. Phys. Chem. B,* **2003,** *107*, 9434.

34. Rego L. G. C.; Batista V. S. *J. Am. Chem. Soc*., **2003**, *125*, 7989.

35. Duncan, W. R.; Prezhdo, O. V. *J. Phys. Chem. B,* **2005**, *109*, 365.

36. Duncan, W. R.; Prezhdo, O. V. *Annu. Rev. Phys. Chem.* **2007,** *58*, 143.

Chapter 4

CHAPTER 4

Effect of Size Quantization on Charge Carrier Dynamics in Thiol Capped CdTe Quantum Dots

4.1. Introduction:

Semiconductor quantum dots (QD) are quasi zero dimensional materials which have gained lot of research interest in last decade due to its exciting size and shape dependent properties [4.1-4.3]. A lot of efforts have been taken to synthesize QDs with different band gap which can be easily tuned by changing their size and shape. These materials are highly luminescent with narrow emission line width which has huge application in fabricating optoelectronic devices, biological application etc. Their novel properties like discrete optical spectra, size dependent optical behavior, increase in PL quantum yield has led to their flexible uses in several devices [4.2]. These developments have led to involvement of several research groups working on the ability to control the growth, size, phase of the nanocrystals by chemical methods [4.3]. Nevertheless, the carrier dynamics of the excited states in semiconductor NPs are still being actively investigated.

Due to efficient coupling of the charge carriers with the polarity of the lattice in bulk II-VI semiconductors, the relaxation rate of the charge carriers are very fast and the conduction band gets populated rapidly [4.4]. However relaxation changes dramatically in case of quantum dots. Discrete energy levels lead to “phonon bottleneck” [4.5] in the relaxation dynamics of QD. Again due smaller size, majority of the atoms lies on the surface of the QDs. As a result surface atom or in other word surface states of QD play a major role in the relaxation dynamics. Surface imperfections leads defect states on the surface which leads to additional competing relaxation pathways by trapping into surface defect sites and eventually can accelerate the depopulation of the band edge. Furthermore, due to smaller size, coupling between electron and hole wave function is much higher which leads to faster relaxation rate. For all the above reasons it is very difficult to predict relaxation behavior of QD particle. Therefore ultrafast spectroscopic techniques would enable the study of complex behavior of the carrier relaxation dynamics in QDs, where many early events take place in ultrafast time scale.

Transient absorption (TA) experiments using time-resolved pump-probe spectroscopy are a perfect tool to investigate the ultrafast electron-hole dynamics in semiconductor nanoparticles. Many time-resolved investigations on the electron-hole dynamics in colloidal II-VI semiconductor nanoparticles are found in the literature. Previously TA technique has been used in the extensive study of charge carrier dynamics in CdSe quantum dot. Guyot-Sionnest and co-workers [4.6] demonstrated that the dynamic behavior of excited electrons could be monitored by using a mid-IR probe beam, in contrast to the complex relaxation behaviors in the visible probe measurements due to the contributions from both electrons and holes, as has been reported [4.6]. These studies [4.6] have led to observation of novel physics in play in QD systems. Several studies have demonstrated the influence of surface ligands in the dynamics of the charge carriers by trapping. The understanding from these studies has led to achievement of nanosecond cooling times in multiple shells CdSe QD [4.7]. Extensive Studies [4.6, 4.8] have suggested phonon bottleneck effects, nonadiabatic interaction, and Auger mediated process in the relaxation of electron and holes in CdSe QDs which is impossible in bulk systems. Formation of multiexcitons is another novel observation that has been confirmed [4.2, 4.9]. These studies suggest how different these systems are compared to that of the bulk systems. While studies carried out have been extensive, but much of the literature have concentrated on carrier dynamics in CdSe QDs. It is important to study the dynamics in further systems as they may present some novel phenomena like Multi Exciton Generation in Lead Salt QD [4.9]. Prior studies on CdTe QDs by fluorescence upconversion [4.10], pump probe spectroscopy [4.11], Degenerate Four Wave Mixing [4. 12] on the dynamics had provided valuable information on the dynamics of carriers or dephasing,

In the present chapter, we investigate charge carrier dynamics in CdTe by ultrafast TA (Transient Absorption) technique. The samples have been synthesized by standard methods as described in experimental section. The samples were characterized by UV-Visible Absorption technique, TEM. The samples synthesized by this method are spherical so they show a 3-D confinement. The TA technique is used to study how size quantization and surface influences the relaxation dynamics in QDs.

4.2. Experimental Section:

4.2.1. Materials:

Cadmium Chloride (≥99%), Te Powder (≥98), 1-Mercaptopropionic acid (≥99%), $NaBH_4$ and Benzoquinone were purchased from Aldrich and used it as received without further purification. Isopropyl alcohol was used as received from S. D. Fine chemicals. N-Butyl Amine and Benzoquinone were from Aldrich.

4.2.2. Synthesis:

The CdTe QDs were prepared by water soluble methods as reported in the literature [4.13]. Briefly, 2.35mmol of $Cd(NO_3)_2$ was added to nanopure water to this mercaptopropionic acid (MPA) with the mole ratio of MPA: Cd=2.4:1. The pH of the above solution was raised to 9-10 and was purged with N_2. The tellurium precursor NaHTe, was prepared by reaction between $NaBH_4$ and tellurium powder in N_2 purged water at 0°C for 8 hr. Part of this solution was added to the Cd precursor solution with the ratio of Cd:Te=1:0.5. The above solution was refluxed and aliquots of the solution were removed at various times to obtain quantum dots of different sizes. The aliquots were concentrated at lower pressure by a Butchi rotavapour to 1/3rd of the original volume and isopropyl alcohol was added to the concentrated solution to precipitate the quantum dots. The collected quantum dots were re-dissolved in nanopure water and precipitated with isopropyl alcohol, this process was repeated 3 times to remove the precursors and clean the quantum dots.

The concentration of CdTe samples was ~10^{-5} M as calculated from extinction coefficient from Peng et al [15] at the exciton peak position. The $\langle N \rangle = j\sigma$ value was maintained at ~0.1excitons per particle to avoid multi particle relaxation processes like Auger process involving 3 charge carriers. Four CdTe samples were prepared and are abelled according to increasing size CdTe1 (2.6nm), CdTe2 (3.3nm), CdTe3 (3.5nm) and CdTe4 (3.8nm).

4.3. Results & Discussion:

4.3.1. Steady State Absorption Studies

To investigate charge carrier dynamics of different sized of CdTe QD we have synthesized particles of different diameters. Figure 4.1 shows optical absorption spectra of CdTe QD which clearly demonstrate different exciton bands in the spectral region. Particle sizes were calculated from the sizing curves as demonstrated by Peng et al [4.15] considering spherical nature of the particles. The particle size of CdTe QD determined to be 3.5 nm which is much smaller than the Bohr radius of CdTe (r_B^{CdTe} ~6.5 nm). We have synthesized different sizes of QD particles and the optical spectra are shown in supporting information, which clearly demonstrate that with increasing particle size the exciton band moves to the red region of the spectra.

The discrete features at 480 nm, 530 nm and 590 nm in the absorption spectrum in Figure 4.1 can be attributed to different exciton states of quantum dot and are labeled according to usual nomenclature [4.8]. The lowest exciton states corresponds to the transition between two different states conduction band and valence band, where electronic state ($1S_e$) in the conduction band is same, however the valence band states of holes are different ($1S_{3/2}$ and $2S_{3/2}$). The higher exciton state is the $1P_{3/2}$-$1P_e$ where both the electron and the hole is in state with l=1. The peak at 590 nm and 530 nm corresponds to $1S_{3/2}$-$1S_e$ and $2S_{3/2}$-$1S_e$ transition, where as the high energy peak at 480 nm can be attributed to $1P_{3/2}$-$1P_e$. Particularly striking is the energy difference between the lowest states which is much higher compared to thermal energy of ~25meV, this would lead to a much slower relaxation from the higher hole state to lower hole state. In CdSe the lowest two hole states are convoluted, leading to considerable overlap between lowest hole states and therefore similar dynamical behavior for these states.

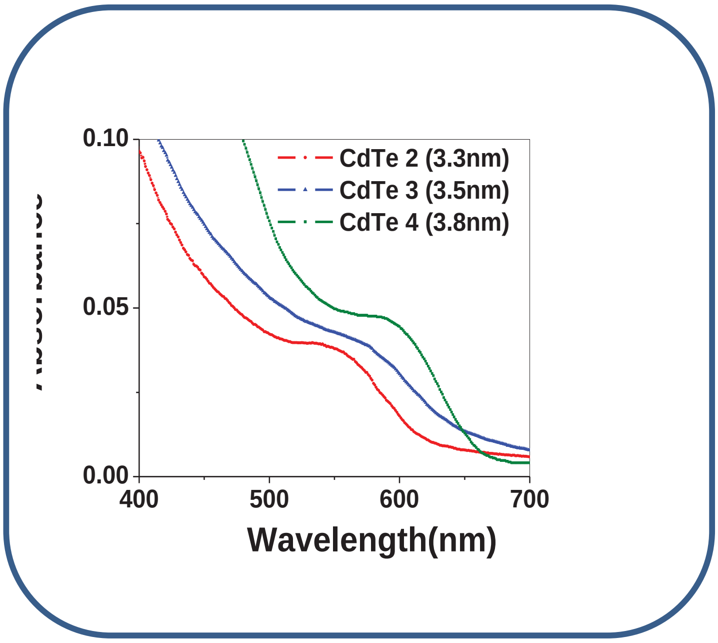

Fig.4.1. Optical Absorption Spectrum of CdTe Samples.

The Samples are numbered in the increasing order of sizes.

4.3.2. Femtosecond Transient Absorption Studies

To understand charge carrier relaxation and charge recombination dynamics in CdTe QD, we have carried out femtosecond transient absorption studies detecting the transients in the visible –near IR region after exciting at 400 nm laser light. Figure 4.2 shows the transient absorption spectra of phtoexcited QDs in different time delay, which comprises two negative absorption bands peaking at 530 nm and 590 nm and a broad positive absorption band in 670 nm – 850 nm region. It is interesting to see that both the bleach peak appears at 530 and 590 nm which exactly matched with the excitonic peaks appeared in the steady state absorption of CdTe QD (Figure 4.1). This indicates that the transitions are state filling because state filling transitions affect transitions observed in linear absorption spectrum.

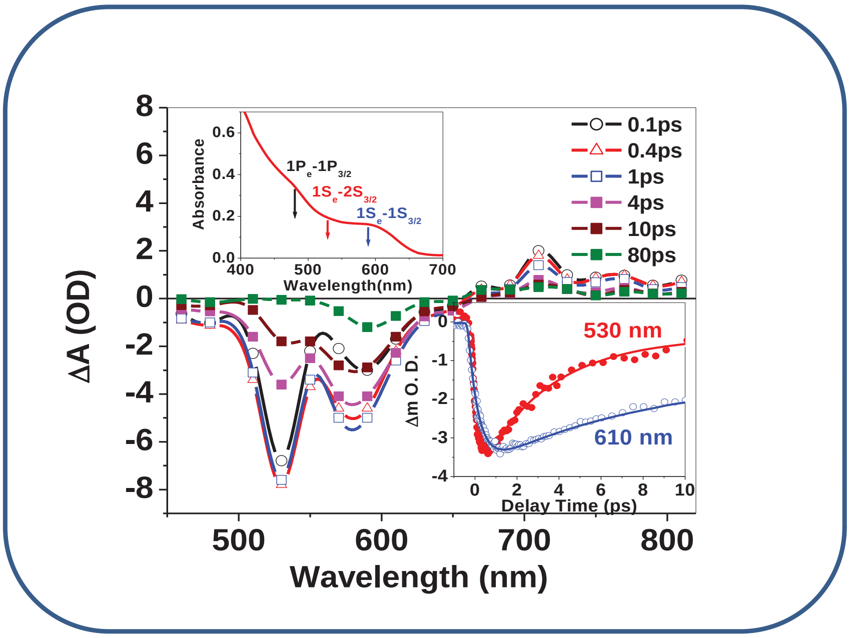

Figure 4.2: Transient absorption spectra of CdTe quantum dot (QD) at different time delay after excitation at 400 nm laser light. Inset: Kinetic traces monitored at 530nm (Figure 3 a) and at 610nm (Figure 3 b) and optical absorption spectra for the sample.

In the present investigation N<0.1, so complexity in the dynamics due to bi-exciton and stark effect can be ruled out. It is interesting to see that the bleach intensity at an early time scale (100 fs) has a maximum at 530 nm and at 590 nm it appears relatively smaller. However with time the peak at 530 nm recovers much faster as compared 590 nm. It is clearly seen that for longer time (80 ps) the bleach at 530 nm is completely disappears however at 590 nm it still exist. We have shown the kinetic traces for both 530 nm and 590 nm wavelengths in Figure

4.2 inset. The kinetic traces at 530 nm and 590 nm can be fitted with growth time constants of 150 fs and 500 fs respectively. It is known from the literature [4.2] that appearance of bleach on photoexcitation of QD is due to the population of charge carriers at particular quantized state. So the appearance and disappearance of the bleach is directly related to the population of charge carrier in that particular quantized state. The bleach appears due to the state filling transitions of both electron and hole, however contribution of electrons to bleach are significant mainly for two reasons (i) valence band degeneracy at Γ-point and (ii) large difference between electron and hole effective masses (m_h/m_e~4 for CdTe) giving rise to delocalization of hole states compared to electron levels in the conduction band. In the present investigation we can observe that the bleach intensity at early time scale at 530 nm is much higher as compared to 590 nm, where the ratio of the bleach intensity doesn't match with the linear absorption spectra as we observe in Figure 2. Earlier Peyghambarian et al [4.16] have demonstrated state filling transition in CdTe QD by selective excitation of different excitons. They attributed the large transient absorption for $2S_{3/2}$-$1S_{3/2}$ due to variation in the selection rules for absorption. Similarly in the present investigation we are attributing the large bleach associated with $2S_{3/2}$ hole states to significant change in the wave functions of the electron and hole due to electron hole pairs created by the pump pulse leading to change in the selection rules. The separation energy between two quantized valance state i.e. $2S_{3/2}$ and $1S_{3/2}$ could lead to much slower relaxation to lower exciton states which lead to piling up excitons in $2S_{3/2}$ state. As a result we can observe larger bleach in early time scale at 530 nm (associated with $2S_{3/2}$ hole state). So the growth time constant 150 fs at 530 nm and 500 fs at 610 nm can be attributed to cooling dynamics of second and first excitonic state respectively. The recovery kinetics at 530 nm can be fitted with time constants of 3.2ps (~90%) which can be attributed to de-population time constant of second exciton. The recovery kinetics at 610 nm can be fitted with time constants (7ps, 35ps, >400ps) attributed to de-population time constant of second exciton which basically the charge recombination dynamics between electron and hole pairs.

We have observed that on excitation of CdTe QD, bleach appears at the excitonic positions. By monitoring the excited state dynamics at those excitonic wavelengths, we get information of both cooling and recombination dynamics of the charge carriers. It is reported in the literature that on size quantization both valence and conduction band becomes discrete and shows interesting properties like slow carrier cooling dynamics in QD material as compared to that in bulk. The cooling based on Frohlich interaction by electron-LO phonon interaction increases with respect to radius because in smaller quantum dot the energy separation between the exciton states are much larger as compared to larger quantum dot due to increase in confinement energy as given below

$$\tau = \omega_{LO}^{-1} \exp(\Delta E/k_B T) \qquad (4.1)$$

Where ΔE is the energy difference between the exciton states and ω_{LO} is the energy of LO phonon [4.2]. Typically in a QD this is expected to give a cooling time of several hundreds of picoseconds. However in our investigation we have observed that the cooling time is sub 1 ps for the charge carriers. Again according to the above equation, cooling time of QD should increases with decreasing the size of the QD. In the present investigation we have also synthesized different sizes QDs and carried out transient absorption studies to monitor the cooling time for different size particles by following the bleach at the excitonic wavelengths. Panel A Figure 4.3 shows the kinetic traces (bleach kinetics) at $1S_{3/2}$-$1S_e$ excitonic position for different QD sizes namely 3.3 nm, 3.5 nm and 3.8 nm. It is very interesting to see that growth of the bleach kinetics (attributed to cooling dynamics) changes from 100 fs, to 250 fs to 500 fs for 3.3 nm, 3.5 nm and 3.8 nm QD particles respectively. We have plotted cooling time vs size of the particles in panel B of Figure 3, which shows nonlinear increase in the cooling times with the size of QD. From the above experimental results we can observe that cooling mechanism doesn't follow the above equation 4.1, on the contrary it gives exactly opposite trend with particle size. Therefore the involvement of other cooling mechanism might be have a role in the present case. It has been observed in earlier investigations[4.2, 4.6] carrier cooling can take place by e-h energy transfer, surface defect or non adiabatic ligand mediated cooling. If cooling dynamics in CdTe QD takes place through e-h energy transfer or non adiabatic ligand mediated cooling, then the decay of the $2S_{3/2}$(h) hole state (recovery of 530 nm bleach) would exactly match with growth of $1S_{3/2}$(h) hole state (growth of 610 nm bleach). Or in other words decay time of the higher hole state ($2S_{3/2}$-$1S_e$) should be equal to the bleach rise time of lower hole state ($1S_{3/2}$-$1S_e$), i.e. they would show complementary dynamics. However we can see from the inset of Figure 4.2 that the bleach formation time at 610 nm ($1S_{3/2}$-$1S_e$) is 0.5ps does not match with the decay kinetics at 530 nm which has been attributed to the relaxation time of higher exciton state $2S_{3/2}$(h)-1S(e). The kinetics at 530 nm can be fitted by 3.2ps(88%) & ~70ps (12%). So from our experimental observation we can tell that the relaxation from $2S_{3/2}$ to $1S_{3/2}$ hole state is not through e-h energy transfer or nonadiabatic relaxation processes. Another possibility is that the population of lowest exciton might takes place directly from the highest excitonic state ($1P_{3/2}$-$1P_e$) which was populated initially on 400 nm laser excitation. The relaxation from this exciton state may proceed via an Auger process.

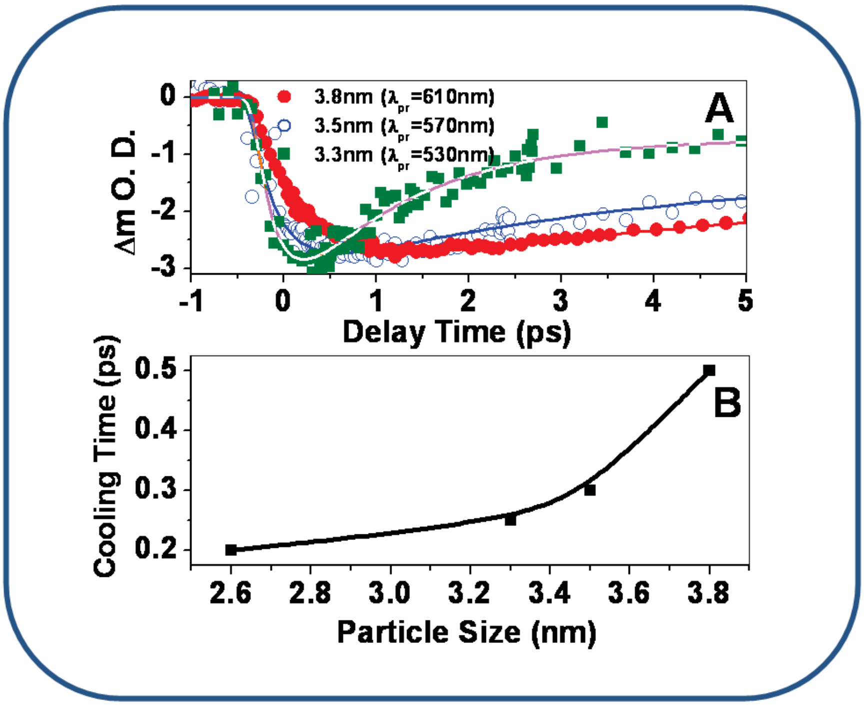

Figure 3: Panel A: Normalized kinetic traces photoexcited CdTe for different particle sizes at 610 nm (1S exciton position). Panel B: Plot of cooling time (growth kinetics at 1S exciton) vs particle size showing non-linear increment.

To confirm the involvement of Auger mediated cooling processes we have carried quenching studies where the quenchers can selectively accept electrons or holes and then find out the effect of cooling dynamics of the lowest excitonic ($1S_{3/2}$-$1S_e$) state. The quenchers can decouple electrons or holes selectively which eventually hinders the energy transfer from the electron to the hole. In the present studies we have used benzoquinone (BQ) as electron quencher and n-butyl amine (BA) as hole quencher. Figure 4 show the kinetic trace at 1S exciton position (monitored at 610 nm) of CdTe QD in absence of any quencher (Figure 4.4a), in presence of electron quencher (BQ) (Figure 4.4b) and in presence of hole quencher (BA) (Figure 4.4c). In presence of BQ, it is expected that hot electron will be quenched. In previous section we have discussed the growth of the bleach kinetics of pure CdTe QD at 610 nm shown in inset of Figure 4.2 and also depicted in Figure 4.4a can be fitted with a growth kinetics can be fitted with time constant of 500 fs. However the kinetic trace at 610 nm in presence of BQ (Inset, Figure 4.4b) can be fitted with a growth time of 200 fs. Here BQ is expected to separate out the hot electrons from the conduction band so it is expected that the growth of bleach signal will be specifically monitor the cooling dynamics of the hot holes. Here in presence of BQ the electrons will be de-coupled from the holes, as a result we will be monitoring only hole dynamics.

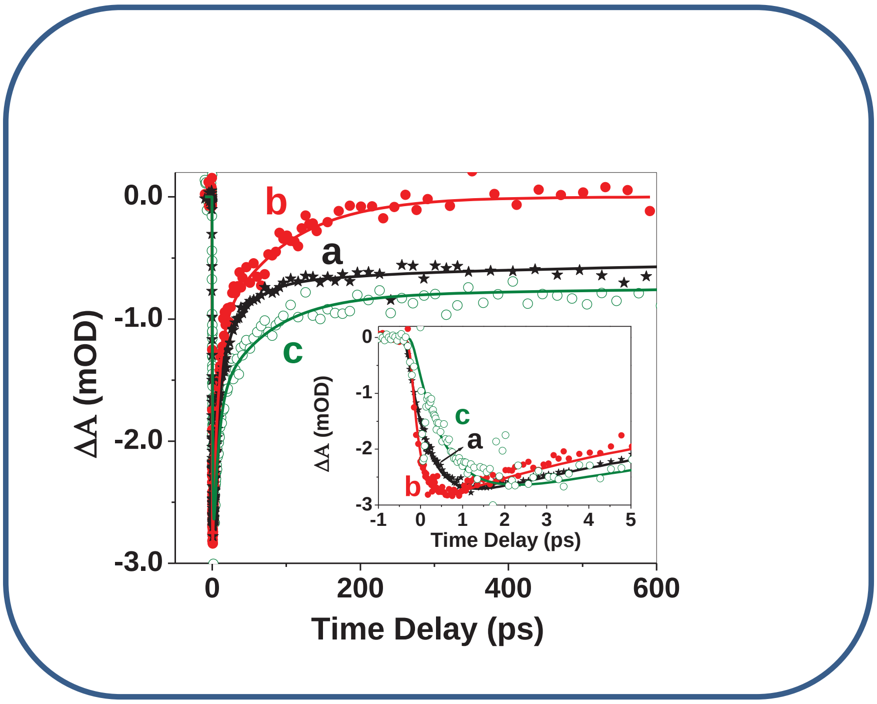

Figure 4.4: Normalized kinetic traces of a) CdTe, b) CdTe with BQ and c) CdTe with BA at 610 nm (1S exciton position). Inset: Same kinetic traces at shorter time scale.

Figure 4.4c is the bleach kinetics of CdTe at 610 nm in presence of hole quencher (BA) can be fitted with 700 fs growth kinetics. This time constant can be attributed to cooling dynamics of hot electron. The presence of a hole quencher decouples the electron from the hole as the hole is localized on the surface therefore the interaction between the electron and the hole is low. Therefore the cooling dynamics exclusively contains information about the electron relaxation. It is interesting to see that the cooling dynamics of hole in the valence band is faster as compared to electron in the conduction band. Density of states in valence band is much higher as compared to the conduction band and also the energy gap between two quantized states in the valence band is much lower as compared to the energy gap between two quantized states in the conduction band. Therefore as expected the electron cooling takes place at a slower rate.

Figure 4.4 also depicted the bleach recovery kinetics at first exciton position (at 610 nm) from which we can estimate the charge recombination (CR) dynamics between the charge carriers. The bleach recovery kinetics of CdTe QD without any quenchers (Figure 4a, Panel A) can be fitted tri-exponentially with time constants of τ_1 = 7ps (53%), τ_2 = 35 ps (25%) and τ_3 => 400 ps (22%). It is interesting to see that majority of the charge carriers recombined with in 100 ps. This might be due to the QDs are smaller in dimension so it is expected that there will be reasonable wave function overlap between photo-generated electrons and holes. The longer components can be attributed to the CR dynamics between trapped charge carriers (both trapped electron and trapped holes). However we can see the bleach recovers at 610 nm much faster in presence of electron quencher (BQ) as shown in Figure 4.4 b. The kinetic decay trace can be fitted tri-exponentially with time constants τ_1 = 5.5ps (56.5%), τ_2=60ps (38.7%) and τ_3 = >400 ps (4.8%). It was shown before by Burda et al [4.17] that the addition of benzoquinone (BQ) to a colloidal solution of CdSe rapidly removes the electrons from the conduction band of the photoexcited NP and forms a short lived charge transfer complex which decays mono-exponentially with a lifetime of 2.7 ps. As a result the repopulation of the ground state depends on the lifetime of the $NP^{+}BQ^{-}$ charge transfer (CT) complex. Since the lifetime of the CT state is shorter, the excited-state lifetime of the NP-BQ conjugate is actually drastically shorter than the one of CdSe NP themselves. In the present investigation also we have observed recombination dynamics of CdTe QD is much faster in precedence of BQ (Figure 4.4b) as compared to without any quencher (Figure 4.4a). Now let us discuss bleach recovery kinetics in presence of hole quencher (BA) which we have shown in Figure 4 c. It is interesting to see that the bleach recovers at slower rate as compared to Figure 4a. The recovery kinetics can be fitted multi-exponentially with time constants of τ_1 = 8ps (44.5%), τ_2 = 60 ps (28.6%) and τ_3 => 400 ps (26.9%). Earlier El Sayed et al [4.18] have reported that BA influences the dynamics by modifying the surface states of the QD. In the present case we find that the cooling dynamics is affected on addition of BA therefore we can safely conclude that the hole is separated from the valence band before cooling takes place, therefore BA acts as a hole quencher. This in turn affects the charge recombination of QD. We can observe clearly that the charge recombination slows down in presence of BA, or in other word the excited state lifetime of CdTe NPs is considerably longer when BA was added.

So far in earlier paragraphs we were discussing about the cooling and recombination dynamics of the charge carriers, however from the application point of view trapping dynamics of the charge carriers has considerable influence on the functioning of various devices based on QDs. To understand the trapping dynamics in Figure 4.5 we have plotted the kinetic decay trace at 1000 nm and reverse bleach recovery kinetics of 610 nm. The reverse bleach recovery kinetics at 610 nm (Figure 5a), which has been fitted with time constants of τ_1 = 7ps (53%), τ_2 = 35 ps (25%) and τ_3 => 400 ps (22%) gives an idea of charge recombination dynamics of both hot and trapped charge carriers. In Figure 2 we can observe a positive absorption beyond 670 nm after photoexcitation. This wavelength region (670 nm -1000 nm) is suitable for monitoring the trapping dynamics of the charge carriers as it does not overlap with excitonic position of the QDs. The kinetic decay trace at 1000 nm which is attributed to positive absorption of the charge carriers (both electrons and holes) can be fitted multi-exponentially with time constants τ_1 = 1ps (72.5%), τ_2 = 25 ps (22%) and τ_3 > 400 ps (5.5)%. The kinetic decay trace at 1000 nm gives us information about trapping dynamics of the photo-excited charge carriers. Here we can see a fast component (1ps) which dominates the decay kinetics at 1000 nm. So the extra ultrafast component can be attributed to trapping dynamics due to charge carriers in the QD. Klimov et al [4.2, 4.19] reported a 1.5 ps dynamics in this spectral range and assigned it to the relaxation of the hole. On the other hand, Guyot-Sionnest et al [4.6,21] reported intraband electron transitions in the IR range from 2.5 to 5 μm. Therefore it was debated whether the features observed at even shorter wavelength (1900-2000 nm) could be due to the hole transitions. However in the present studies we are monitoring in the visible to near IR (below 1000 nm), so the trapping dynamics involve in this wavelength region might not be due single carrier (electron or hole). To disentangle the trapping dynamics of individual charge carrier we have realized that it is very important to quench individual carrier (both electron and hole) with suitable quencher and monitor the kinetics, where we can separate the trapping contributions from each of the other charge carrier. As mentioned earlier, addition of these quenchers lead to a pulse width limited separation of charge carriers, therefore they compete with the trapping of charge carriers. The concentrations of the quenchers used in the present study were ~10^{-3} M which is

100 times concentration of the QDs, which will enable efficient separation of the charge carriers from the surface. BQ and BA were used as electron and hole quenchers respectively. To determine the trapping dynamics of hole we have used BQ as electron quencher which can effectively quench the electron. Panel B of Figure 4.5 shows the reverse bleach recovery (Figure 4.5c) kinetics and transient absorption at 1000 nm (Figure 4.5d). The reverse bleach recovery kinetics at 610 nm (Figure 4.5c), which has been fitted with time constants of τ_1 = 5.5ps (56.5%), τ_2=60ps (38.7%) and τ_3 = >400 ps (4.8%) gives an idea of charge recombination dynamics in presence of electron quenchers. However the kinetic trace at 1000 nm can be fitted multi-exponentially with time constants τ_1 = 1ps (72.5%), and τ_2 = 25 ps (22%) τ_3 => 400 ps (5.5 %) in presence of BQ (Figure 5d). The kinetics monitored at 1000 nm in presence of electron quencher gives information on the hole trapping and de-trapping behavior in addition to charge recombination dynamics. So the extra ultrafast component (1 ps) can be attributed to as hole trapping dynamics in CdTe QD.

Now to determine the trapping dynamics of electron we have used BA as hole quencher. Panel C of Figure 4.5 shows the reverse bleach recovery (Figure 4.5e) kinetics and transient absorption at 1000 nm (Figure 4.5f). The reverse bleach recovery kinetics at 610 nm (Figure 4.5a), has been fitted with time constants of τ_1 = 8ps (44.5%), τ_2 = 60 ps (28.6%) and τ_3 => 400 ps (26.9%) attributed to charge recombination dynamics in presence of hole quenchers. On the other hand the kinetic trace at 1000 nm can be fitted multi-exponentially with time constants τ_1 = 0.7ps (80%), τ_2 = 6 ps (1.2%) and τ_3 => 400 ps (19%) in presence of BA. Here the ultrafast component (700 fs) can be attributed to electron trapping in CdTe.

4.4 Conclusion

In conclusion we are report ultrafast charge carrier cooling and trapping dynamics of MPA capped CdTe quantum dot (QD) using femtosecond transient absorption spectrometer by exciting the particles at 400 nm laser light and monitoring the transients visible to near IR region. On laser excitation electron-hole pairs are generated which are confirmed by induced absorption signal for the charge carriers in the visible and near-IR region and bleach at excitonic positions of the QD. Carrier cooling dynamics was followed by monitoring the growth kinetics of the bleach at excitonic wavelengths. The cooling time was measured to be 150 fs and 500 fs for second and first excitonic states respectively. The cooling time for the first excitonic state found to increase with the size of the particles. Further by following the dynamics in presence of quenchers, revealed the involvement of surface defects and Auger mediated processes in relaxation dynamics of CdTe QD. Cooling and trapping dynamics of both electron and hole were determined by using BA as hole quencher and BQ as electron quencher respectively. Hole cooling time has been found to be 200 fs in presence of electron quencher. On the other hand the electron cooling time has been found to be 700 fs in presence of hole quencher. Trapping dynamics of electron and hole have been determined by monitoring transient signal at 1000 nm and by using hole and electron quencher respectively. Electron and hole trapping times have been found to be 700 fs and 1 ps respectively in CdTe QD. Our study also proves that the surface states on CdTe have a major influence the dynamical behavior of QDs, which in turn might have a major influence on the practical application of these QDs.

4.5. References

4.1. Efros, Al. L., Efros, A. Sov. Phys. Sem. 1982, 16, 772

4.2. Klimov, V. I. J. Phys. Chem. B. 2006, 110, 16827.

4.3. Murray, C.; Norris, D.; Bawendi, M., J. Am. Chem. Soc., 115 (1993) 8706.

4.4. Shah, J. *Ultrafast spectroscopy of semiconductors and semiconductor nanostructures*; Springer: New York, 1999.

4.5. Helm, U.; Wiesner, P. *Phys. Re*V. *Lett.* **1973**, *30*, 1205.

4.6. Sionnest, P, G.; Shim, M.; Matranga, C.; Hines, M.; Phys. Rev. B. 1999, 60, 2181.

4.7. Pandey, A.; Sionnest, P. G.; Science 2008, 322, 929.

4.8. Cooney, R. R.; Sewail, S. L.; Anderson, K. E. H.; Dias, E. A.; Kambhampati, P. Phys. Rev. Lett. 2007, 98, 177403.

4.9. Nanda. J.; Ivanov, S. A.; Achermann, M.; Bezel, I.; Piryatinski, A.; and Victor I. Klimov. *J. Phys. Chem. C.* **2007**, *111*, 15382.

4.10. Mikel, S.; Miguel, A. C-D.; Marzan, L. M.- L ; and Abderrazzak, D. J. Photochem. Photobiology. A. **2008**, 196, 51.

4.11. Fragnito, J. L.; Rios, J. M. M.; Duarte, A. S.; Palange, E.; Neto, J. A. M.; Cesar, C. L.; Barbosa, L. C.; Alves, O. L.; and Cruz, G. H. B. J. Phys. Cond. Mater. **1993**, A179-A180, 5.

4.12. Ma, S. M-.; Seo, J. T.; Yu, W.; Yang, O.; Tabibi, B.;Temple, D.; Min, N.; Jung, S. S.; and Kim, W. J. J. Phys. **2008**, 109, 012025.

4.13. Gaponik, N., Talapin D. V.; Rogach, A. L.; Hoppe, K.; Shevchenko, E. V.; Kornowski, A, Eychm¨uller, A and Weller, H. *J. Phys. Chem.* B. **2002,** 106, 7177.

4.14. Yu, W. W.; Qu, L.; Guo, W.; and Peng, X. *Chem. Mater.***2003**, *15*, 2854.

4.15. Ekimov, A. I.; Hache, F.; Klein, M. C. S-.; Ricard, D.; Flytzanis, C.; Kudryavtsev, I. A.; Yazeva, T. V.; Rodina, A. V.; and A. L. Efros, J. Opt. Soc. Am. B. **1993**, 10, 100.

4.16. Esch, V.; Fluegel, B.; Khitrova, G.; Gibbs, H. M.; Jiajin, X.; Kang, K.; Koch, S. W.; Liu, L. C.; Risbud, S. H.; and Peyghambarian, N. Phys. Rev. **1990**, 42, 7450.

4.17. Burda, C.; Green, T. C.; Link, S.; El-Sayed, M. A. *J. Phys. Chem.B* **1999**, *103*, 1783

4.18. Landes, C.; Burda, C.; Braun, M.; and El-Sayed, M. A. *J. Phys. Chem. B*, **2001**, *105*, 2981.

4.19. Klimov, V. I.; Schwarz, Ch. J.; McBranch, D. W.; Leatherdale, C.A.; Bawendi, M. G. *Phys. Rev. B* **1999**, *60*, R2177.

4.20. Guyot-Sionnest, P.; Hines, M. A. *Appl. Phys. Lett.* **1998**, *72*, 686.

Chapter 5

CHAPTER 5

Charge Carrier Dynamics in Tailored CdSe/ ZnTe Core Shell Nanostructure

5.1. Introduction:

Charge recombination in quantum dots (QDs) is an area of current ongoing research due to its important roles in QD-based devices, such as solar cells and light emitting diodes [5.1]. Recent experimental a report on multiple exciton generation (MEG) by one absorbed photon in some QDs [5.2] suggests that the efficiency of QD-based solar cells can be increased dramatically [5.3]. However the main hurdle arises due to exciton-exciton annihilation process in photo-excited QD which occurs on the 10s to 100s ps time scale [5.4]. So it is necessary to dissociate the exciton by ultrafast charge transfer to electron donors and acceptors before the annihilation process. There are few reports in the literature on ultrafast exciton (bound electron-hole pair) dissociation in QDs by electron transfer (ET) or by hole transfer to adsorbed acceptors, however mechanism and rate of charge transfer still poorly understood [5.5-5.9].

As we discussed in early paragraph that for better application of QDs efficient charge separation still remains a challenge. Semiconductor core-shell nanostructure is one of the best possible ways for charge separation which can be synthesized by combining two or more semiconductors with proper lattice match between them. Recently, considerable progress has been made in the synthesis of type II heterojunction nanostructures that spatially separate photoexcited electrons and holes in different parts of a composite QD. These core-shell nanocrystals are made up of two semiconductor materials with a particular alignment of conduction and valence band edges at the interface, which creates a step-like radial potential favoring the localization of one of the carriers in the core of a QD and the other one in the shell. Such a structure is called a staggered band aligned heterostructure or a type II core shell. These nanostructures are important from the point of view of photovoltaic device application, as an improved charge separation enables slower recombination times due to reduced e-h wave function overlap. Secondly the absorption related to direct excitation from one semiconductor can occur, somewhat weakly analogous to an “indirect band gap”, leading to extension of optical response to red side of the electromagnetic spectrum, thus facilitates in covering red region of electromagnetic spectrum. However the performance of such a heterostructure could be hampered due to formation of a defected interface between the core and shell. So it is necessary to understand how fast electron or hole can be separated in core-shell nano-structured and also to understand the effect of defect state on the charge transfer dynamics of Type II core-shell.

Considerable research efforts have been devoted to charge transfer dynamics of type II semiconductor QDs [5.3-5.7, 5.10]. Bawendi and coworkers [5.3] reported the time resolved emission in CdSe/ZnTe and CdTe/CdSe where they have shown that charge recombination time in CdSe/ZnTe can be increased from 9.6ns to 57 ns. In our earlier investigation we have also investigated ultrafast charge transfer dynamics in CdTe/CdS core-shell using femtosecond time-resolved absorption spectroscopy. Chen and coworkers [5.4, 5.11] have reported spatial separation of charge carrier by changing size of core and shell in

CdSe/ZnTe. Feldman and coworkers [5.12] reported charge separation and tunneling behavior between CdTe and CdSe QD material with the formation of core-shell structures. Banin and coworkers [5.13] reported photophysical properties of ZnSe QD within CdS nanorods and demonstrate the charge separation. Most of the above studies have clarified the issue of charge separation clearly; however much more needs to be understood for a device application. For e.g. on UV excitation, certain materials like PbSe, CdTe, PbTe etc [5.6] shows the ability to generate multiexcitons, these multiexcitons need to be separated by e-h energy transfer before they annihilate into a hot exciton, therefore an ultrafast charge separation is required. This indirectly means that we should decrease the interaction between the carriers before they annihilate by Auger recombination [5.6]. Because e-h is mediated by coulomb interaction, lower electron-hole wave function overlap and repulsive biexciton interaction on formation of a Type II heterostructure enables in achieving slower e-h energy transfer. In fact this information have been incorporated in creating better quantum dot by forming a thick shell as previously reported [5.3, 5.7]. Klimov et al [5.7] has shown several orders of magnitude increase in the biexciton recombination by formation of a thick shell. Additionally Sionnest et al [5.3] has exploited the multiple shell configurations to achieve nanoseconds order cooling time. So it is very important know how fast the electrons or holes are migrated to another semiconductor and also how fast the photo excited carriers relaxed in different QD materials.

To understand charge transfer and carrier cooling dynamics in early time scale we have carried out femtosecond transient absorption studies in tailor made CdSe/ZnTe core-shell with different thickness. We have synthesized the core-shell material by adopting eco-friendly colloidal method in water which much less hazardous as compared to organometallic synthesis by arrested precipitation at high temperature [5.3, 5.11]. We have chosen CdSe/ZnTe core-shell where lattice mismatch between core and shell is less than 1 % which ensures less defect (cleaner) surface and minimizes non radiative relaxation via interface defects or charged excitons. Core-shell materials have been characterized by steady state optical absorption and emission studies and also in high resolution TEM (HRTEM) technique. To unravel the charge transfer dynamics we have carried out transient absorption studies in ultrafast time scale detecting the transients in visible to near-IR region by exciting both CdSe core and CdSe/ZnTe core-shell material by exciting at 400 nm laser light. Detail mechanism of charge transfer and carrier cooling mechanism has been discussed.

5.2 Experimental

5.2.1. Materials:

Cadmium chloride (≥99%), Te powder (≥98), 1-mercaptopropionic acid (≥99%), $NaBH_4$ and benzoquinone were purchased from Aldrich and used it as received without further purification. Isopropyl alcohol was used as received from s.d.fine chemicals. Pyridine (Fluka) was used after distillation.

5.2.2. Synthesis of CdSe QDs:

Thiol capped CdSe QD was prepared by following previously reported method [5.12]. In brief, cadmium chloride (cadmium precursor) was dissolved in N_2 purged nanopure water followed by addition of 1-mercaptopropionic acid (MPA). The solution pH was adjusted to 9-10 using 1M NaOH. NaHSe (Selenium precursor) solution was prepared fresh by reducing Se with $NaBH_4$ with Se: $NaBH_4$=1:2 in water maintained at 273K for 1h. NaHSe was added to cadmium precursor solution with vigorous stirring. The ratio between Cd, MPA and Se was maintained at 1:2.5:0.5. The above solution was refluxed for six hours. Reaction mixture was allowed to cool naturally and was concentrated to 1/3rd of its original volume by using rotary evaporator. QDs were precipitated by adding Isopropyl alcohol as the nonsolvent. Supernatant was discarded and precipitate was re-dissolved in nanopure water and finally re-precipitated. The cleaning was complete by a 3 time dissolution and re-precipitation procedure to remove un-reacted precursors. These samples were dried in ambient for further use.

5.2.3. Shell Growth:

For shell formation the concentration of the precursor for formation of 2.5nm shell was calculated according to reported methods. 10^{-6}M MPA capped CdSe was dissolved in N_2 purged water. To this solution zinc nitrate hexahydrate and MPA solution in 1:2.5 molar ratio was added and pH was adjusted to 9-10. NaHTe (tellurium precursor) solution was prepared fresh by reducing Te with $NaBH_4$ with Te: $NaBH_4$=1:2 in N_2 purged water maintained at 273K for 8h. This was added to the above prepared QD solution with Zn precursor with vigorous stirring. The Zn: MPA: Te molar ratio was maintained at 1:1.5:0.5. The solution was refluxed for 6h for the growth of shell. To obtain shells of different shell thickness the samples were eluted at different time (1/2h, 1h, 2h, and 6h). The cleaning procedure was the same as described above for the CdSe QDs. The four samples are named as CdSe/ZnTe1, CdSe/ZnTe2, CdSe/ZnTe3, and CdSe/ZnTe4

with increasing shell thickness order which were eluted at 1/h, 1h, 2h and 6h respectively.

5.3. Result and discussion:

5.3.1. TEM & XRD Studies

The TEM pattern (figure 1) clearly shows crystallite size of about ~7nm. The CdSe core diameter is ~2nm as revealed by UV-Vis absorption studies. There is no clear discernable core and shell separation due to very small change in the lattice spacing between CdSe and ZnTe. The thickness of the shell as inferred from the TEM for CdSe-ZnTe sample is ~3.5nm.

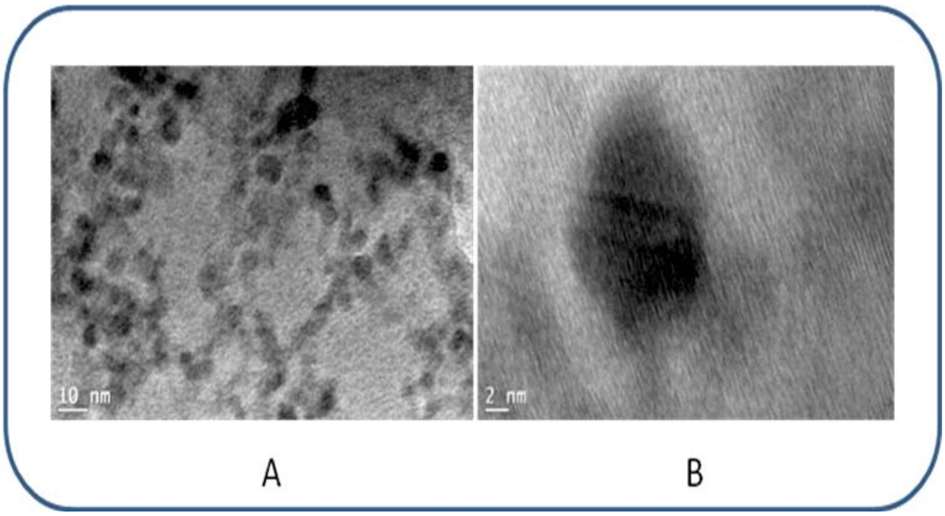

Figure 5.1: High-resolution TEM (HR-TEM) image of CdSe/ZnTe quantum dot core-shell (Panel A) and same picture in higher resolution Panel B).

Insets: Selected electron diffraction patternof the corresponding particles.

The XRD paterns given in figure 2 shows lattice spacing as observed in the above case is ~0.32nm which matched with the spacing for (111) plane. The clearly discerning feature is the broad peak at 25.4° can be assigned to (111) plane of CdSe. The peak broadening in the present case is due to smaller crystallite size which is ~ 2nm according to optical absorption spectra. This value also matches with the domain size obtained from Debye Scherrer formula of ~2nm.

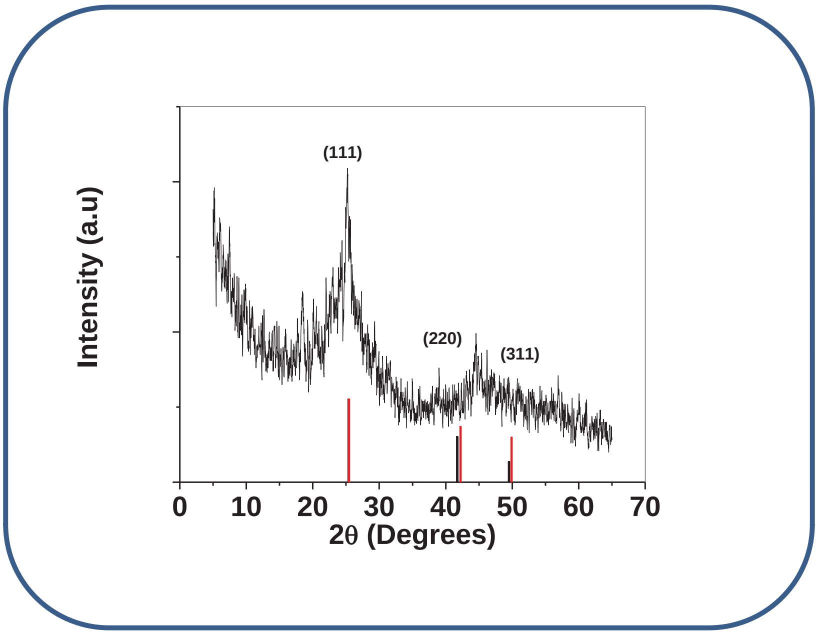

Figure 5.2: XRD Pattern for CdSe/ZnTe quantum dot core-shell

5.3.2. Steady state absorption and emission studies:

In the present investigation to characterize the QD materials we have carried out steady state absorption and emission spectroscopy. Figure 3 indicates normalized steady state absorption spectrum of CdSe (Core) and CdSe/ZnTe core-shell material. In absorption spectrum it can be clearly seen that CdSe (shown in black solid line) has first exciton peak 1S(e)-1S$_{3/2}$(h) around 455nm (Figure 3a) (referred hereafter as 1S). Assignment of this exciton is made by usual notation [5.14]. The exciton peak appears for CdSe QD appears at ~455nm which is considerably shifted compared to bulk band gap of ~1.9eV for CdSe indicating a confinement induced shift. Particle size of as prepared CdSe QD calculated by using sizing curve given by Peng [5.15] and coworkers is around 2 nm. The figure indicates an evident red shift of 1S exciton peak with increasing thickness of ZnTe (Figure 3). From our optical absorption studies, we can clearly see that the formation of ZnTe shell on CdSe core, where exciton peak shows red shift with increasing thickness of ZnTe. It has been observed that exciton peak of core-shell CdSe/ZnTe1 (thinnest shell) shifted to ~470 nm, for CdSe/ZnTe2 it has been shifted to ~482 nm and for CdSe/ZnTe3 the exciton peak shifted to ~ 492 nm from exciton peak of CdSe which has been observed at ~455nm.

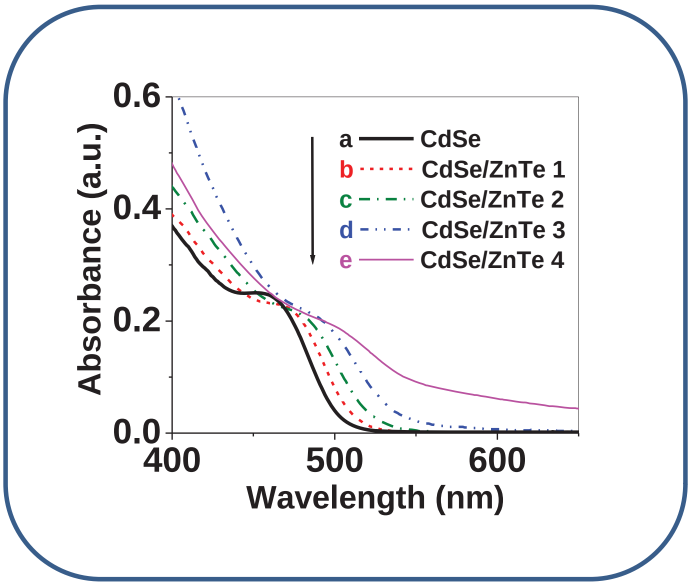

Figure 5.3: Steady state absorption spectra of a) CdSe (thick solid line), b) CdSe/ZnTe1 (short dash), c) CdSe/ZnTe2 (dash dot), d) CdSe/ZnTe3 (dash-dot-dot) and e) CdSe/ZnTe4 (thin solid line),

In the present case the band offsets are in such a way that on photoexcitation the hole can be transferred to ZnTe shell. Therefore the dielectric constant and confinements are considerably different leading to wave function manipulation enabling a redshift [5.3]. UV-vis absorption spectra of the thickest sample show a featureless absorption from Visible- NIR region. This absorption is related to direct transition from ZnTe valence band to CdSe conduction band. It is clear that in the NIR region it is considerably weak due to forbidden nature of the transition [5.3, reference therein]. The distinguishing feature of the core shell samples is an increase in the absorbance with an increase shell thickness in the blue side of the exciton transition indicating a clear increase in the DOS contribution from the ZnSe also towards the optical absorption.

To corroborate optical absorption properties in the above systems we have also carried out steady state emission spectroscopy for CdSe QD and CdSe/ZnTe core-shell material of different thickness and are shown in Figure 5.4. Figure 5.4a shows broad emission band from 525 -770 nm with a peak 650 nm for CdSe QD samples. The emission with a large stoke shift clearly indicate the emission originate from surface states. Earlier Wuister et al [5.16] reported emission from surface states from thiol capped CdSe where the inter band gap states are formed via interaction of thiolate group with the metal ion. However on formation shell the emission spectra of CdSe/ZnTe core-shell systems changes dramatically. Figure 4b shows broad emission spectra for CdSe/ZnTe1 core-shell (thinnest shell) with two emission peaks at 524 and 633 nm. The band at 523 nm region can be attributed as exciton emission and the emission band at 633 nm shows large stoke shift which can be attributed to surface (defect) state emission. This clearly indicates that the shell formation is not complete for the CdSe/ZnTe1 core-shell sample. However it is interesting to see that on formation of ZnTe shell surface state emission is drastically reduced. In CdSe/ZnTe2 core-shell sample (Figure 4c) we can observe only one peak at 600 nm, which can be attributed to exciton emission of CdSe/ZnTe2 core-shell. We have observed in optical absorption studies that on formation type II shell absorption peak moves towards to red region of the spectrum. As we have discussed that on formation shell surface state emission are drastically reduced so the emission observed in these type II core shell are due to "indirect" emission where electrons reside in the CdSe core and hole in ZnTe shell. Earlier Kim et al [5.2] reported gradual red shift of type II core shell emission in CdTe/CdSe core-shell with increasing shell thickness. We can still see further red shift in emission spectra for CdSe/ZnTe3 core-shell in Figure 4d. We have also excited CdSe/ZnTe4 core-shell to find out the emission band. The emission could not be detected in the visible region as the emission might be appearing in the near-IR region which beyond the detection limit of our instrument.

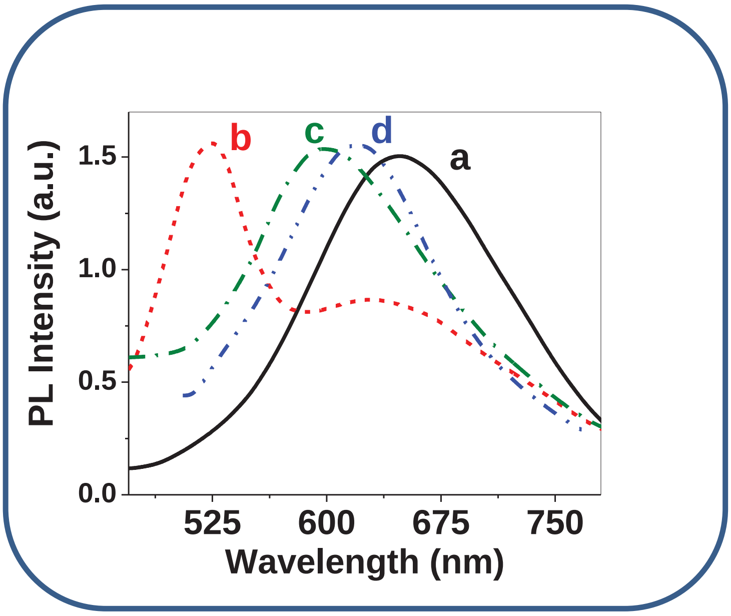

Figure 4: Normalized steady state emission spectra of a) CdSe (thick solid line), b) CdSe/ZnTe1 (short dash), c) CdSe/ZnTe2 (dash dot), and d) CdSe/ZnTe3 (dash-dot-dot).

5.3.3. Time resolved emission studies:

To ascertain influence of shell formation on the recombination dynamics we have carried out time-resolved emission studies for CdSe QD and CdSe/ZnTe core-shell material of different thickness and the emission decay kinetics are shown in Figure 5.5. It is clear from the kinetic decay trace that on shell formation emission lifetime increases in core-shell materials. It is clear from our observation that the recombination dynamics for the photoexcited electron-hole pairs is longer in Cdse/ZnTe core shell as compared to the CdSe core. Similar observation we made in our earlier investigation [5.19] where the emission life time of CdTe/CdS type II core-shell drastically increased as compared to CdTe core. In the present studies we have compared emission decay kinetics for CdSe QD and CdSe/ZnTe1 (thinnest shell) and CdSe/ZnTe3 (thick shell). For all samples time resolved emission measurement has been done at their peak emitting wavelengths and exciting at 454 nm. The emission decay kinetics for CdSe can be fitted multi-exponentially with time constants τ_1= 0.50 ns (59%), τ_2= 3.8 ns (34%), τ_3= 17.4 ns (7%) with average time (τ_{av}) of 2.8 ns (Figure 5a). Figure 5b shows the emission decay kinetics for CdSe/ZnTe1 (thinnest shell) which can be again fitted multi-exponentially with time constants τ_1= 0.60 ns (65%), τ_2= 3.7 ns (18.6%), τ_3= 16.3 ns (16.4%) with average time (τ_{av}) of 3.75 ns.

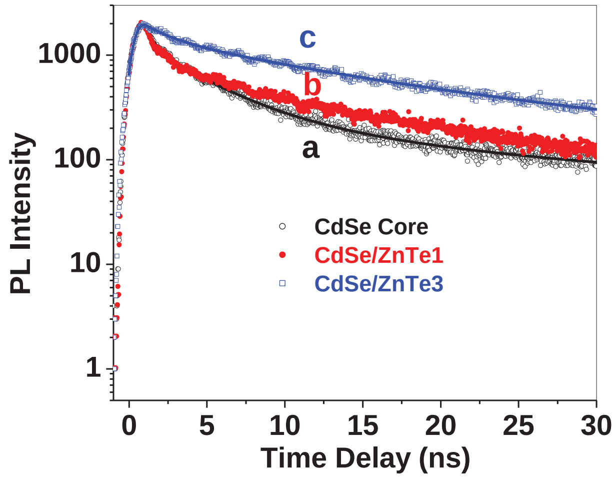

Figure 5.5: Time resolved emission decay traces of a) CdSe, b) CdSe/ZnTe1, and c) CdSe/ZnTe3.

As we have mentioned in earlier section that shell formation is not complete similarly from time resolved emission data we can see that the emission kinetics still dominated by CdSe core emission. However we can still see that contributions of shorter components decrease and longer component increases for CdSe/ZnTe1 core-shell as compared to CdSe core. Finally we have shown the emission kinetics decay trace for thicker shell CdSe/ZnTe3 in Figure 5.3c, which can be fitted bi-exponentially τ_2= 2.19 ns (41%), τ_3= 18 ns (59%) with average time (τ_{av}) of 11.5 ns as given in the Table 5.1. Interestingly we can observe that the fast component (τ_1) is missing in the kinetic decay trace in CdSe/ZnTe3 sample.

Sample	**t_1(ns)**	**t_2(ns)**	**t_3(ns)**	**t_{avg}(ns)**
CdSe	0.5 (59%)	3.8 (34%)	17.4(7%)	2.8
CdSe/ZnTe1	0.6(65%)	3.7(18.6)	16.3(16.4%)	3.75
CdSe/ZnTe3		2.19 (41%)	18 (59%)	11.5

Table 5.1: Fits for emission decay traces for core and core shell samples

We can observe a fourfold increase of average lifetime in CdSe/ZnTe3 core-shell as compared to CdSe core. The spatial separation of electron and hole can result in a decrease of the wave function overlap and thus longer lifetime of charge recombination is expected in type II heterostructures. Our observation indicates that the formation of shell leads to an increase in lifetime which can be concluded as the clear evidence of reduced electron hole wave function overlap in core-shell material. Furthermore present study confirms the Marcus theory predictions which indicate an inverted regime in the present case which would in turn indicate that the reorganization energies are very small. In case of quantum solvent seldom plays an important role as the excitons or the charge carriers are well localized within the bulk of the quantum dot. Therefore the nuclear reorganization energy arising from exciton-phonon coupling plays an important role in the charge recombination dynamics. To ascertain the role of nuclear reorganization we calculate the reorganization energy and free energy change in the case of CdSe/ZnTe3 as described by Scholes et al [5.19]. We find that the reorganization energy, λ= 90meV and ΔG= -0.36eV. This clearly shows that for that sample – $\Delta G > \lambda$, inverted regime in terms of Marcus theory. This is also in accordance with previous study by Scholes et al [5.19]. Such a situation arises in the case of quantum dot core shell samples due to a very weak exciton-phonon coupling in these cases. While the information regarding recombination dynamics have been instructive in ascertaining the role of shell in improving charge separation behaviour, complete understanding on carrier dynamics is not obtained just from radiative recombination as we neglect information on the nonradiative processes which often come from defects. To ascertain role of nonradiative processes we have carried out femtosecond transient absorption.

5.3.4. Transient absorption spectroscopy of CdSe QD:

To understand further details about the dynamics of both radiative and non-radiative and charge transfer dynamics in CdSe/ZnTe core-shell QD, we have carried out transient absorption studies on both CdSe QD and CdTe/ZnTe core-shell by exiting the samples at 400nm light and monitoring the transients in the visible region. Figure 5.6 shows the transient absorption spectra of photoexcited CdSe QD materials in different time delay, which comprises a negative absorption band in 460 nm to 540 nm region and a broad positive absorption band in 550 nm – 700 nm region. The first exciton position for the CdSe core samples (Figure 3a) appear ~ 455nm, however in the transient spectrum we could show only second half of exciton bleach due to very low intensity of probe light in white light in the present experimental set-up. In steady state absorption spectrum of CdSe QD we have observed exciton peak at 455nm. Similarly, we observed bleach peak below 560nm in transient spectrum of CdSe QD. In our earlier investigations [5.20] we have described that bleach in transient spectrum of CdTe was due to state filling effect. In the present investigation also we can conclude that bleach feature in the transient spectrum is due to the ground state population depletion. The transient positive absorption beyond 550 nm regions can be attributed to absorption of light by photo-generated charge carriers (both electrons and holes) in free or in trapped in the defect states of QDs. In addition to that positive absorption can also arise due to non-linear effects like two electron-hole pair interaction (bi-exciton effect) and trapped-carrier induced stark effect. To exclude these many-particle interactions we have recorded the transient data at low pump intensity so that average number of electron-hole pair ($<N_{eh}>$) is less than 1.

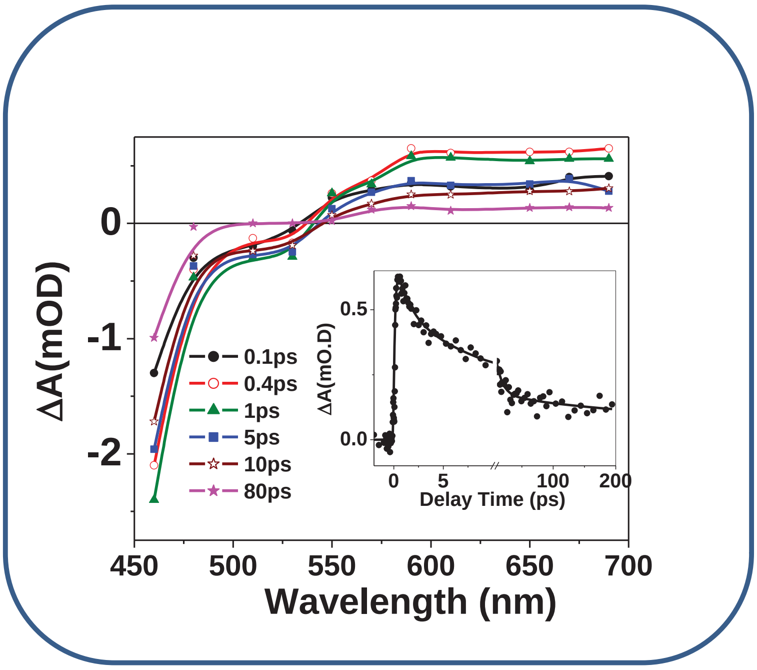

Figure 5.6: Transient absorption spectra of CdSe quantum dot (QD) at different time delay after excitation at 400 nm laser light. Inset: Kinetic decay trace monitored at 690 nm.

Furthermore the stark effect induced absorption feature is highly unlikely as the feature shown is broad whereas stark effect induced features are expected to lie on the either side close to the exciton feature, also we have maintained N<<1, therefore nonlinearities in the dynamical spectrum is negligible [5.5]. The broad feature beyond the exciton bleach feature can arise from trapped carriers or intraband transitions [5.18]. The assignment of this feature to intraband transition is highly unlikely as the intraband transition show very fast decay (few ps) and highly wavelength dependent kinetics which is not observed in the present investigation. So from the above observation we can safely conclude that the feature most likely comes from trapped carriers.

To monitor the charge carrier dynamics in CdSe QD we have monitored the bleach recovery kinetics at 460 nm and transient decay kinetics at 720 nm. Figure 6A show the bleach recovery kinetics of CdSe QD at 460 nm (1S Excitonic position). The growth kinetics of the bleach at 460 nm can be fitted 155 fs and the recovery kinetics can be fitted multi-exponentially with time constants 2.55 ps (45%), 27 ps (17%) and > 400 ps (38%). Here 155 fs time constant can be attributed to state filling to 1S excitonic level [5.8]. The bleach recovery time constants suggest the charge recombination time constants between photo-generated electrons and holes. We have also monitored decay kinetics of excited state absorption (ESA) of photo excited CdSe at 690 nm (Figure 5.4 inset) which can be fitted multi-exponentially 1.3ps (30%), 10 ps (45%) and >200 ps (25%). It is interesting to see that growth time of the signal can be fitted single exponentially with pulse-width limited time constant (< 100 fs). Earlier investigations suggest that the positive absorption band in NIR region is mainly due to intraband transition of the photo excited holes [5.21]. In our early studies of CdTe QD we have observed that positive absorption can be due to both the trapped charge carriers (electron and hole).

5.3.5. Transient absorption studies of CdSe/ZnTe core-shell QD:

In the present studies we have intended to study charge carrier dynamics (cooling and trapping) and charge transfer dynamics in core-shell nano-structure. For this purpose we have chosen two different QD core-shell samples CdSe/ZnTe3 and CdSe/ZnTe4 where core size of CdSe QD kept same but the ZnTe shell thickness was different. Figure 7 shows the transient spectra for the above two core-shells. Figure 7 shows the excitonic bleach peak at 490 nm for CdSe/ZnTe3 core-shell and at 510 nm for CdSe/ZnTe4 core-shell which matches with position of exciton from optical absorption.

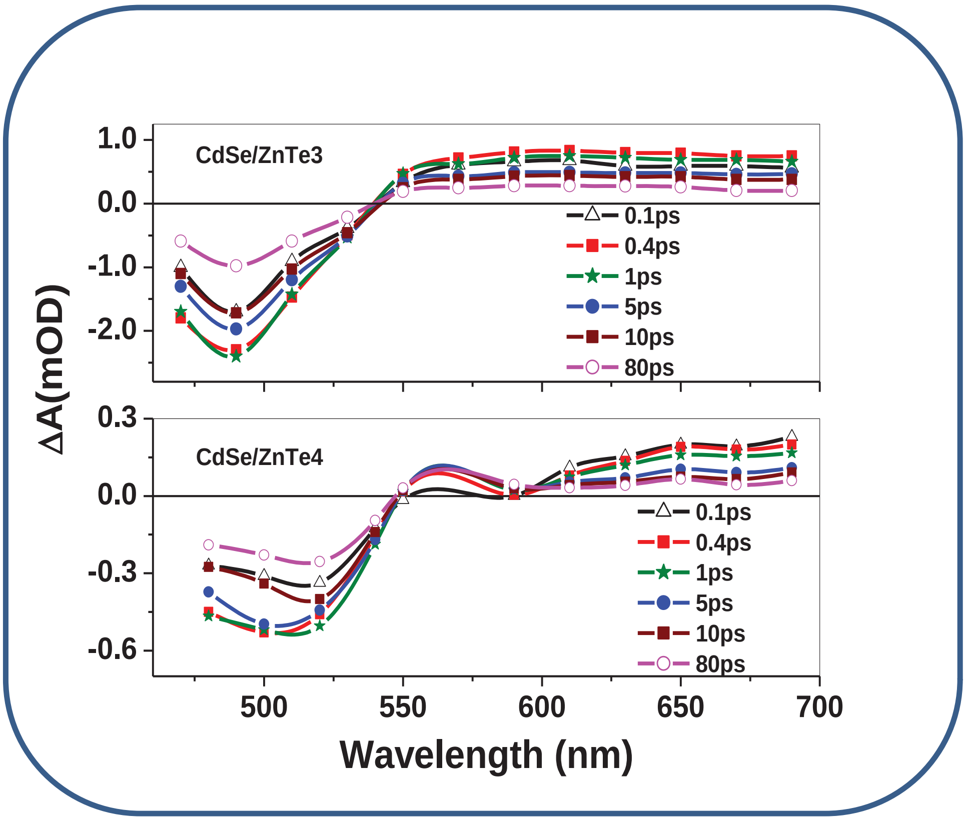

Figure 5.7: Transient absorption spectra of CdSe/ZnTe3 (top panel) and CdSe/ZnTe4 (bottom panel) Quantum dot core-shell at different time delay after excitation at 400 nm laser light.

Earlier authors [5.4] reported charge transfer dynamics in type II CdSe/ZnTe core-shell QD using time-resolved emission spectroscopy. However in the present studies first time we are reporting time-resolved absorption studies where we have observed exciton peak shift in the red region in TA spectrum with the formation of shell and further on increasing thickness. However it is interesting to see that that relative intensity of positive absorption and exciton bleach intensity does not change with increasing the thickness of shell material as the lattice mismatch between CdSe and ZnTe are < 1 %. Here on photoexcitation of CdSe/ZnTe core-shell by 400 nm majority of the photon excite CdSe QD and electron and holes are generated in CdSe core.

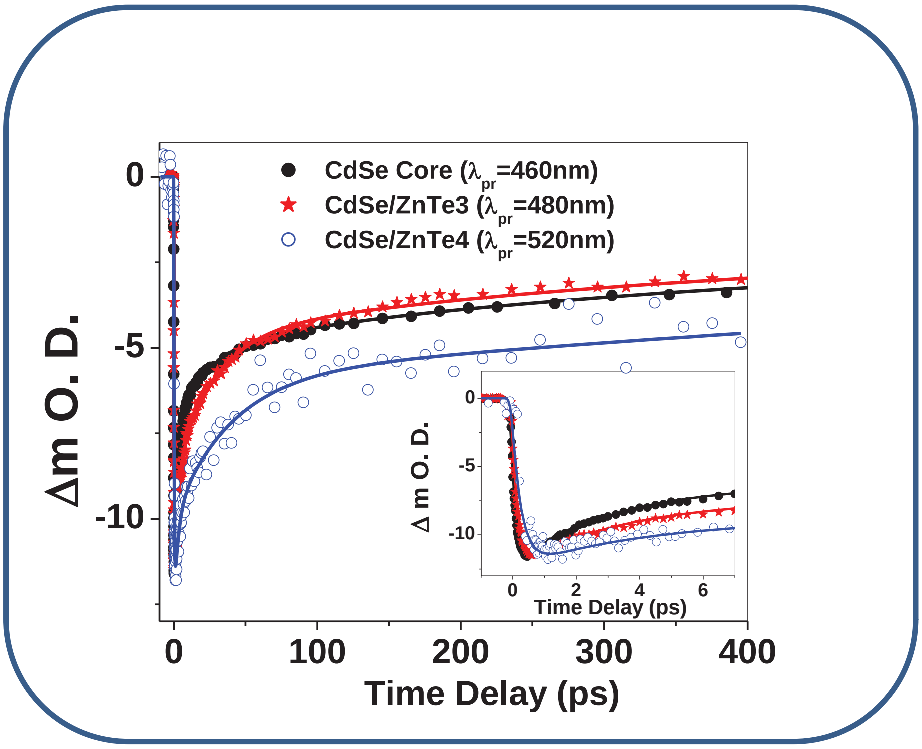

Figure 5.8: Normalized kinetic traces of a) CdSe at 460 nm, b) CdSe/ZnTe3 at 480 nm, and c) CdSe/ZnTe4 at 520 nm after excitation at 400 nm laser light. Inset: Same kinetics are shown at shorter time scale.

However, due to staggered band alignment between CdSe and ZnTe, photoexcited hole which was generated in CdSe core will migrate to ZnTe shell. Now to understand charge carrier cooling dynamics and charge transfer dynamics we have monitored the kinetics at the bleach wavelengths for CdSe core and CdSe/ZnTe core-shell of different thickness and shown in Figure 8. In the inset of Figure 8 we have shown the bleach kinetics at shorter time scale.

We can clearly see that the growth time of the bleach from core to core-shell and further on increasing shell thickness. The growth time can be fitted with time constants of 155fs for CdSe core, 180 fs for CdSe/ZnTe3 and 300 fs for CdSe/ZnTe4 core-shell (Table 2). This growth time of the bleach can be attributed cooling of the charge carriers [5.8]. In a bulk semiconductor the cooling of carriers is expected to be pulse width limited. This can be rationalized as follows, on photoexcitation the carriers are initially populated in the higher exciton level as 400nm laser light populates the higher excitons which finally populates the lowest excitonic state with the formation of 1S bleach [5.20]. In QD bleach formation is delayed due to quantized nature of the individual bands [5.1]. The main contribution to cooling of the carriers comes from Auger mediated or surface mediated processes as reported earlier and not by multi-phonon emission. Since density of states (DOS) of holes are much larger compared to electrons because of higher effective mass and degenerate valence band, faster cooling of hole is achieved by of electron-hole (e-h) mediated energy transfer and subsequent electron cooling [5.8, 5.22-5.23]. So in the present investigation we attribute that the cooling of the charge carrier mainly to electron cooling.

Sample	t_r(ps)	t_1(ps)	t_2(ps)	t_3(ps)
CdSe	0.155	2.55(45)	27(16.8)	>400(38.2)
CdSe/ZnTe3	0.18	2.59(30)	30(33)	>400(37)
CdSe/ZnTe4	0.3	3(21.4)	50(32.5)	>1000(46.1)

Table 5.2: Fit for kinetic traces of a) CdSe at 460 nm, b) CdSe/ZnTe3 at 480 nm, and c) CdSe/ZnTe4 at 520 nm after excitation at 400 nm laser light.

To understand the influence of thickness of shell on cooling dynamics after photoexcitation we have shown the photoinduced process in Scheme 1. As illustrated in the scheme 1, 400nm light can either excite the carriers directly from ZnTe to CdSe by a charge transfer or CdSe may be first excited and hole transfer occurs subsequently. However the possibility of direct excitation from ZnTe to CdSe is very low due to forbidden nature of the transition. Therefore, we can safely assume that the excitation initially populates the CdSe levels and then holes are transferred to ZnTe. Assuming that holes are injected from CdSe, there are two ways hole can be transferred from CdSe to ZnTe as depicted in Scheme 1.

In route I, photo-generated holes in CdSe can cool and then be transferred to ZnTe shell. On the other hand in route II hot holes from CdSe can be directly transferred to ZnTe and get cooled in the valence band of ZnTe. We can find out the most probable route by analysis the cooling dynamics of charge carriers in both core and core-shell samples. We have observed that cooling time as monitored by bleach formation kinetics of charge carrier (mostly contributed from electron) increases with the thickness of the shell from 150fs for CdSe to ~300fs for CdSe/ZnTe4 core shell.

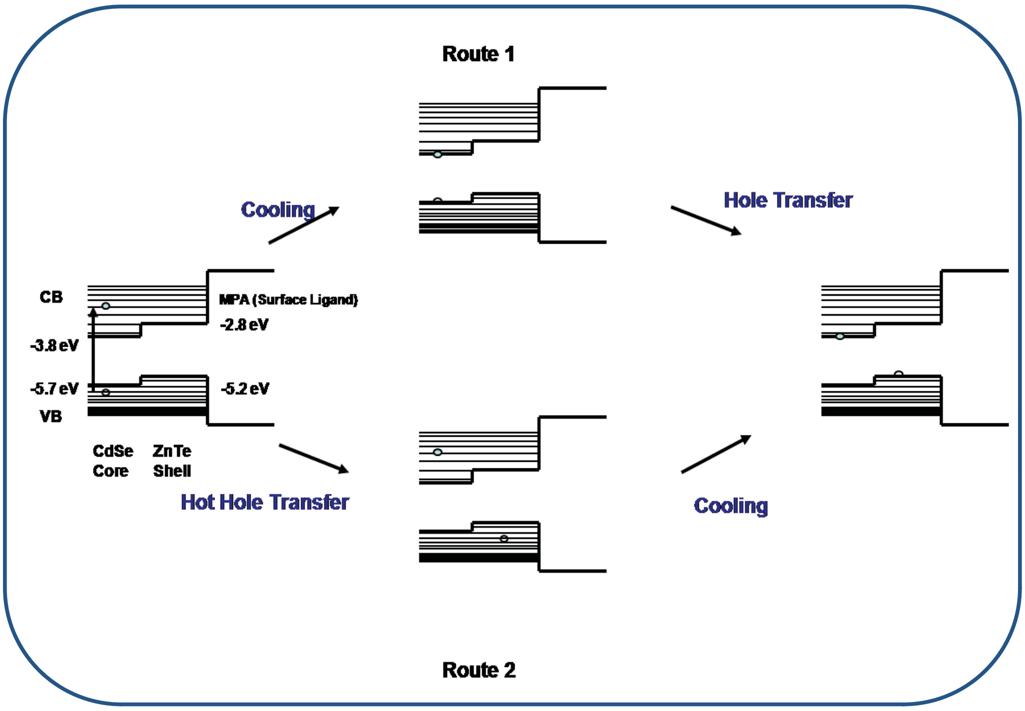
Route 1
Cooling
Hole Transfer
CB
MPA (Surface Ligand)
-2.8 eV
-3.8 eV
-5.7 eV
-5.2 eV
VB
CdSe
Core
ZnTe
Shell
Hot Hole Transfer
Cooling
Route 2

Scheme 5.1: Schematic representation of the energy level (both valence band and conduction band) of CdSe and ZnTe bulk semiconductor, where energy levels are shown with respect to vacuum. Charge transfer and cooling dynamics are depicted in the diagram

The observation of slower cooling in core shell samples implies that interaction between electrons and holes are hindered due to charge separation as e-h energy transfer mediates the cooling. The above process is only possible when hole is transferred before electron cooling otherwise we would not see any effect of shell thickness on cooling dynamics. Support for this assessment also comes from the fact that initially populated higher hole levels in CdSe core has a significant overlap with hole levels in ZnTe enabling the hot hole injection into shell. Therefore based on these argument we can conclude that route II as depicted in the scheme is the most likely process occurring.

In addition to the cooling dynamics Figure 8 also shows the bleach recovery dynamics of core and different core-shells. The bleach recovery kinetics can be fitted multi-exponentially with different time constants with τ_1 = 2.55 ps (45%), τ_2 = 27 ps (17%) and τ_3 = > 400 ps (38%) for CdSe core, τ_1 = 2.6 ps (30%), τ_2 = 30 ps (33%) and τ_3 = > 400 ps (37%) for CdSe/ZnTe3 core-shell and τ_1 = 3 ps (21.5%), τ_2 = 50 ps (32.5%) and τ_3 = > 400 ps (46%) for CdSe/ZnTe4 core-shell. It clearly hints at the multi-exponential nature of bleach recovery tell us that the charge carrier dynamics is governed by more than one process. The multi-exponential nature of the dynamics can come from multiple sizes QD in addition to trapping dynamics of trap states. If the dynamics is dominated by only one lifetime contribution it could come from single dot contribution. However in the present case we have long component which contributes quite substantially (> 30%). Since under the present excitation conditions N<<1, we can conclude with certainty that biexciton and stark effect contribution is negligible in the present studies. Furthermore, we can rule out size distribution as the cause of the multiexponential nature as position of the bleach wavelength does not change with time even up to 80 ps. So the multi-exponential dynamics can only come from different processes and traps are the most likely candidate. Comparison of bleach recovery kinetics from CdSe core to CdSe/ZnTe core-shell with different thickness reveal that the contribution of first component (τ_1) reduces from ~45% to 21.5% for CdSe core to CdSe/ZnTe4 core shell. τ_1 contribution can be attributed to electron traps at the surface of CdSe, as this component still remains in the core shell samples also. Further evidence for this assignment also comes from the fact that CdSe surface is truncated by MPA by formation of Cd-S thiolate linkage. It is well known that thiolate linkages act as hole traps and if the hole traps are the reason for that contribution we can expect the contribution to completely disappear on the formation of shell. Therefore we can conclude that decrease in the contribution in the core shell samples is due to annihilation of Cd related dangling bonds which act as electron traps at the surface. Now let us discuss the dynamics associated with the τ_2 and τ_3 components. We can clearly see that both amplitude and contribution of the τ_2 and τ_3 components increases with the thickness of the shell. This observation clearly suggest us that τ_2 and τ_3 components are might be due to charge recombination indicating better charge separation on formation of shell. This observation is also supported by time-resolved photo-luminescence studies as discussed in earlier section.

5.4. Conclusions

In conclusion, we have synthesized thiol capped CdSe QD and CdSe/ZnTe type II core-shell nano hetero structure which characterized by steady state absorption, steady state emission study and high resolution transmission electron microscopyCdSe QD shows emission purely due to surface state however on formation of ZnTe shell surface state emission drastically reduce with the appearance of exciton emission. Steady state emission studies indicate red shift in peak position of excitonic emission with shell thickness. Time resolved emission kinetics suggest that average radiative lifetime of CdSe-ZnTe core-shell increases by fourfold as compared to CdSe core, which clearly suggest spatial separation electron and hole in core-shell. To understand both charge transfer and carrier cooling dynamics we have carried out femtosecond time-resolved absorption studies in the visible region. Our ultrafast studies suggests that photoexcitation of CdSe-ZnTe core-shell initially electron and holes are generated in the CdSe core and holes are migrated to ZnTe shell in pulse-width time scale followed by electron cooling in CdSe core which is greatly affected by the thickness of ZnTe shell. Our studies suggest that trapping dynamics plays a major role in the relaxation dynamics of photo-excited charge carriers in both core and core-shell materials. Traps states influence the overall performance of the devices constructed with quantum dots and core-shell nanostructure material. Our studies suggest that involvement of trap states adversely affect the charge carrier dynamics of quantum dot materials which very important in technological application view point.

5.5. References

5.1. Nozik, A.; Ann. Rev. Phys. Rev. 1996, **52**, 193.

5.2. Kim, S.; Fisher, B.; Eisler, H.; and Bawendi, M., *J. Am. Chem. Soc*. **2003**, *125,* 11466.

5.3. Anshu Pandey and Philippe Guyot-Sionnest, *Science* **2008**, 322, 929.

5.4. Chen, C. Y.; Cheng, C. T.; Yu, J. K.; Pu, S. C.; Cheng, Y. M.; Chou, P. T.; Chou, Y. H.; Chiu, H. T.; J. Phys. Chem. B, 2004, 108, 10687.

5.5. Dooley, C. J.; Dimitrov, S. D.; Fiebig, T.; J. Phys. Chem. C, 2008, 112 (32), pp 12074–12076

5.6. Schaller, R. D.; Klimov, V. I. *Phys. Rev. Lett.* **2004**, *92*, 186601.

5.7. Garca-Santamara, F.; Chen, Y.; Vela, J.; Schaller, R. D.; Hollingsworth, J. A.; Klimov, V. I.; Nano Lett., 2009, 9 (10), pp 3482–3488

5.8. Klimov, V. I. J. Phys. Chem. B. **2006**, 110, 16827.

5.9. Klimov, V. I. ; McBranch, D. W. ; Leatherdale, C. A.; Bawendi, M. G. Phys. Rev. B. **1999**, 60, 13740.

5.10. L. P. Balet, S. A. Ivanov, A. Piryatinski, M. Achermann, and V. I. Klimov, Nano Lett., **2004**, 4, 1485-1488. (b) Alexander Nemchinov, Maria Kirsanova, Nishshanka N. Hewa-Kasakarage, and Mikhail Zamkov, *J. Phys. Chem. C* **2008,** *112*, 9301–9307. (c) Qinghui Zeng, Xianggui Kong, Yajuan Sun, Youlin Zhang,, Langping Tu, Jialong Zhao, and Hong Zhang, *J. Phys. Chem. C* **2008,** *112*, 8587–8593.

5.11. Chun-Yen Chen, Chiu-Ting Cheng, Jen-Kan Yu, Shih-Chieh Pu, Yi-Ming Cheng, and Pi-Tai Chou. *J. Phys. Chem. B*, **2004**, *108* (30), pp 10687–10691.

5.12. Gross, D.; Susha, A.; Klar, T.; Como, E.; Rogach, A.; Feldmann, J. *Nano Lett.* **2008**, 8, 1482.

5.13. Dorfs, D.; Salant, A.; Popov, I.; Banin, U. *Small* **2008**, 4, 1319.

5.14. Efros, A. L.; Rosen, M. *Annu. Rev. Mater. Sci.* **2000** 30, 475. (b) Norris, D. J.; Bawendi, M. G. *Phys. Rev. B* **1996** , 53, 16338.

5.15. Yu, W. W.; Qu, L.; Guo, W.; and Peng, X. *Chem. Mater*. **2003**, *15*, 2854.

5.16. Sander F. Wuister, Celso de Mello Donegá, and Andries Meijerink, *J. Phys. Chem. B*, **2004**, *108* (45), pp 17393–17397.

5.17. Andrey L. Rogach, Andreas Kornowski, Mingyuan Gao, Alexander Eychmüller, and Horst Weller, *J. Phys. Chem. B*, **1999**, *103* (16), pp 3065–3069.

5.18. Sachin Rawalekar, Sreejith Kaniyankandy, Sandeep Verma and Hirendra N. Ghosh, *J. Phys. Chem. C,* **2010,** *114*, 1460.

5.19. Scholes, G. D.; Jones, M.; Kumar, S.; J. Phys. Chem. **2007**, 111, 13777.

5.20. Sreejith Kaniyankandy, Sachin Rawalekar, Sandeep Verma, Dipak K. Palit and Hirendra N. Ghosh, *Phys. Chem. Chem. Phys.***, 2010,** 12**, 4210.**

5.21. Landes, C.; Burda, C.; Braun, M.; El-Sayed M. *J. Phys. Chem. B* **2001**, *105*, 2981.

5.22. Sionnest, P, G.; Shim, M.; Matranga, C.; Hines, M.; Phys. Rev. B. **1999**, 60, 2181.

5.23. Guyot-Sionnest, P.; Hines, M. A. *Appl. Phys. Lett.* **1998**, *72*, 686.

Chapter 6

CHAPTER 6

Charge Separation in CdTe Decorated Graphene

6.1. Introduction

Graphene is a 2-D array consisting of sp^2 hybridized carbon atoms in a honeycomb lattice. This distinctive structure imparts graphene with a unique linear electronic dispersion near the K-point of the Brillouin zone [6.1] which leads to relativistic velocity of ~ 10^6m/s and mobility of ~15000 cm^2/Vs for the electrons [6.2]. These unique properties are ideally suited for application in fast electronic devices like transistors, diodes and oscillators [6.3]. Apart from these applications, graphene has been exploited for verifying table top quantum electrodynamics experiments due to its unique electronic structure. Previously, several groups have verified a number of exotic behaviors like the observation of room temperature Quantum Hall Effect [6.4], Klein paradox [6.5] etc. These applications and interesting novel properties of graphene have given impetus to their synthesis by different routes. The first report on synthesis of graphene was by Geim et al [6.4] who produced graphene by micromechanical cleavage from highly oriented pyrolitic graphite (HOPG) using a scotch tape [6.2]. Graphene prepared by micromechanical cleavage was used to verify several novel attributes of graphene like observation of Klein paradox, Quantum Hall Effect, high mobility etc. at room temperature. However, from the application point of view, the scotch tape method is not very conducive due to non scalability.

Recently several methods like chemical vapor deposition (CVD) [6.6], decomposition of SiC at higher temperature [6.7], and chemical methods like oxidation promoted exfoliation [6.8] have been proposed as possible route to synthesis of graphene. Decomposition of SiC to form hexagonal graphene lattice have shown promising behavior similar to the ones prepared by micromechanical cleavage used by Geim et al [6.4]. However this method suffers from the formation of multilayers along the surface, leading to inhomogeneity along the films of graphene. Furthermore strong interaction with the SiC substrate lead to breakdown of A-B sub-lattice symmetry leading to band gap opening at the K-point [6.9]. Klaus Mullen et al have used bottom up approach to synthesize graphene sheets which are in principle defect free however these methods are economically nonviable [6.10].On the other hand oxidation induced exfoliation has captured the attention of several groups due to their ability to produce these layer of GO in a large scale [6.11]. Furthermore, these samples can be processed by chemical reduction to obtain monolayer graphene [6.8].

In the present study our focus is on charge separation behavior in graphene QD nanocomposite. The graphene used is chemical reduced graphene oxide. Several previous have demonstrated previously that for an efficient photovoltaics employing QD one needs to separate charge carriers before trapping or recombination. This problem is particularly acute in case of QD due to larger surface to volume ratio [6.12]. Studies by Alivisatos et al [6.13] have demonstrated use to conducting polymers for charge separation which helps in improving photovoltaic effcicincy.

Kamat and coworkers [6.14] employing carbon nanotubes for charge separation for TiO_2 based photovoltaics have demonstrated an increase in efficiency.

Studies by Wang et. al. [6.15] and Cao et. al. [6.16] have demonstrated growth of quantum dots of CdS and CdSe on graphene and good steady state optical properties. Apart from this potential of graphene in improvement of photovoltaics effcicincy also has been demonstrated. quantum dots-graphene assembly also has shown potential application in photovoltaic measurements [6.17, 6.18]. Cao et al [6.16] have shown effcicint electron transfer from CdS QD to graphene from time-resolved emission spectroscopy.

To address this issue we have synthesized CdTe QD decorated on graphene and performed femtosecond transient absorption studies.

6.2. Experimental

6.2.1. Synthesis of Graphene Oxide

GO was synthesized from graphite by the modified Hummers method [6.19]. To 250 mL flask filled with graphite (2 g), 50ml H_2SO_4 was added at room temperature. Above solution was cooled to 0°C followed by addition of 7g of $KMnO_4$ slowly while maintaining the temperature below 10°C. After complete addition of $KMnO_4$, the temperature was increased to 10°C. The mixture was stirred for 2 h. Excess water was added into the mixture at 0°C (ice bath) and then H_2O_2 (30 wt% in water) was added until the effervescence ceases. The GO powder was washed with copious amount of water and dried in the ambient.

6.2.2. Reduction of Graphene Oxide

1gm of as prepared Graphene Oxide were dispersed in 1 litter of 1M NaOH and sonicated for 1 hour. This solution was cooled to 0°C. To this solution 2gm of $NaBH_4$ was added with vigorous stirring. This above solution was maintained at 0°C for 2h and heated to 50°C for 2h [6.20].

6.2.3. Synthesis of CdTe Decorated Graphene

The CdTe QDs were prepared by colloidal methods as reported earlier [6.21]. Briefly, 10 mmol of $CdCl_2$. $2.5H_2O$ was added to the above solution of reduced graphene (1g/l). To this, mercaptopropionic acid (MPA) was added with mole ratio of MPA:Cd = 2.4:1. The solution was then purged with nitrogen gas (N_2). The tellurium precursor NaHTe, was prepared by the reaction between $NaBH_4$ and tellurium powder in N_2 purged water at 0°C for 8 hours. Part of this solution was added to the Cd precursor solution with the ratio of Cd:Te = 1: 0.5. The above mixed solution was then refluxed for 4hours. The solution was then concentrated at reduced pressure by a Butchi Rotavapor to 1/3 of the original volume and isopropyl alcohol was added to the concentrated solution to precipitate the graphene-quantum dots composites. The collected composites were re-dissolved in nanopure water and precipitated with isopropyl alcohol, this process was repeated for 3 times to remove the precursors and clean the composites. Synthesis of CdTe quantum dots for the comparison of dynamics have been carried out by the same procedure as described above without the addition of exfoliated graphene in a 1M NaOH solution. The CdTe decorated samples will be referred to as G-CdTe

6.3. Results and Discussion

6.3.1. TEM Studies

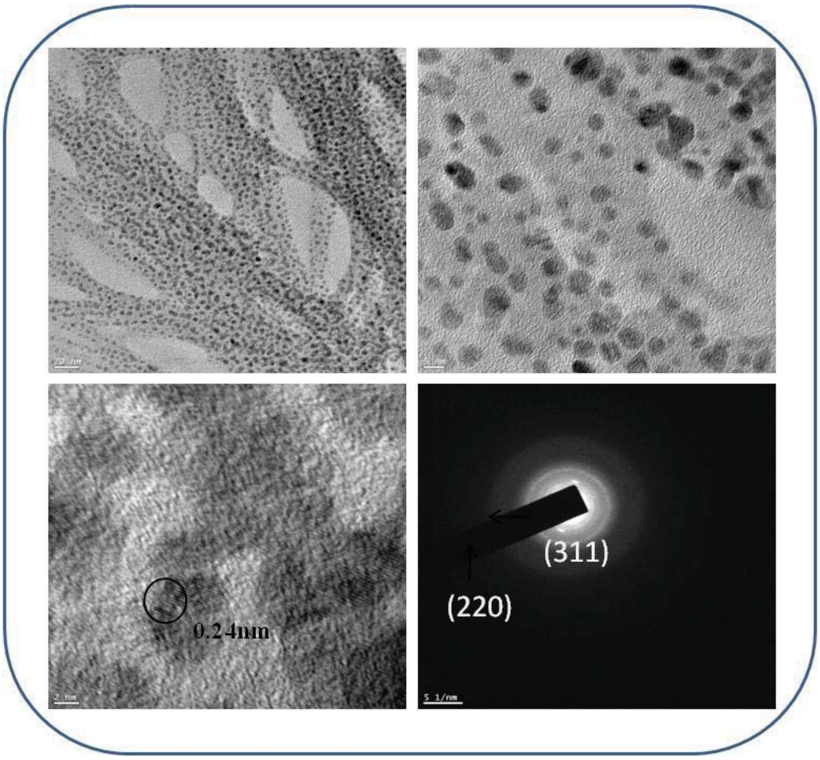

Figure 6.1. Transmission Electron Microscopy (High and Low magnifications) and Electron Diffraction of G-CdTe samples.

TEM images of are shown in Figure 6.1 shows the Transmission Electron Microscopy (TEM) images of G-CdTe samples. Images clearly indicate formation of predominantly isolated CdTe QD over graphene sheet. CdTe QD sizes are approximately 2nm. The lattice fringes in HRTEM images show a d-spacing of 0.24nm which matched well with (220) plane for cubic CdTe. SAED shows 2 rings which could be assigned to (220) and (311) planes of Cubic CdTe.

6.3.2. Steady State UV-Vis Absorption and Emission Studies

Figure 6.2 shows optical absorption spectra of CdTe and Graphene-CdTe (G-CdTe). The clear discerning feature in the spectrum is a band at 440nm for both the samples and is assigned to $1S_e$-$1S_{3/2}$ exciton. Since under the synthesis conditions the particles are spherical, the position of optical absorption feature can be used to arrive at a size of 2.2nm for quantum dot from sizing curves as reported previously [6.21]. This size obtained from optical absorption spectrum matches well with the size obtained from TEM. A closer look at the absorption spectra reveals a feature at ~300nm which matches well with the Graphene π- π^* absorption. The similar peak position of CdTe and G-CdTe clearly show that the sizes are similar for both. This observation enables us in a direct one to one comparison between CdSe and G-CdTe. The photoluminescence spectrum in figure 6.2 shows just a single feature in the visible region at 500nm illustrating similar particle sizes.

This emission is assigned to radiative recombination of the $1S_{3/2}$-$1S_e$ exciton. The peaks position for both the samples are ~500nm indicating the similar size of the quantum dots in both the cases confirming the conclusions based on optical absorption. The emission spectra from absorbance matched samples show a clear ~90% quenching of the G-CdTe emission as compared to pure CdTe. This observation could be an indication of electron transfer from CdTe to graphene on photoexcitation which will be confirmed later by femtosecond studies.

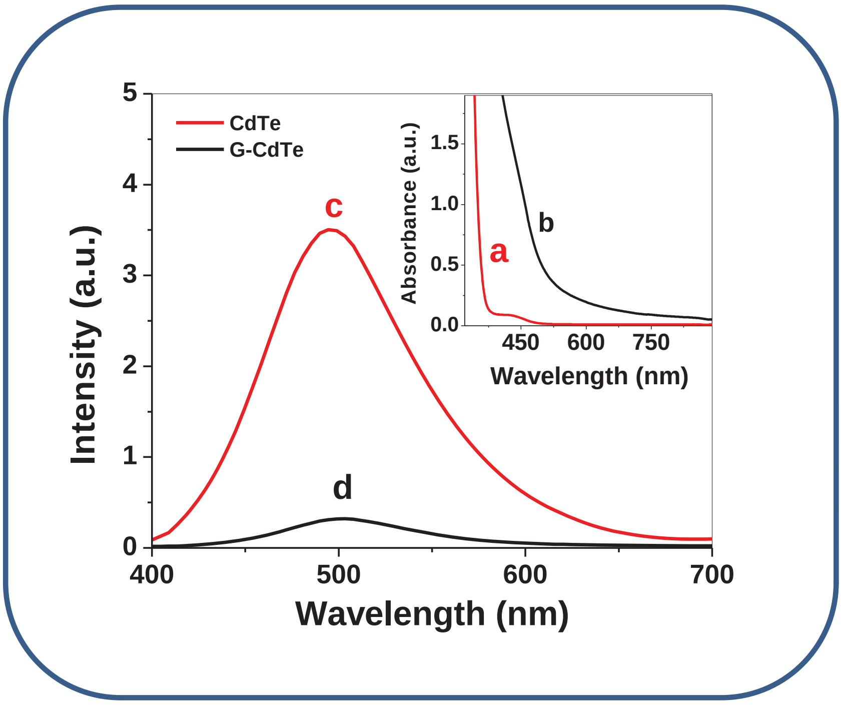

Figure 6.2: Photoluminescence Spectra of a) CdTe and b) G-CdTe after exciting the sample at 380 nm. Inset: optical absorption spectra of c) CdTe and d) G-CdTe.

6.3.3. TCSPC Studies

TCSPC studies was also carried out on G-CdTe by monitoring the peak position. Figure 6.3 shows the emission decay kinetics of CdTe in water and on graphene surface.

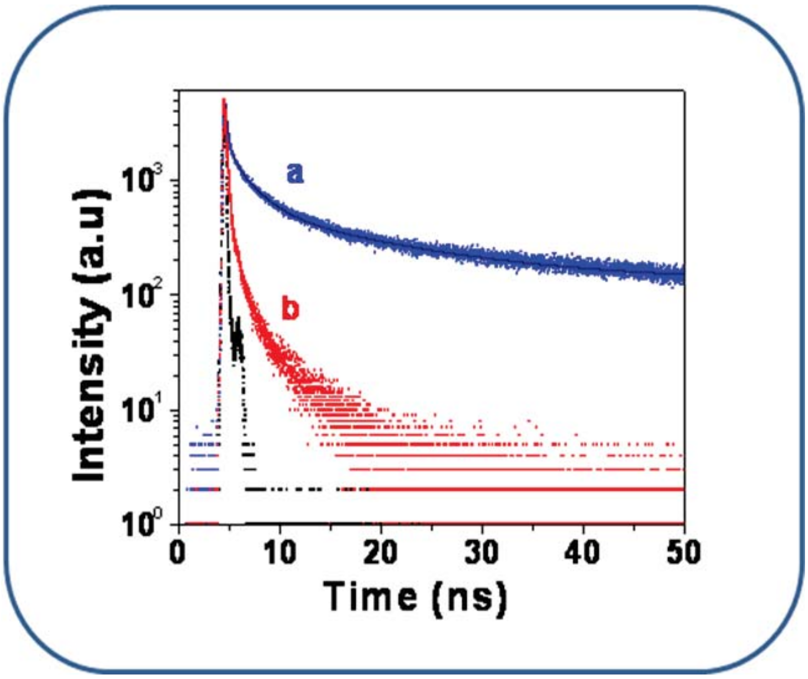

Figure 6.3: Time-resolved emission kinetics of a) CdTe and b) G-CdTe after exciting the sample at 400 nm.

The emission decay traces can be fitted multi-exponentially with time constants of τ_1= 0.27 ns (10.5%), τ_2= 2.3 ns (28.2%) and τ_3= 14.6ns (61.3%) and on graphene surface the emission kinetics can be fitted with time constants τ_1= 0.19 ns (57%), τ_2= 0.75 ns (25 %) and τ_3= 3.4 ns (18 %). The decay kinetics clearly show that on graphene surface the decay is much faster indicating an electron transferfrom QD to graphene.

6.3.4. Femtosecond Transient Absorption and Kinetics of Graphene Oxide and reduced graphene oxide

Graphene Oxide on photoexcitation at 400nm also can also show an electronic transition due to its high band gap arising due to oxygen incorporation. Therefore we investigated the dynamics of graphene oxide and reduced graphene after photoexcitation. The femtosecond spectra for graphene oxide are given in figure 6.4.

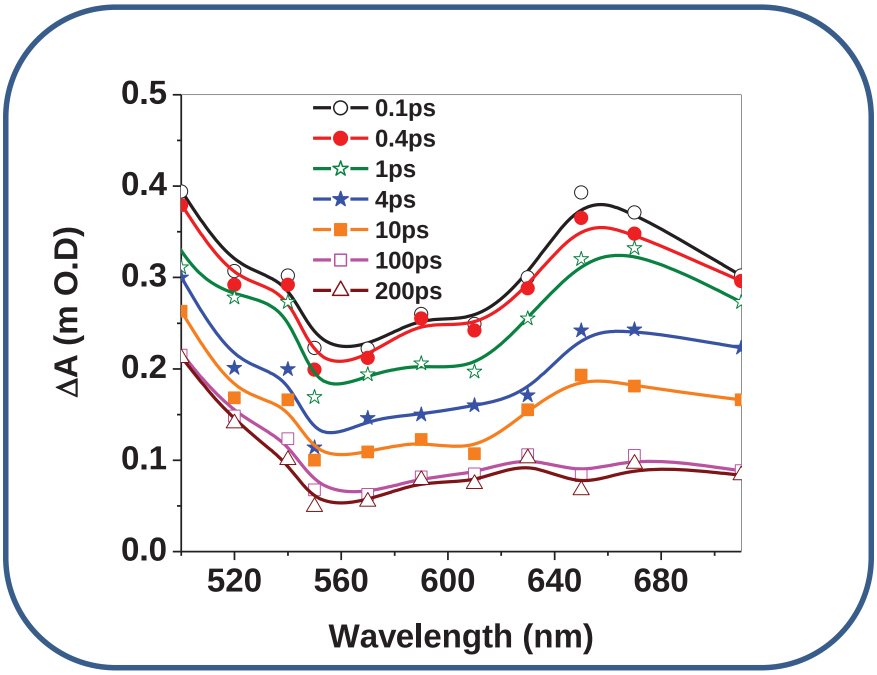

Figure 6.4. Transient absorption spectra of graphene oxide (GO) at different time delay after exciting 400 nm laser pulse.

The transient absorption spectra clearly show a broad absorption band in the entire visible region with a small peak at 670 nm, which can be attributed to the absorption due to trapped carriers. We have monitored the transient decay kinetics at 670 nm and shown in Figure 6.5. The transient data can be fitted multiexponentially with time constants of τ_1 = 0.9 ps (33.3%), τ_2 = 9 ps (38.5%), τ_3 = > 400 ps (28.2%). We have monitored transient kinetics at different wavelengths, but we did not observe any difference in dynamics. We have observed pulse-width limited rise of the transient signal which indicates the immediate formation of charge carriers on laser excitation. It is interesting to observe that a sizeable contribution (26.7%) of transient absorption signal does not decay beyond 400 ps.

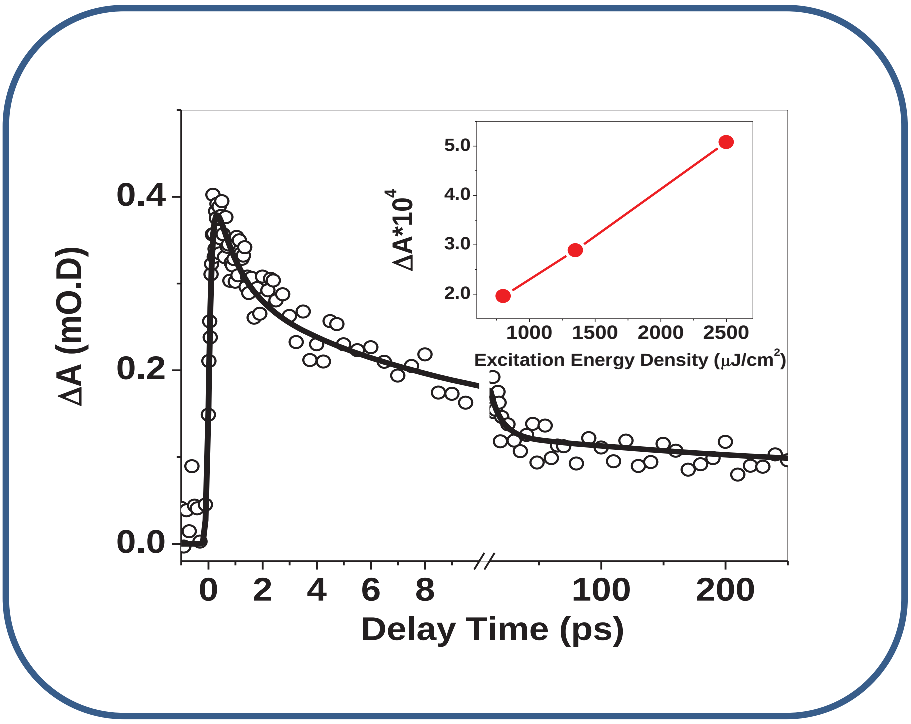

Figure 6.5: Transient decay kinetics of graphene oxide (GO) at 670 nm after exciting at 400 nm laser pulse. Inset: Absorbance change (Δ O. D.) graphene oxide (GO) at 670 nm at different excitation energy density (pump intensity).

This observation is in contrast to transient absorption signal of pure graphene as observed earlier [6.22]. Earlier studies on graphene or graphene oxide show ultrafast relaxation dynamics of photoexcited charge carriers with time constants ranging from ~ 100fs-2ps. So the slower decay time constants for transient signal observed in the present investigation might be due to slow recombination of the trapped charge carriers. Confirmation of this assignment is discussed in the later parts of this contribution. The dynamics at 670 nm for

GO as shown in the Figure 3 reveals a pulse width limited rise after excitation indicating the formation of the state within pulse-width time scale (< 50 fs). The relaxation of photoinduced charge carriers in the present investigation could due to a number of processes like carrier-carrier scattering, auger recombination, carrier-phonon relaxation or carrier trapping. It is reported in the literature [6.22] that the carrier-carrier interactions are complete within 30 fs in graphene. So it is reasonable to conclude that a quasi equilibrium state can be attained in photoexcited GO and subsequent relaxation process can take place with the mediation of optical phonons and which relax within a few picoseconds.

To ascertain the role of carrier-carrier interactions, we have carried out intensity dependence studies by monitoring the transient signal at 670 nm. The normalized signals showed an intensity independent kinetics which clearly indicates that the charge carrier dynamics does not depend on the carrier density. This observation excludes carrier-carrier interactions which have non trivial carrier density dependence (n^2 for carrier-carrier interaction and n^3 for Auger recombination, where n is the carrier density) [6.22-6.25] on lifetime. So from our observation we can safely conclude that carrier-carrier interactions are complete within the pulse width time (< 100fs) in the present studies. The shortest lifetime component (0.9ps) which contributes 33.3% to the relaxation may be assigned to a fast de-trapping. Majority (66.7%) of the transient signal still remain which has lifetimes of 9ps and >400ps. This suggests that unlike graphene on SiC, free GO in solution follows a different relaxation mechanism. Interestingly signal intensity of the photoinduced transient absorption signal was found to vary linearly with the intensity (Figure 6.5 Inset). In case of defect induced relaxation this is expected to saturate, but the possible reason for non saturation of intensity could be due to lower light intensity which is insufficient for saturation for transient absorption in the present studies. Plausible conclusion that one can make from the relaxation dynamics is that the charge carrier diffusion is hindered along the sheet due to the presence of trap sites, which facilitate energy relaxation by alternate pathways. Presence of surface (defect) states is further supported by recent STM study which showed that atomic arrangement in GO sheets composed of regions of graphene like hexagonal lattice separated by disordered regions composed of topological defects and oxidized parts [6.26]. This conclusion is further supported by electrical measurements which show hopping and tunneling mediated conductivity [6.27] in GO.

In our earlier investigations [28] the role of individual carriers in relaxation dynamics has been ascertained in quantum dots by use of electron/hole quenchers like quinones, pyridine, and amines. So we adopted a similar strategy to throw some light on the electron and hole contribution to the trapping dynamics. In the present study we have used benzoquinone (BQ) as electron quencher and pyridine (Py) as hole quencher to find out the contribution of trapped electrons and trapped holes in the transient signal, where the trapped carriers can be quenched completely or partially depending upon the trapped depth of the carrier. Earlier Charlier et al [6.29] have shown that carbon nano tube (CNT) can interact effectively with π –cyclic organic molecules although CNT surface has curvature. Charlier et al [6.29] probed the electronic interaction between CNT and different π –cyclic organic molecules like benzene and dichloro dicyano quinone (DDQ). In case of benzene-CNT system the interaction found to be weak as benzene physically adsorbed on CNT. However in case of CNT-DDQ system, DDQ acted like electron acceptor and CNT act as electron donor, which was evident from the formation of mid gap states in CNT+DDQ composite system. Benzoquinone with similar quinone structural unit, can act similar to DDQ as an efficient electron acceptor for Graphene. As GO is a planar surface both benzoquinone and pyridine are expected to interact with GO through π-ring of GO surface more effectively. In this condition it is expected that individual charge carriers will interact with the quenchers and will facilitate faster recombination with the complementary carriers. Figure 6.6 shows the transient decay for GO (trace a), GO in presence of electron quencher (benzoquinone, BQ) (trace b) and GO in presence of electron hole quencher (pyridine, Py) (trace c) at 670 nm.

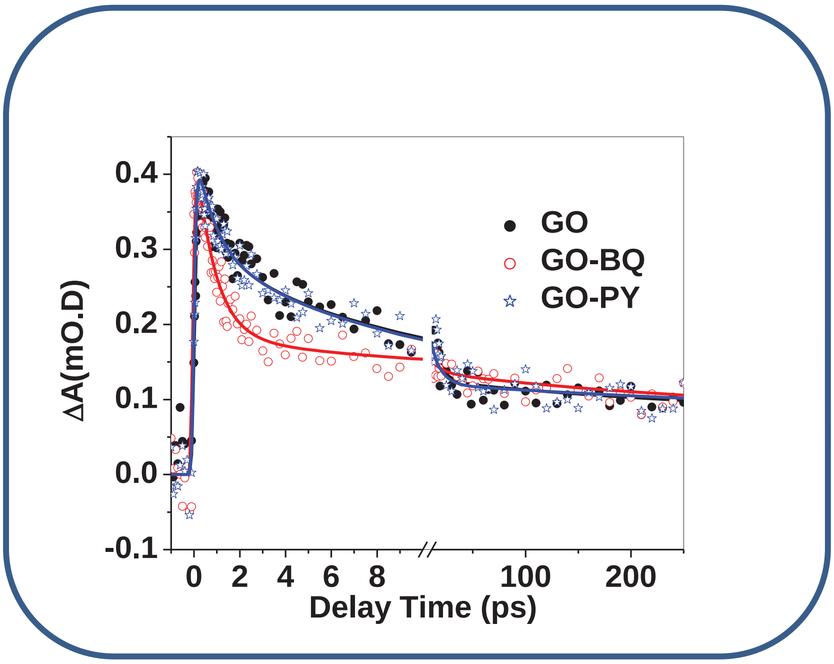

Figure 6.6: Transient decay kinetics of graphene oxide (GO) at 670 nm after exciting at 400 nm laser pulse in absence of any quencher (GO), in presence of electron quencher (GO-BQ) and in presence of hole quencher (GO-PY).

In presence of BQ the kinetic trace decays faster as compared to that of pure GO. The kinetics can fitted multiexponentially with time constants of τ_1 = 0.85 ps (61.8%), τ_2 = 10 ps (9.8%), τ_3 = > 400 ps (28.4 %) (Table 6.1). Additionally contribution of 0.9ps component increases from 33.3% to 61.8% in presence of BQ. However, the 9ps component show considerable decrease in contribution while >300ps component shows negligible changes.

Sample	τ_1(ps)	τ_2(ps)	τ_3(ps)
GO	0.9 ±0.2 (33.3%)	9 ± 2 (38.5%)	>300 (28.2%)
GO-PY	0.9 ±0.2 (33%)	9 ± 2 (39%)	>300 (28%)
GO-BQ	0.85 ±0.2 (61.8%)	10 ± 2 (9.8%)	>300 (28.4%)

Table 6.1: Life times of the transient absorption signal of graphene oxide at 670 nm after exciting at 400 nm laser light in absence of any quencher (GO), in presence of electron quencher (GO-BQ) and in presence of hole quencher (GO-PY).

From our experimental observation we can suggest that that BQ can interact with the photo-excited electron before trapping and can facilitate faster recombination, as a result we see that the reduction of 9 ps and > 400 ps components which are primarily attributed to trapped electrons in different trap depth. We have observed that the contribution of > 400 ps component has not been changed much from 28.2% (without BQ) to 28.4 % (in presence of BQ) which earlier was attributed to the component due to the deeper trapped states. So it clear that BQ cannot quench the electrons effectively which are deeply trapped in GO. This observation clearly ascertains the significant roles of electron traps in the relaxation dynamics of photoexcited charge carriers in chemically synthesized GO. However, in presence of hole quencher (Py) the kinetics at 670 nm of GO did not show any difference (Figure 6.6 c), which indicates that transient absorption mostly dominated by electron trap states. From the above investigation it is evident that trapping dynamics of charge carrier governs the recombination dynamics in GO, which in turn affect the suitability of the material as practical purposes. It is important to remove those defect states by reducing GO to reduced GO so that one can make it as a defect free material. It is important to ask how reduction procedure improves or more precisely, changes the carrier dynamics of the material? Does the charge carrier recombination dynamics becomes faster? Does it decrease the concentration of trap states? To answer all the above questions, we have reduced graphene oxide (GO) by following reported method [6.27]. We have prepared two different samples named as RGO-1 and RGO-2 where we have reduced the sample for 1h and 24h respectively as described in the Supplementary Information. Previous studies on reduction revealed that the reduction process is efficient only if the reduction time is 24h. To prove this we have prepared 1h reduction sample.

To further confirm the role of defects in relaxation dynamics we have carried out transient absorption studies of RGO-1 sample and compared the decay kinetics with GO at 670 nm. The decay kinetics was not influenced by intensity similar to GO. The kinetic data can be fitted multi-exponentially τ_1 = 0.70 ps (37%), τ_2 = 10 ps (36.5%), τ_3 = > 400 ps (26.5 %). Lifetime of and the contributions in RGO-1 remains almost identical (i.e. within the errors) as compared to that of GO. It is reported in the literature [6.30] that on reduction oxygen related defects of GO can be removed by a larger reduction time. To further ascertain the role of reduction processes we have reduced GO for 24 hours labeled RGO-2 which followed the reduction procedure generally used in the reduction of GO and carried out femtosecond transient absorption studies to monitor the charge carrier relaxation dynamics.

Figure 6.7 show the transient spectrum of RGO-2 at different time delay after exciting the samples at 400 nm laser pulse. The transient spectrum of RGO-2 looks significantly different as compared to that of GO. It is clearly seen that transient signal intensity increases dramatically in RGO-2 as compared that of GO. Transient spectrum broad absorption in the visible region (500 nm to 700 nm) shows higher absorption in the blue region of the spectrum. Furthermore the broad feature at 670nm is significantly reduced indicating that this feature might come from oxygen related trap state absorptions. We have monitored the transient decay kinetics at 670 nm and shown in inset of Figure 6.7.

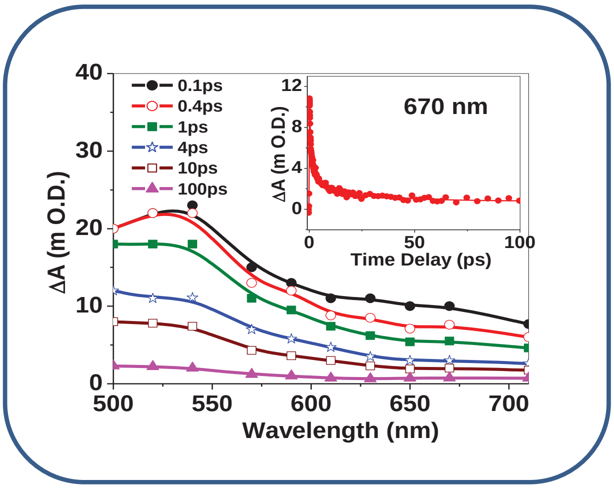

Figure 6.7: Transient absorption spectra of reduced (24 hours) graphene oxide (RGO-2) at different time delay after exciting 400 nm laser pulse. Inset: Transient decay kinetics at 670 nm.

The transient data can be fitted multiexponentially with time constants of τ_1 = 0.26 ps (65%), τ_2 = 2.5 ps (24.5%), τ_3 = 30 ps (6.5%), τ_4 = >400 ps (4%) (Table 6.2).

Sample	τ_1(ps)	τ_2(ps)	τ_3(ps) + τ_4(ps)
GO	0.9 ± 0.2(33.3%)	9 ± 2 (38.5%)	>300 (28.2%)
RGO-1	0.7 ± 0.2 (37%)	10 ± 2 (36.5%)	>300(26.5%)
RGO-2	0.26 ± 0.1 (65%)	2.5 ± 0.5 (24.5%)	30 ±5 (6.5%) + >300 (4%)

Table 6.2: Life times of the transient absorption signal of graphene oxide (GO), reduced (1 hour) graphene oxide (RGO-1) and reduced (for 24 hours) graphene oxide (RGO-2) and at 670 nm after exciting at 400 nm laser light.

It is clear that the transient signal decay significantly faster as compared to that of GO. The faster two lifetimes components (0.26ps and 2.5ps) contribute almost 90% to the relaxation process, which indicates a significant percolation in GO from sp^3 to sp^2 carbon.

The first two components matches with excited dynamics of photo-excited graphene as measured in earlier reports. These fast components have been assigned to the relaxation by electron-phonon interactions. It is reported in the literature [6.31] that carrier relaxation process in graphite are hindered by accumulation of hot phonons at higher carrier density which is called hot phonon bottleneck effect as a result one can see slower component in the relaxation dynamics. Kamfrath et al. [6.32] measured 2.5 ps component of carrier relaxation dynamics in photo-excited graphite phonon mediated relaxation. In the present studies the slower 0.26ps and 2.5 ps can be attributed interactions with optical and acoustic phonons respectively. However in the decay kinetics of RGO-2, we can still observe ~ 4% contribution >400ps component. In case of transient decay analysis of GO we have explained that >400 ps component arises due to deep trap states. We can see clearly see that on reduction of GO to RGO-2 the contribution of 30ps and >400 ps component. These components could come from traps still present after reduction [6.26]. Our ultrafast study clearly shows that RGO-2 still contains a reasonable amount of defect states.

6.3.5. Femtosecond Transient Absorption of CdTe Quantum Dot Decorated Reduced Graphene Oxide

In line with the emission study we conduct further analysis by monitoring the dynamics by femtosecond transient absorption measurements to better understand the charge transfer dynamics after 400 nm excitation. Fig. 6.8 shows the transient absorption spectra of CdTe and G-CdTe nanocomposites for varying time delays. The spectra comprises of a bleach <500nm for CdTe samples and <550nm for G-CdTe nanocomposites. Also it shows a presence of broad induced absorption feature for the other wavelengths for both the samples. We ascribe the bleach feature to the first exciton of the CdTe.

The complete bleach assigned to exciton envelope cannot be mapped as the generation of white light was poor in this region. This bleach could be attributed to state filling transitions as the position matches well with our absorption study. This conclusion is backed by the fact that $N = j\sigma = 0.1 (\ll 1)$, therefore contribution of biexciton and stark effect can be ruled out. This is also evident from absence of derivative like feature in the transient spectra [6.33]. The bleach in the case of CdTe mostly arises from electron due to much higher effective mass of the electron as compared to the hole and greater degeneracy of the valence band. Therefore the bleach dynamics that we monitor mostly pertains to electron dynamics [6.33, 6.34].

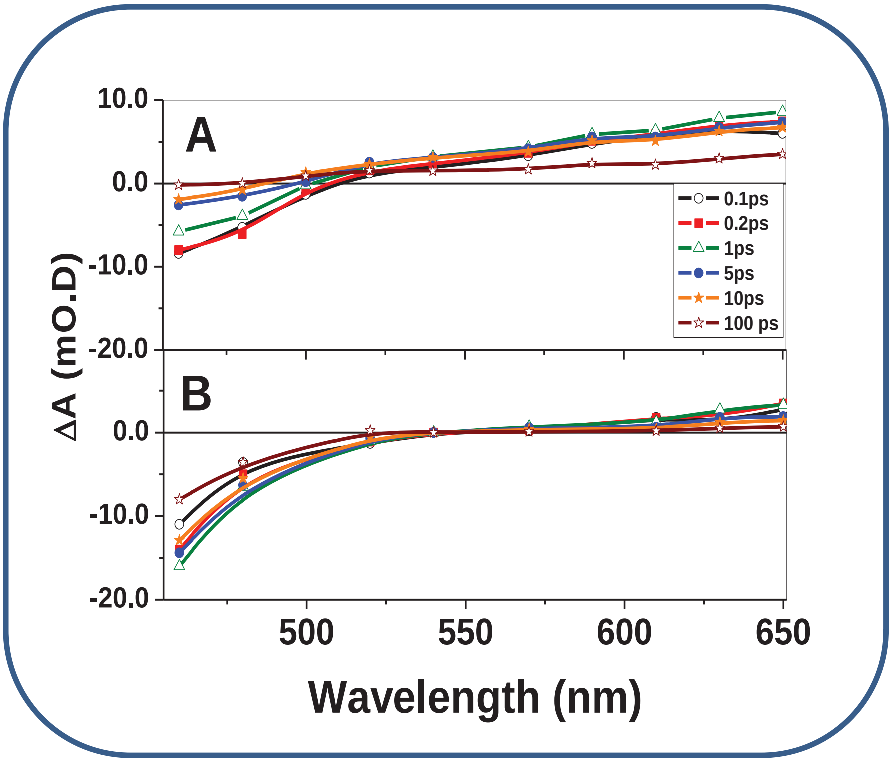

Figure 6.8. Femtosecond Transient absorption spectrum at different time delays for CdTe (a) and G-CdTe (b) after excitation at λ_{pump}=400nm.

The dynamics as shown from transient absorption spectra reveals that on comparison with CdTe quantum dot, the relaxation is much delayed in the case of G-CdTe composites revealing the significant role played by Graphene in the relaxation dynamics in G-CdTe. As discussed earlier the bleach has a significant component arising from the electron in the case of CdTe. Therefore we can conclude that the delayed dynamics in the case of G-CdTe is clearly due to an electron transfer into graphene on photoexcitation of CdTe quantum dots. This observation clearly indicates that Graphene can act as an electron relay which enables an efficient charge separation. The photoinduced absorption beyond 550nm in the present case may be possibly due to carrier trap states [6.34]. Additionally the features that are observed in case of G-CdTe nanocompostes are different from reduced graphene oxide.

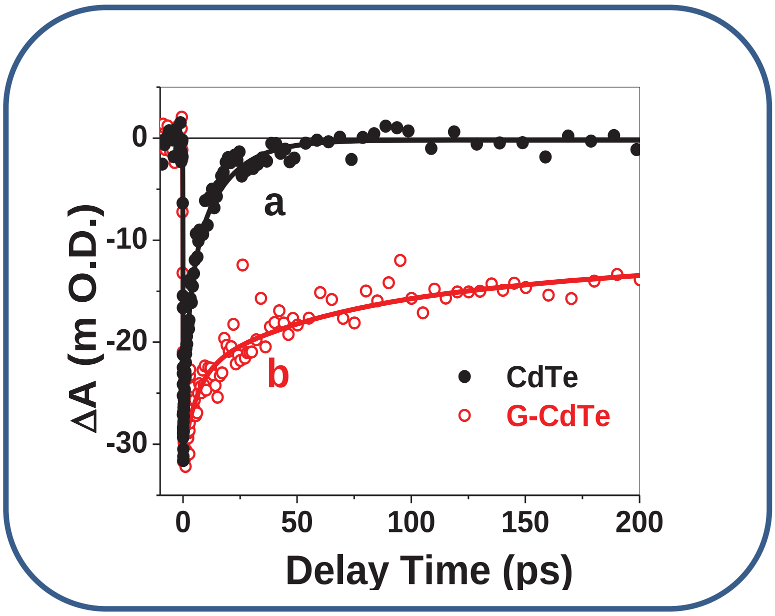

Figure 6.9: Bleach recovery kinetics at 460 nm for a) CdTe and b) G-CdTe after 400 nm laser excitation.

The bleach dynamics measured at 460nm is plotted in figure 6.9. The bleach recovery kinetics reveals significantly different dynamics for the two samples. As previously noted in the literature the relaxation of bleach is governed by both radiative and nonradiative contribution [6.33]. The radiative contributions mostly arise from exciton recombination in thiol capped CdTe with lifetimes in the range of ns. However nonradiative relaxation arising from trap state related contributions governs the faster time scale relaxations. Previous studies by our group [6.34] on CdTe clearly differentiated the contribution of electron and hole traps on relaxation dynamics. Since the bleach contains significant contribution from electrons it is safe to assume that the relaxation dynamics is governed by electron trapping as previously pointed out by Klimov et al [6.33, 6.35] on CdSe. The different time constants involved in the relaxation may come an ensemble average (arising from size distribution or different types of defects) or from a single QD behavior [6.33].

The initial time constant in the case of CdTe is ~1.7ps this relaxation is mostly likely related to a relaxation to a defect within the band gap and if this lifetime corresponds to a single quantum dot behavior then the relaxation of the bleach will be completely dominated by the trapping event with lifetime of ~1.7ps. Since this is not observed and we also have very slow relaxing component, we can safely conclude that the relaxation is multiexponential because of several type of defects forming states within the band gap and aiding in relaxation of the quantum dots. Comparing the QD samples with G-CdTe clearly show a significant slower relaxation of the bleach. Since the sizes of the quantum dots are same in both of the cases a one to one comparison is directly possible between the two samples.

Sample	**CdTe (ps)**	**G-CdTe (ps)**
τ_1 (%)	**1.7(41.2)**	**6(25.4)**
τ_2 (%)	**12(58.8)**	**50(20.2)**
τ_3 (%)	**-**	**>200(54.4)**

Table 6.3. Fits of the time traces monitored at 460nm (Exciton Bleach).

The fits to bleach as shown in the table 6.3 are ~200fs for both the samples. The bleach formation of lowest exciton in quantum dots after a 400nm excitation populates carriers deep into the individual bands and therefore rise time of the bleach contains information on cooling dynamics of the carriers [6.24].

The cooling dynamics does not show much variation between the two samples and is more or less pulse width limited, therefore indicating a very fast cooling process. The recombination dynamics that is monitored from the bleach indicates the electron recombination occurring after the donation of electron into graphene for G-CdTe samples, i.e. after the formation of lowest exciton state. The relaxation dynamics shows that the dynamics is multiexponential revealing the role of several traps states in relaxation. In the case of G-CdTe we find that the relaxation is much slow with significant contribution coming from very slow components (>200ps, 54.4%) beyond the time delay of our instrument hinting at efficient charge separation in present system. Comparing this with CdTe QD, we find that the dynamics is biphasic and with relaxation completely over within 12ps lifetime. Our previous studies on size dependent dynamics indicated a faster relaxation dynamics for smaller nanocrystals. This size dependent dynamics was assigned to relaxation from the increased traps states on the surface of smaller quantum dots. This observation is also supported by previous literature studies on CdSe by Klimov et al [6.33, 6.35]. Therefore a drastic increase in the lifetime of G-CdTe is a clearest indication of an efficient charge separation before trapping on the surface. Evidence of which also comes from luminescence measurements where we observed a ~90% reduction in the luminescence intensity for G-CdTe as compared to CdTe. As the bleach formation and recovery kinetics is dominated by electrons due to higher degeneracy of the valence band and lower electron mass as compared to holes, the bleach dynamics exclusively monitors the electron dynamics. Therefore we can conclude that the relaxation in G-CdTe is delayed due to charge transfer. To gain further insight into the charge transfer dynamics we study the dynamics in the presence of an electron quencher.

Electron quencher (benzoquinone in this case) leads to a fast separation of electrons from the conduction band. Since the smaller quantum dots have significant surface area due to smaller radius, the diffusion of the electrons to the surface is expected to take place within the pulse width. Therefore the probability of quenching is expected to be high. Our previous studies in fact demonstrate this by monitoring the formation of the lowest exciton state or cooling dynamics. For quenching studies the concentration of the quencher is ~100 times the concentration of QD therefore it is expected for the electron quenching to be efficient. In the present case there is a drastic quench of the bleach in the presence of the electron quencher (>50%), Since the quenching is expected to be complete and relaxation on quenching gives only the slower recombination components we can safely conclude by comparing the dynamics in the presence and absence of quencher that the slow lifetime component comes from the recombination of the electron injected in graphene after the photoexcitation of the QD. The studies in the presence of quencher in this case only an electron quencher were used as we are monitoring the bleach which contains information on the electron dynamics.

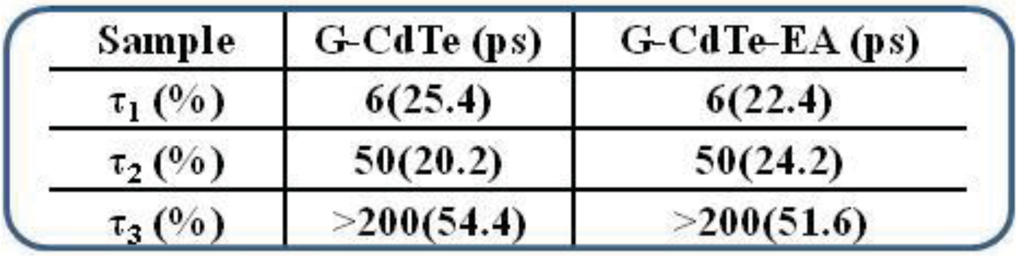

Sample	G-CdTe (ps)	G-CdTe-EA (ps)
τ_1 (%)	6(25.4)	6(22.4)
τ_2 (%)	50(20.2)	50(24.2)
τ_3 (%)	>200(54.4)	>200(51.6)

Table 6.4. Fits of the time traces monitored at 460nm (Exciton Bleach in presence of electron quencher).

The study clearly shows that the dynamics in the presence of quencher is more or less same as shown in the table 6.4. Previous studies by our group and others have reported the effect of benzoquinone on quantum dot dynamics. The results of these have unambiguously verified the role of benzoquinone as an electron shuttler on the surface of CdSe and CdTe quantum dot. Benzoquinone accepts the electron within the pulse width and BQ anion situated on the surface donates the electron back to the valence band hole within few ps. However in the present study we observe quenched bleach in the presence of quenchers indicating electron quenching. However the bleach recovery is dominated by the electrons that are not quenched by benzoquinone and they show negligible effect on the dynamics. These are the electrons which have been injected into Graphene. This is clear from the lifetime contributions which show that the lifetime and contribution are approximately the same. This further ascertains the role of electron injection into Graphene in G-CdTe. Furthermore the dynamics of the bleach also does not arises from Graphene as previously we have shown that the reduced Graphene oxide (Pump-400nm) dynamics gives a positive absorption in this wavelength range as compared to a bleach in the present cases.

These experimental observations are summed up in the schematic given in Scheme 1. The CdTe E_{VB} and E_{CB} are -5.2eV and -3.5eV with respect to vacuum.

We have obtained the position from fits equation obtained from tight binding calculations as reported previously [6.37]. The expressions for the valence and conduction band shift with respect to diameter of the quantum dots are given below,

$$\begin{aligned} E_{VB} &= E_{VB}^{Bulk} - \frac{19.03}{d^{1.13}} \\ E_{CB} &= E_{VB}^{Bulk} + \frac{16.38}{d^{0.92}} \end{aligned} \tag{6.1}$$

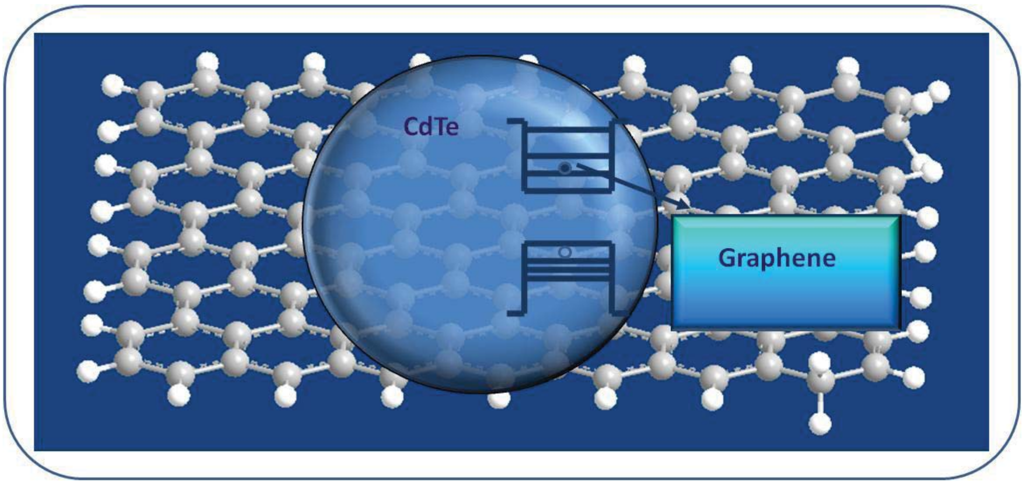

Scheme 6.1. Schematic of Electron Transfer Process

The positions of the valence and conduction band are ~-5.8 and -2.6 respectively. The Fermi level of graphene is -4.5eV. Band alignment is such that the Fermi level of graphene is much lower compared to the conduction band of CdTe, leading to a highly negative free energy for electron transfer (ΔG~-1eV). Therefore graphene similar to metal nanoparticles can act as an electron sink. This has been verified by the present study by use of luminescence spectroscopy and transient absorption technique.

6.4. Conclusions

In conclusion we state that we have synthesized and studied ultrafast charge carrier dynamics of Graphene-CdTe (G-CdTe) system and compare the dynamics with CdTe of same size synthesized by colloidal methods. TEM studies confirmed formation of CdTe over graphene. UV-Visible absorption indicated the sizes of quantum dots as ~2.2nm. The sizes of CdTe were found to be the same as observed by $1S_{3/2}$-$1S_e$ first exciton band postion at 450nm.

From emission studies both steady state and time resolved revelaed charge separation in presence of graphene. Charge separation behavior as studied by monitoring lowest exciton bleach revealed an enhanced recombination time as compared to pure CdTe QD by transient absorption spectroscopy. The exciton recombination in the case of CdTe was complete within 50ps while dynamics in G-CdTe was found to be very slow with the longest lifetime component >400ps clearly indicating much better charge separation the case of G-CdTe nanocomposites. Studies on carrier quenching using benzoquinone (electron quencher) revealed a quench in the bleach signal with negligible change in lifetimes and their contributions indicating this recombination contribution actually comes from electron transferred to Graphene.

6.5. References

6.1. Geim, A. K. and Novoselov, K. S., Nature Mater., **2007**, *6*, 183.

6.2. Novoselov, K. S., A. K. Geim, S. V. Morozov, D. Jiang, Y. Zhang, S. V. Dubonos, I. V. Gregorieva, and A. A. Firsov, Science, **2004**, *306*, 666.

6.3.Berger, C.; Song, Z.; Li, T.; Li, X.; Ogbazghi, A. Y.; Feng, R.; Dai, Z.; Marchenkov, A. N.; Conrad, E. H.; First, P. N.; and Heer, W. A. De., J. Phys. Chem. B, **2004**, *108*, 19912.

6.4. Novoselov, K. S., A. K. Geim, S. V. Morozov, D. Jiang, M. I. Katsnelson, I. V. Grigorieva, S. V. Dubonos, and A. A. Firsov, Nature, **2005**, *438*, 197.

6.5. Katsnelson, M. I.; Novoselov,K. S.; Geim, A. K., Nature Physics, **2006**, *2,* 620.

6.6. Reina, A.; Jia, X.; Ho, J.; Nezich, D.; Son, H.; Bulovic, V.; Dresselhaus, M.; Kong, J., Nano Lett. **2009**, *9*, 30.

6.7. Hass, J., Feng, R.; Millán-Otoya, J. E.; Li, X.; Sprinkle, M.; First, P. N.; de Heer, W. A.; and Conrad, E. H., Phys. Rev. B, **2007**, *75*, 214109.

6.8. Li, D.; Mueller, M. B.; Gilje, S.; Kaner, R. B.; and Wallace, G. G. Nature Nanotech., **2008**, *3*, 101.

6.9. Zhou, S. Y.; G.-H. Gweon, A. V.; Fedorov, P. N.; First, W. A.; de Heer, D.-H.; Lee, F.; Guinea, A.; Castro Neto, H.; and Lanzara, A., Nature Mater., **2007**, *6*, 770.

6.10. Xiaoyin Yang, Xi Dou, Ali Rouhanipour, Linjie Zhi, Hans Joachim Rader, and Klaus Mullen, J. Am. Chem. Soc., **2008**, 130, 4216.

6.11. Hummers, W. S. Jr; and Offeman, R. E. J. Am. Chem. Soc., **1958**, *80*, 1339.

6.12. A. P. Alivisatos, Science, **1996**, 271, 933.

6.13. W. U. Huynh, J. J. Dittmer and A. P. Alivisatos, Science, **2002**, 295, 2425.

6.14. A. Kongkanand, R. M. Domínguez, and P. V. Kamat, Nano Lett., **2007**, 7, 676.

6.15. Y. Wang, H. –B. Yao, X. –H. Wang and S. -Hong Yu, J. Mater. Chem., **2011**, 21, 562.

6.16. A. Cao, Z. Liu, S. Chu, M. Wu, Z. Ye, Z. Cai, Y. Chang, S. Wang, Q. Gong, Y. Liu, Adv. Mater., **2010**, 22, 103.

6.17. Y. Lin, K. Zhang, W. Chen, Y. Liu, Z. Geng, J. Zeng, N. Pan, L. Yan, X. Wang and J. G. Hou, ACS Nano, **2010**, 4, 3033.

6.18. C. X. Guo, H. Bin Yang, Z. M. Sheng, Z. S. Lu, Q. L. Song, C. M. Li, Angew. Chem. Int. Ed., **2010**, 49, 3014.

6.19. Kovtyukhova, N. I.; Ollivier, P. J.; Martin, B. R.; Mallouk, T. E.; Chizhik, S. A.; Buzaneva, E. V.; Gorchinskiy, A. D.; Chem. Mater.**1999**, 11, 771.

6.20. Hyeon-Jin Shin, Ki Kang Kim, Anass Benayad, Seon-Mi Yoon, Hyeon Ki Park, In-Sun Jung, Mei Hua Jin, Hae-Kyung Jeong, Jong Min Kim, Jae-Young Choi, Young Hee Lee, **2009**, 19, 1987.

6.21. A. L. Rogach, T. Franzl, T. A. Klar, J. Feldmann, N. Gaponik, V. Lesnyak, A. Shavel, A. Eychmuller, Y. P. Rakovich and J. F. Donegan, J. Phys. Chem. C, **2007**, 111, 14628.

6.22. Wang, H.; Strait, J. H.; George, P. A.; Shivaraman, S.; Shields, V. B.; Chandrashekhar, Mvs.; Hwang, J.; Rana, F.; Spencer, M. G.; Ruiz-Vargas, C. S.; and Park, J. *Appl. Phys. Lett.* **2010**, *96*, 081917 (1-3).

6.23. Libai Huang, Gregory V. Hartland, Li-Qiang Chu, Luxmi, Randall M. Feenstra, Chuanxin Lian, Kristof Tahy and Huili Xing, *Nano Lett.*, **2010**, *10*, 1308-1313.

6.24. Gao, B.; Hartland, G.; Fang, T.; Kelly, M.; Jena, D.; Xing, H. G.; and Huang, L. *Nano Lett.* **2011**, *11*, 3184-3189.

6.25. Ruzicka, B. A.; Werake, L. K.; Zhao, H.; Wang, S.; and Loh, K. P. *Appl. Phys. Lett.* **2010**, *96*, 173106 (1-3).

6.26. Kaiser, A. B.; Navarro, C.G-; Sundaram, R. S.; Burghard, M.; and Kern, K., *Nano Lett.*, **2009**, *9*, 1787-1792.

6.27. Sungjin Park & Rodney S. Ruoff, *Nature Nanotechnology* **2009**, *4*, 217-224.

6.28. Sreejith, K.; Rawalekar, S.; Verma, S.; and Ghosh, H. N. *Phys. Chem. Chem. Phys.*, **2010**, *12*, 4210-4216.

6.29. Tournus, F.; Latil, S.; Heggie, M. I.; and Charlier, J.-C., *Phys. Rev. B*, **2005**, *72*, 075431 (1-5).

6.30. Tung, V. C.; Allen, M. J.; Yang, Y.; Kaner, R. B., *Nat. Nanotech*. **2009**, *4*, 25-29.

6.31. Gao, B.; Hartland, G.; Fang, T.; Kelly, M.; Jena, D.; Xing, H. G.; and Huang, L. *Nano Lett.* **2011**, *11*, 3184-3189.

6.32. Kamfrath, T.; Perfetti, L.; Schapper, F.; Frischkorn, C.; and Wolf, M. *Phys. Rev. Lett*. **2005**, *95*, 187403 (1-4).

6.33. Victor I. Klimov, J. Phys. Chem. B, 2000, 104, 6112.

6.34. Sreejith Kaniyankandy, Sachin Rawalekar, Sandeep Verma, Dipak K. Palit and Hirendra N. Ghosh, Phys. Chem. Chem. Phys., 2010, 12, 4210.

6.35. V. I. Klimov and D. W. McBranch, C. A. Leatherdale and M. G. Bawendi, Phys. Rev. B 60, 13740 (1999).

6.36. S. Sapra and D. D. Sarma, Evolution of the electronic structure with size in II-VI semiconductor nanocrystals, Phys. Rev. B, **2004**, 69, 125304(1-7).

CHAPTER 7

Summary and Outlook

7.1. Thesis Summary

The premise of the thesis is to better understand carrier dynamics in QD based nanostructures. In the present thesis we have investigated dynamics in TiO_2 and II-VI QD nanostructures. The dynamics investigated in most cases include cooling, trapping and recombination of carriers. Synthesis of QD nanostructures is a major part of the present thesis. The synthesized QDs were characterized by X-Ray diffraction, transmission electron microscopy, electron diffraction, optical techniques etc. Charge carrier dynamics were studied by time correlated single photon counting and ultrafast transient absorption spectroscopy. Details of the studies carried out in the present thesis are described in chapters 3-6. The conclusion formed out of these studies is described below.

Focus of the work described in chapter 3 is on effect of particle size on interfacial electron transfer dynamics from alizarin to TiO_2. Alizarin binds strongly to TiO_2 surface and has been shown to sensitize TiO_2. The binding of alizarin leads to broadening of absorption of TiO_2 which indicated a strong covalent interaction. On photoexcitation with 400nm, alizarin transfers electron to TiO_2 conduction band. The electron transfer dynamics was compared to bulk TiO_2 as control. Electron injection was found to be multiexponential injection in contrast to monoexponential ultrafast injection in bulk TiO_2. Aggregation and multilayer formation as the reason for observation of multiple injection components were ruled out as concentration of the dyes was low. Multiexponential injection components were assigned to injection into different discrete levels in the CB. The multiexponential injection indicated possibility of a nonadiabatic electron transfer process. The injections times were ~<100fs, 17fs and 50fs. Furthermore, the BET dynamics was considerably slower on the ultrasmall TiO_2 as compared to bulk TiO_2 system. The slower BET compared to bulk TiO_2 was explained as arising from increased free energy due to upward shift of the conduction band levels and also its discrete nature. The observations were as expected from Marcus theory, where in the inverted regime BET rate decreases with free energy. Observation of multiple injection components in a strong binding dye like alizarin is noteworthy as ET is expected to be adiabatic in the case of alizarin-TiO_2 system.

Work described in chapter 4 is centered on influence of size on relaxation behavior of cubic CdTe QDs. The CdTe QDs were synthesized by colloidal route as previously reported and characterized by optical techniques. Four different sizes of QDs were synthesized for this study. The dynamics in each of the cases were studied mainly at the bleach wavelengths of the first excitons after photoexcitation at 400nm by transient absorption spectroscopy. The transient absorption spectroscopy revealed in general bleach at exciton position as observed in steady state absorption and broad photoinduced absorption arising from traps. The growth times of 1st exciton bleach correspond to cooling times of carriers due to state filling. The comparison of rise time revealed an increase in cooling times with sizes. This observation ruled out possibility of multi phonon emission mechanism as the cooling mechanism observed in the present study. Possibility of involvement of e^--h energy transfer (2-body Auger mechanism) was verified by use of quenchers in largest CdTe QD used (Diameter=3.2nm). The addition of quenchers varied bleach growth times indicating involvement of e^--h energy transfer in cooling. For eg addition of hole quencher increases bleach growth times from 500fs to 700fs. Furthermore involvement of surface on relaxation was confirmed by comparing decay time (~3ps-~90%) of the 2nd exciton (monitored at 530nm) and growth time (~500fs) of first exciton (monitored at 590nm) of the largest sample (Diameter=3.2nm). The broad induced absorption observed at red side of bleach from visible to NIR region arises from traps. Analysis of photoinduced absorptions correspond to trapping and detrapping of carriers. Contribution of different lifetimes to electrons and holes were assigned on the basis of quenching studies.

Chapter 5 deals with charge carrier dynamics in a staggered aligned CdSe/ZnTe core shell. The CdSe core samples were synthesized by colloidal methods. CdSe core samples were cleaned and fixed concentration of core samples were further used for shell growth. The shell growth was carried out at lower temperatures to avoid homogeneous nucleation. Four core shell samples were synthesized. The samples were characterized by XRD, TEM and optical techniques. The formation of shell was confirmed by HRTEM and red shift in optical absorption. Additional evidence of formation was obtained by reduction in traps state emission from thiol related traps in CdSe and concomitant formation of exciton emission in core shell samples. TCSPC analysis of emission decay kinetics revealed decrease in faster components and increase in slower decay components. Furthermore core and core shell samples an increase in average lifetimes as measured at exciton positions confirmed the observation of a staggered aligned interface in the core shell system. Femtosecond transient absorption spectra revealed bleach and induced absorption. The induced absorption is much reduced in core shell samples as compared to core samples indicating reduction in traps on shell formation. Additionally dynamics monitored at bleach positions showed increase in cooling times as revealed by monitoring bleach growth times. This confirmed ultrafast hole transfer from CdSe core to ZnTe shell. This study further highlighted the importance of having a proper interface in enabling an efficient transfer of charges.

Aim of the work described in the chapter 6 is to investigate role of graphene in charge separation from a QD. We chose chemically synthesized reduced graphene oxide as the template to decorate it with CdTe QDs. The samples were characterized by XRD, HRTEM and optical techniques. Since graphene oxide and reduced graphene oxide is also known to absorb 400nm light we also studied their dynamics as control. Our analysis of relaxation dynamics revealed involvement of phonon and trap states. Involvement of electrons traps in relaxation dynamics was ascertained by use of quenchers. Furthermore long time component observed in relaxation were still present after reduction procedure indicating presence of traps. However we observed a dramatic decrease in traps with higher reduction time. The dynamics of 24h reduced Graphene oxide was found to be close to previous reports on pristine graphene. The CdTe decorated graphene was synthesized by colloidal methods and characterized. The TCSPC studies and transient absorption studies confirmed an efficient charge separation.

7.2. Outlook

Focus of the present is on investigation of charge carrier dynamics in confined systems with particular emphasis on charge separation behavior. Insights on how charge carrier dynamics in QD is mediated by different factors like surface, carrier interactions etc have been drawn from dynamics measurements. Major conclusion of the present thesis is on tunability of charge transfer properties by creation of heterostructures by simple synthesis modifications of a QD.

Study of interfacial electron transfer dynamics revealed a better charge separation behavior in a confined system. There is still scope for doing further research in this area. The possibility of variation in dynamics by varying the size of TiO_2 remains unexplored. How much such smaller TiO_2 can improve the actual photovoltaic efficiency is a question that needs to be explored.

The next chapters describe dynamics in QDs and QD based heterostructure. In chapter 4 we have studies the dynamics in CdTe QD. The main inferences drawn indicate significant size dependent dynamics. In fact in smaller QD the recovery at bleach was found to be much faster as compared to larger QD. This indicates significant role played by surface. Previous study on QD using TOPO or oleic acid capping showed relaxation in time scales of ns. This hints at the role of capping agent and crystallinity in relaxation. Therefore synthesis of good crystalline QD with better surface capping agent needs to be investigated. This might help in overcoming the drawbacks arising from trapping of carriers. This is also true in case of CdSe/ZnTe core shell QD. Here our purpose was to investigate charge transfer time. The results of this study were promising and it warrants further exploration. The characteristics of the interface are one of the areas one needs to investigate. The formation of a shell forms an interface between two different materials. This leads to a lattice mismatch which could lead to formation of defects along the interface. The types of defects and its energetics is an area which needs careful attention. Additionally the lattice mismatch for small shell thickness could lead to a strain close to the interface on core and shell. This is also known to affects band alignment at the interface. Therefore knowledge of band alignment is of utmost importance. Studies have shown role of cyclic voltammetery in obtaining band positions.

However the position of bands in a buried interface requires more advanced instrumentation like ultraviolet photoelectron spectroscopy.

Our study on charge separation in CdTe decorated graphene has shown how a heterostructure with good electronic contact can be used for an effcicient charge separation. The studies actually show the dynamics to be multiexponential which indicates that several factors contribute to relaxation. Further studies to explore role of different processes involved in the relaxation is required.

Possible areas of explorateation are necessary to better understand charge carrier dynamics in QD based nanostructures. The possible direction of investigations as delineated in outlook section are fundamental in nature, but it has a large bearing on applications that these heterostructure are intended to be used for.

Chapter 8

List of Publications

1. Efficient Charge Separation in CdTe Quantum Dot decorated Graphene.
   Sreejith Kaniyankandy, Sachin Rawalekar, and Hirendra N. Ghosh,
   Journal of Physical Chemistry C, 116, 16271–16275 (2011)

2. Ultrafast Relaxation Dynamics in Graphene Oxide: Evidence of Electron Trapping,
   Sreejith Kaniyankandy, S. N. Achary, Sachin Rawalekar, and Hirendra N. Ghosh, *Journal of Physical Chemistry C*, *115*, 19110–19116 (2011)

3. Ultrafast Hole Transfer in CdSe/ZnTe Type II Core-Shell Nanostructure,
   Kaniyankandy, S., Rawalekar, S.,Verma, S., Ghosh, H. N.,
   Journal of Physical Chemistry C,115, 1428-1435 (2011)

4. Charge Carrier Dynamics in Thiol Capped CdTe Quantum Dots,
   Kaniyankandy, S., Rawalekar, S.,Verma, S., Palit, D. K.
   Physical Chemistry Chemical Physics 12, 4210-4216 (2010)

5. Efficient Luminescence and Photocatalytic Behavior in Ultrafine TiO_2 Particles Synthesized by Arrested Precipitation,
   Kaniyankandy, S., Ghosh, H. N.
   Journal of Materials Chemistry, 19, 3523-3528 (2009)

6. Evidence of Multiple Electron Injection and Slow Back Electron Transfer in Alizarin-Sensitized Ultrasmall TiO_2 Particles,
   Kaniyankandy, S., Verma, S., Mondal, J. A., Palit, D. K., Ghosh, H. N.
   Journal of Physical Chemistry C 113, 3593-3599 (2009)